

MITIGATION OF TEMPERATURE POLARIZATION AND MINERAL  
SCALING IN MEMBRANE DISTILLATION: THE IMPACT OF INDUCTION  
HEATED ELEMENTS

---

A Dissertation  
Submitted to  
the Temple University Graduate Board

---

In Partial Fulfillment  
of the Requirements for the Degree  
DOCTOR OF PHILOSOPHY  
(Environmental Engineering)

---

by  
Arezou Anvari  
December 2020

Examining Committee Members :

Dr. Avner Ronen, Advisory Chair, Civil & Environmental Engineering

Dr. Heyang (Harry) Yuan, Civil & Environmental Engineering

Dr. Rouzbeh Tehrani, Civil & Environmental Engineering

Dr. Sujith Ravi, External Member, Earth and Environmental Science

©  
Copyright  
2020

by

Arezou Anvari  
All Rights Reserved

## ABSTRACT

In the last decade, there is a growing interest in membrane distillation (MD) technology, a thermally driven membrane separation process, to treat high salinity water or contaminated wastewater. However, MD commercialization is still limited by technical challenges such as temperature polarization (TP), heat losses, scaling, and high energy consumption, as the feed solution requires continuous heating to provide an efficient driving force. The present work aims to develop and optimize a novel, efficient, and robust MD system utilizing an electromagnetic field, i.e., induction heating (IH) as a heat source for MD distillation, specifically aimed to overcome MD limitations.

The proposed MD system includes a radio frequency IH system and a metallic component embedded to the hydrophobic membrane. This allows fast and contactless heating of the feed solution at the membrane surface without the need for preheating the bulk feed solution. As a result of the increase in solution's temperature at the membrane-solution interface, TP reduces and thus, distillate flux increases. In addition, as IH transfers energy directly to electrically and thermally conducting materials with minimal heat loss to the surrounding environment, it leads to significant power savings.

Two main concept approaches for the radio frequency heated MD (RF-MD) system were evaluated. First, the RF-MD system included a thermally conducting dual-layer membrane containing a magnetic hydrophilic layer based on iron oxide-carbon nanotubes coated on a hydrophobic membrane. Heating the solution was mainly done directly at the membrane-water interface. The impact of operational conditions on the distillate flux and salt rejection was evaluated while treating high salinity feeds (35-100 g/L NaCl). Following optimization, high distillate flux and 99% salt rejection were measured at a low inlet flow

velocity (2.33 cm/min) and low vacuum (20 kPa) conditions. In addition, the specific heating energy of the system was determined to be significantly lower in comparison to the conventional MD system under similar conditions. Finally, numerical simulation tools based on computational fluid dynamics (CFD) coupling heat and mass transport have been used to assess the system's limitations and potential.

In addition, the impact of RF heating on fouling, specifically addressing common inorganic scaling (i.e.,  $\text{CaSO}_4$ ) as it is a limiting factor in MD processes, was assessed. Scaling was addressed in terms of distillate flux change and crystal formation at the membrane surface and in the liquid medium. Scaling results showed the impact of RF electromagnetic field on salts crystallization, leading to less scaling. Following analysis of membrane surfaces, only sporadic small  $\text{CaSO}_4$  crystals were detected, while high concentrations of small crystals were detected at the concentrate stream exiting the MD process. The scaling mitigation mechanism is hypothesized to be a result of the high-frequency movement and collision of the ions in the solution.

The second approach is based on using RF heated stainless steel thermally conducting feed spacers, thus, coupling heating and mixing. The RF heated spacers were shown (experimentally and by numerical simulations) to reduce TP. The influence of the spacer's material and geometry were evaluated and results were compared to a conventional MD process using a polymeric spacer. Higher spacer mass and larger porosity led to an increase in distillate flux and the use of thermally conducting spacers heated by RF significantly enhanced the distillate flux while reducing the specific heating energy.

Overall, the results are promising as they show the RF-MD systems have the potential to improve MD processes, specifically for hypersaline solutions such as concentrated brine of produced wastewater, where pressure-based applications are limited.

## ACKNOWLEDGMENTS

First and foremost, I would like to express my deepest appreciation to my advisor, Dr. Avner Ronen, for his decisive role in my doctoral work. The completion of this dissertation would not have been possible without his support and nurturing. He provided me with encouragement and patience throughout the duration of this research.

I would also like to thank my committee members Dr. Heyang (Harry) Yuan, Dr. Rouzbeh Tehrani and external examiner Dr. Sujith Ravi.

Many thanks to my fellow labmates Kartikeya M. Kekre, Ying Yao, and Katelyn Kahn for their unwavering assistance and stimulating discussions. Ying was a best friend, a source of great emotional support. I greatly look forward to having all of them as colleagues in the years ahead.

Nobody has been more important to me in the pursuit of this project than the members of my family. I would like to thank my family; whose love and guidance are with me in whatever I pursue. They are the ultimate role models. Words cannot express how grateful I am to my mother for all the sacrifices that she has made on my behalf. Most importantly, I wish to thank my beloved and supportive husband, Amir who provides unending inspiration. I cannot thank him enough for encouraging and supporting me throughout this journey.

# TABLE OF CONTENTS

ABSTRACT.....	iii
ACKNOWLEDGMENTS .....	vi
LIST OF TABLES .....	xii
LIST OF FIGURES .....	xiii
CHAPTER 1 INTRODUCTION .....	1
1.1 Background .....	1
1.2 Research Objectives and Significance .....	4
CHAPTER 2 LITERATURE REVIEW .....	8
2.1 Introduction.....	8
2.2 Principle of MD Process .....	8
2.2.1 Membrane Distillation Configurations .....	9
2.2.1.1 Direct Contact Membrane Distillation (DCMD) .....	9
2.2.1.2 Air Gap Membrane Distillation (AGMD) .....	10
2.2.1.3 Sweeping Gas Membrane Distillation (SGMD).....	10
2.2.1.4 Vacuum Membrane Distillation (VMD).....	10
2.2.2 Heat Transfer in MD Process.....	11
2.2.2.1 Temperature Polarization.....	13
2.2.2.2 Temperature Polarization Coefficient (TPC).....	15
2.3 Membrane Characteristics .....	16
2.3.1 Membrane Porosity and Tortuosity .....	17

2.3.2 Membrane Pore Size and Pore Size Distribution.....	17
2.3.3 Membrane Thickness .....	18
2.3.4 Wetting Resistance.....	18
2.3.5 Thermal Conductivity .....	19
2.3.6 Chemical and Thermal Stability .....	19
2.4 Operating Parameters.....	20
2.4.1 Feed Solution Temperature.....	20
2.4.2 Feed Inlet Concentration.....	21
2.4.3 Feed Flow Velocity.....	21
2.5 Fouling .....	21
2.6 Recent Advanced MD Systems for Overcoming Temperature Polarization .....	23
2.6.1 Membrane Modification .....	24
2.6.2 Flow Promoters.....	29
2.6.3 Self-heating MD Systems .....	33
2.6.3.1 Photothermal Heating (Solar) .....	34
2.6.3.2 Joule Heating .....	42
CHAPTER 3 MATERIALS AND METHODS .....	45
3.1 Materials .....	45
3.2 Feed Solutions.....	46
3.3 Synthesis of Iron Oxide Coated Multiwall Carbon Nanotubes (Fe-CNTs).....	47
3.4 Fabrication of Fe-CNTs/PTFE Membrane .....	47
3.5 Surface Characterization.....	48

3.6 Experimental Design.....	49
3.6.1 Vacuum Membrane Distillation (VMD) system with RF heated membrane.....	49
3.6.2 Vacuum Membrane Distillation (VMD) system with RF heated spacer .....	50
3.7 MD Performance.....	51
3.8 Thermal Imaging and Temperature Profiles .....	52
3.9 Temperature Polarization Coefficient (TPC).....	53
3.10 Workpiece Power ( $P_w$ ).....	53
3.11 Temperature and Heating Rate Calculations of RF Heated Spacers .....	54
3.12 Heating Energy Calculations .....	55
3.13 Numerical Modeling and Simulation.....	56
3.13.1 VMD process with RF heated membrane.....	56
3.13.2 VMD process with RF heated spacer.....	60
3.13.2.1 Thermally Conducting Spacers in Static Conditions .....	60
3.13.2.2 Thermally Conducting Spacers in Flow Conditions.....	61
CHAPTER 4 RESULTS AND DISCUSSIONS.....	64
4.1 Membrane Distillation of High Salinity Water by Induction Heated Thermally Conducting Membranes .....	64
4.1.1 Introduction.....	64
4.1.2 Characterization of Fe-CNTs Powder.....	65
4.1.3 Fe-CNTs Coating Characterization.....	67
4.1.4 Static Heating.....	68

4.1.5 Flow Experiments .....	69
4.1.5.1 Impact of Flow Rate.....	70
4.1.5.2 Impact of Vacuum Level .....	72
4.1.5.3 Impact of Membrane Coating Thickness .....	72
4.1.5.4 Impact of Feed Concentration.....	73
4.1.6 Comparison between Conventional VMD and RF-VMD .....	76
4.1.7 Simulation and Scale up.....	79
4.1.8 Conclusions.....	83
4.2 Scaling Mitigation in Radio-Frequency Induction Heated Membrane Distillation	84
4.2.1 Introduction.....	84
4.2.2 Distillate Flux Under Scaling Conditions .....	84
4.2.3 Proposed Scaling Mitigation Mechanism .....	87
4.2.4 Impact of CaSO <sub>4</sub> Concentration.....	92
4.2.5 Impact of Feed Flow Velocity on Distillate Flux .....	95
4.2.6 Impact of Concentration Factor on Distillate Flux .....	98
4.2.7. Treatment and Scaling behavior of Simulated RO Brine .....	101
4.2.8 Conclusions.....	103
4.3 Enhanced Performance of Membrane Distillation using Radio-Frequency Induction Heated Thermally Conducting Feed Spacers.....	104
4.3.1 Introduction.....	104
4.3.2 SS Spacer Heating at Static Conditions .....	106
4.3.3 SS Spacer Heating in Flow Conditions.....	107

4.3.4 Parametric Evaluation of Operating Conditions on Distillation Flux	109
.....	
4.3.4.1 Vacuum Level.....	109
4.3.4.2 Feed Flow Velocity.....	110
4.3.4.3 Required Power to Heat SS Spacers ( $P_w$ ) .....	112
4.3.5 Optimization of Spacer’s Physical Properties and Impact of Orientation .....	113
4.3.6 Comparison of RF Heated SS Spacers with Conventional MD System	116
.....	
4.3.7 Comparison with Self-heated MD Systems.....	118
4.3.8 Conclusions.....	120
 CHAPTER 5 COMPARISON, OVERALL CONCLUSION, AND FUTURE DIRECTIONS	
.....	121
5.1 Comparison of Self-heating MD Systems .....	121
5.2 Overall Conclusion and future directions .....	126
REFERENCES .....	128

## LIST OF TABLES

<b>Table 3. 1.</b> Operating and initial parameters .....	57
<b>Table 3. 2.</b> Adopted boundary conditions (BCs) in computational model.....	58
<b>Table 3. 3.</b> Adopted boundary conditions (BCs) in computational model.....	63
<b>Table 3. 4.</b> Validation data for flow condition simulations.....	63
<b>Table 4. 1.</b> Comparison of performance and energy from different direct heating MD systems.....	78
<b>Table 4. 2.</b> Comparison between simulation and experimental results of distillate flux for RF-VMD and conventional VMD .....	80
<b>Table 4. 3.</b> Averaged temperatures and heating rates of S1 spacer according to Pc values. ....	107
<b>Table 4. 4.</b> Geometric characteristics of assessed feed spacers. ....	114
<b>Table 5. 1.</b> Comparison of self-heated MD systems. ....	124

## LIST OF FIGURES

- Figure 2. 1.** Schematic illustration of membrane distillation process and different approaches for the conventional MD process: DCMD, AGMD, SGMD, and VMD..... 9
- Figure 2. 2.** Illustration of heat transfer and TP mechanisms in the MD system..... 15
- Figure 2. 3.** (a) CNTs bilayered membrane and water vapor transport mechanism (Reprinted with permission from Ref. [131], Copyright (2016) American Chemical Society); (b) GO membrane and water vapor transport mechanism (Reprinted from Ref. [123])..... 27
- Figure 2. 4.** (a) Schematic diagram of PVDF/ATO membranes, including IR irradiated and SEM images (Reprinted from Ref. [143], Copyright (2019), with permission from Elsevier); (b) FESEM images of MXene coated PVDF membrane: (b1) surface and (b2) cross-section and (b3) IR thermal image of MXene-coated PVDF membrane after 1 min of light irradiation (average initial temperature of 22 °C) (Reprinted from Ref. [145], Copyright (2018), with permission from Elsevier)..... 29
- Figure 2. 5.** (a) Schematic of feed spacer and its structural parameters; (b) Simulation results of (b1) heat transfer coefficient ( $W/m^2.K$ ) and (b2) shear stress (Pa) for spacer filled channels (left side) compare to the empty channel (right side) (Reprinted from Ref. [151], Copyright (2017), with permission from Elsevier); (c) Different configurations of 3D-printed spacers (Reprinted from Ref. [161], Copyright (2018), with permission from Elsevier) (d) SEM image of metallic foam (Reprinted from Ref. [165], Copyright (2019), with permission from Elsevier)..... 33
- Figure 2. 6.** (a) Schematic of the solar-driven DCMD system (Reproduced from Ref. [182], Copyright (2018), with permission from the Royal Society of Chemistry); (b) CB-PVDF dual-layer membranes used in solar-driven system [177]; (c) Schematic of the solar-driven

DCMD system coupled with a dynamic heat recovery (HX) system,  $Q_F$  and  $Q_D$  represent the feed flow and distillate flow, respectively (Reproduced from Ref. [181], Copyright (2020), with permission from the Royal Society of Chemistry); (d) Schematic of a solar-driven MD system under focused illumination [185]; (e) Impact of light focusing on distillate flux in solar-driven MD system [185]..... 41

**Figure 2. 7.** (a) Joule heating effect of CNTs layer in a non-ionizable environment (Reprinted from Ref. [187], Copyright (2017), with permission from Springer Nature); (b) Cross-section SEM image of dual-layer hydrophilic/hydrophobic CNTs/PTFE membrane (Reprinted from Ref. [187], Copyright (2017), with permission from Springer Nature); (c) Direct heating of feed solution on the CNTs/PTFE membrane; (Reprinted from Ref. [187], Copyright (2017), with permission from Springer Nature); (d) Cross-section SEM of NRW membrane (Reprinted from Ref. [192], Copyright (2019), with permission from Elsevier); (e) IR image of electro-thermal NRW membrane in the feed solution at different current and initial feed solution of 30 °C (Reprinted from Ref. [192], Copyright (2019), with permission from Elsevier)..... 44

**Figure 3. 1.** Images of the SS and PP feed spacers. .... 46

**Figure 3. 2.** Schematic diagram of the RF-VMD system..... 50

**Figure 3. 3.** Schematic diagram of the (a) Membrane module; (b) Spacer’s parameters. 51

**Figure 3. 4.** IR thermal image of the S1 spacer after 5 seconds of induction heating. .... 55

**Figure 3. 5.** Computational domain and mesh grid including three distinct regions; feed (saline water stream), membrane, and permeate (pure water vapor)..... 58

<b>Figure 3. 6.</b> Configuration of coil, spacer, and air domains used for 3D numerical simulations-static condition. ....	60
<b>Figure 3. 7.</b> Configuration of coil, spacer, and feed solution domains used for 3D numerical simulations – Flow condition.....	63
<b>Figure 4. 1.</b> Illustration of the RF-VMD process. Bottom layer: temperature profile in the feed; Middle layer: composite membrane; Top: vacuum chamber. Right image: enlargement of the Fe-CNTs layer.....	65
<b>Figure 4. 2.</b> Characterization of the synthesized Fe-CNTs powder: (a) SEM image of CNTs; (b) SEM image of Fe-CNTs; (c) TEM image of Fe-CNTs; (d) EDX analysis of Fe-CNTs film; (e) FTIR analysis of Fe-CNTs. ....	66
<b>Figure 4. 3.</b> Surface characterization of the Fe-CNTs layer: (a) SEM cross section of Fe-CNTs/PTFE membrane; (b) Water contact angle of PTFE commercial membrane; (c) Water contact angle of Fe-CNTs/PTFE membrane. ....	68
<b>Figure 4. 4.</b> Water droplets temperature on the Fe-CNTs membrane as a function of membrane coating thickness and contact time.....	69
<b>Figure 4. 5.</b> (a) Impact of flow velocity on distillate flux and salt rejection at 30 kPa vacuum pressure; (b) Impact of vacuum level on distillate flux and salt rejection with 2.33 and 11.25 cm/min feed flow velocity; (c) Impact of Fe-CNTs loading and layer thickness on distillate flux at 20 kPa vacuum pressure, and 2.33 cm/min feed flow velocity; (d) Impact of feed salt concentration on distillate flux of RF-VMD and conventional VMD at 20 kPa vacuum pressure, and 2.33 cm/min feed flow velocity. ....	75

<b>Figure 4. 6.</b> (a) Distillate flux and specific heating energy of Fe-CNTs/PTFE membrane in RF-VMD and unmodified PTFE membrane in conventional VMD at 2.33 cm/min feed flow velocity and 20 kPa vacuum pressure; Temperature Polarization membrane in (b) conventional VMD (c) RF-VMD.....	78
<b>Figure 4. 7.</b> (a) FEM simulation of feed temperature distribution and (b) distillate flux values along the membrane in the conventional VMD model with feed temperature 65 °C; (c) FEM simulation of feed temperature distribution and (d) distillate flux values along the membrane in the RF-VMD model with feed temperature 20 °C; feed flow velocity for both systems: 2.33 cm/min.....	81
<b>Figure 4. 8.</b> Impact of system scaling on system performance by using a FEM simulation of a scaled-up system: (a) Distillate flux along a membrane module as a function of flow rate with heat source flux: 781.25 W/m <sup>2</sup> , (b) Distillate flux along a membrane module as a function of heat source energy with flow velocity 750 cm/min; (c) Specific heating energy of RF-VMD as a function of heat source energy at 750 cm/min feed flow velocity.....	83
<b>Figure 4. 9.</b> N.Fs of C-VMD and RF-VMD systems as a function of time at feed velocity of 2.33 cm/min and vacuum pressure of 20 kPa for the distillation of 35 g/L NaCl with 1.8 g/L CaSO <sub>4</sub> solution and feed inlet temperatures of 65 °C and 20 °C, respectively.....	86
<b>Figure 4. 10.</b> Morphological images of used membranes' surface in (a) C-VMD; (b) RF-VMD systems, and EDX images of selected parts of membranes in (c) C-VMD; (d) RF-VMD systems for the distillation of 35 g/L NaCl with 1.8 g/L CaSO <sub>4</sub> solution. Feed velocity of 2.33 cm/min, vacuum pressure of 20 kPa, and feed inlet temperatures of 65 °C and 20 °C, respectively. ....	87

<b>Figure 4. 11.</b> Light microscopy images of the concentrated flow of (a) C-VMD; (b) RF-VMD, and ImageJ counting images for the concentrated flow of (c) C-VMD; (d) RF-VMD. .....	89
<b>Figure 4. 12.</b> Schematic illustration of (a) CaSO <sub>4</sub> scaling in the C-VMD system (b) declined CaSO <sub>4</sub> scaling in the RF-VMD system. ....	90
<b>Figure 4. 13.</b> Influence of RF-VMD on N.F as a result of solution composition. Feed velocity of 2.33 cm/min, vacuum pressure of 20 kPa, and feed inlet temperature of 20 °C. .....	92
<b>Figure 4. 14.</b> Influence of CaSO <sub>4</sub> feed concentration on the N.F of (a) C-VMD; (b) RF-VMD systems. Feed velocity of 2.33 cm/min, vacuum pressure of 20 kPa, and feed inlet temperatures of 65 °C and 20 °C for C-VMD and RF-VMD, respectively. ....	94
<b>Figure 4. 15.</b> EDX and SEM images of membranes surface at 3.6g/L CaSO <sub>4</sub> feed concentration in: (a) C-VMD; (b) RF-VMD systems.....	95
<b>Figure 4. 16.</b> Influence of feed flow velocity on the N.F of RF-VMD system at 35 g/L NaCl with (a) 1.8 g/L; (b) 3.6 g/L CaSO <sub>4</sub> feed solution. ....	97
<b>Figure 4. 17.</b> (a) Impact of ionic strength on the CaSO <sub>4</sub> solubility; (b) Impact of CF on the solubility and concentration of CaSO <sub>4</sub> ; (c) Impact of CF on N.F of C-VMD and SEM image of membrane surface at CF=4 in the C-VMD; (d) Impact of CF on N.F of RF-VMD and SEM image of membrane surface at CF=4 in the RF-VMD. ....	101
<b>Figure 4. 18.</b> (a) Impact of RF-VMD on N.F of RO brine compared to saline solutions with and without CaSO <sub>4</sub> ; (b) EDX and SEM images of membranes surface of RO brine in RF-VMD system. ....	103

<b>Figure 4. 19.</b> Schematic diagram of the RF heated MD process. Bottom layer: vacuum chamber; Middle layer: membrane-feed spacer interface; Top: feed solution and temperature profile (red: hot; blue: cold).....	105
<b>Figure 4. 20.</b> (a) IR thermal image of the heated SS feed spacer ( $P_c$ of 60W); (b) Numerical simulation of the temperature profile of the RF heated SS feed spacer at similar conditions. The temperature scale is in $^{\circ}\text{C}$ units.....	107
<b>Figure 4. 21.</b> IR thermal images of SS spacer and the feed solution in the flow module: (a) Initial conditions; (b) Following 30 seconds of RF heating; Numerical simulation of temperature profile of the RF-heated SS spacer and the feed solution in the flow module: (c) top view; (d) cross-section. Temperature scale is in $^{\circ}\text{C}$ units.....	109
<b>Figure 4. 22.</b> (a) Impact of vacuum level on distillate flux of the SS spacer in RF heated based VMD, at 50 cm/min feed flow velocity and $P_c$ of 60 W; (b) Impact of feed flow velocity on distillate flux of the SS spacer in RF heated based VMD, at 20 kPa vacuum pressure and $P_c$ of 60 W.....	112
<b>Figure 4. 23.</b> (a) Impact of $P_w$ on distillate flux of SS spacer in RF-IH based VMD, at 20 kPa vacuum pressure. (b) Impact of $P_w$ on specific heating energy of SS spacer in RF-IH based VMD, at 20 kPa vacuum pressure. ....	113
<b>Figure 4. 24.</b> (a) Distillate flux of SS spacers in RF-VMD as a function of feed flow velocity; (b) Distillate flux of S1 and S4 spacers with $45^{\circ}$ and $90^{\circ}$ spacer filament orientations as a function of feed flow velocity.....	116
<b>Figure 4. 25.</b> (a) Distillate flux of C-VMD with and without PP and S4 spacers in comparison to the RF heated VMD system with S4 spacer at flow velocities of 100 and 300 cm/min.; (b) Numerical simulation results of TPC along the membrane length in the RF heated MD system.....	118

**Figure 4. 26.** Distillate flux and specific heating energy comparison of self-heated MD systems [177,187,193]. ..... 120

**Figure 5. 1.** Specific heating energy consumption ( $Q_{sh}$ ), gain output ratio (GOR), and energy efficiency of recently self-heated developed MD processes. Labels correspond to Table 5.1. Colors represent the efficiency percentage (%) of systems. NA: not available. .... 125

# CHAPTER 1

## INTRODUCTION

### 1.1 Background

Rapid population growth, coupled with changing climate, has resulted in a rise in potable water deficiency in many water-stressed countries worldwide [1–3]. Therefore, new technologies for providing freshwater have been developed to diminish water stress, including water desalination and distillation processes designed to recover water from saline or contaminated water sources such as seawater, brackish groundwater, and hypersaline solutions (e.g., reverse osmosis (RO) brine or produced water) [4–9]. Currently, there are almost 16,000 desalination plants worldwide with a desalination capacity of 95 million m<sup>3</sup>/day [10]. Generally, desalination technologies can be divided according to their separation methods, by membranes (i.e., pressure-driven separation) or through thermal processes. The contribution of thermal processes, including multi-effect distillation and multi-stage flash, is about 31.5% of the total desalination capacity, and the rest (about 68.5% or 65.5 million m<sup>3</sup>/day) is based on membrane processes [11,12]. Membrane-based desalination has several benefits over thermal distillation, including the limited need to provide thermal energy, low environmental impacts related to thermal energy production by fuel consumption, reduction of pumping requirements, and no incorporated large ecological footprints that are required in many thermal distillation plants [13–15]. On the other hand, high-pressure separation RO systems suffer from limitations related to the nature of their separation mechanism, including membrane fouling, the need for high pressure and energy when desalinating hypersaline feed, and pretreatment of the feed solution, resulting in an elevated cost of treatment [16–21].

Membrane distillation (MD) is a hybrid technology that combines the advantages of membrane separation and thermal distillation [8,22–24]. The separation is based on transmembrane partial vapor pressure, leading to transport of only water vapor molecules through a hydrophobic microfiltration membrane. In order to ensure an efficient driving force and relatively high distillate flux, the feed solution is continuously heated. While the volatile vapors cross the membrane to the distillate side, the liquid does not enter the membrane pores due to the membrane's surface tension and hydrophobic nature. Water vapor is collected and condensed at the distillate side by a range of operational configurations, including direct contact membrane distillation (DCMD), air gap membrane distillation (AGMD), sweeping gas membrane distillation (SGMD), and vacuum membrane distillation (VMD) [25–27]. MD has multiple advantages over other desalination processes, including high rejection of non-volatile compounds, low concentration polarization (CP), limited fouling, and low operating pressure and temperature even when distilling hypersaline solutions [22,23,28–33]. Therefore, MD technology has gained interest as an alternative to both pressure-driven membrane separation and conventional thermal driven separation processes, fitting for desalination and wastewater treatment processes [32,34–39].

Despite these advantages, industrial applications of large-scale MD have been restricted primarily by technical challenges such as temperature polarization (TP), high energy required for heating the bulk feed solution, heat losses, and the need for expensive heat management due to metal corrosion of heat exchangers when exposed to a heated saline feed [40–42]. MD systems undergo TP as the feed temperature is higher than the water-membrane interface temperature due to the consumed latent heat of vaporization as a result

of water evaporation. TP leads to a decrease in mass transfer through the membrane and reduced distillate flux as a result of a decline in the driving force for vapor transport (i.e., decreased vapor pressure at the membrane surface) [24,43–45]. Thus, mitigating TP is an essential tool for controlling MD performance and increasing distillation efficiency. Furthermore, membrane fouling is considered as another limiting phenomenon for MD application as it leads to a decrease in distillate flux and changes in membranes' surface properties. Fouling was shown to increase membrane hydrophilicity and wettability, eventually leading to a decrease in membrane selectivity [46,47]. As MD systems are typically used to reclaim clean water from different degrees of saline solutions (i.e., saline water to concentrated brine or produced water), accumulation of inorganic fouling (i.e., scaling) such as calcium sulfate ( $\text{CaSO}_4$ ) and calcium carbonate ( $\text{CaCO}_3$ ) is considered a critical problem [48–50]. In addition, scale layers on the membrane surface can intensify the negative influences of TP and CP, thus, reducing the active surface of the membrane for water evaporation and consequently decreasing distillate flux [51,52]. Controlling and removing  $\text{CaSO}_4$  scaling was shown difficult in comparison to  $\text{CaCO}_3$  [53]. While  $\text{CaCO}_3$  typically precipitates and adheres to heat exchangers and tubing prior to entering the filtration module,  $\text{CaSO}_4$  was shown to form suspended crystals that may reach the membrane surface and deposit on it as scaling [54]. Therefore,  $\text{CaSO}_4$  scaling mitigation is considered crucial for future MD commercialization.

Finally, in addition to water desalination, there is a growing understanding that brine discharge has significant environmental impacts, and therefore, it should be treated and managed prior to release. Since MD is suggested as a possible treatment approach, it is

vital to evaluate the operating limiting phenomena as TP, high energy consumption, heat loss, and scaling to derive methods to decrease their impact.

## **1.2 Research Objectives and Significance**

The overall objective of this research is to develop and optimize a novel, efficient, and robust vacuum MD (VMD) system to treat high salinity contaminated feed solutions while increasing the distillate flux and decreasing TP, inorganic fouling (i.e., scaling), and the required energy in comparison to conventional VMD systems.

The main research hypothesis is that applying an electromagnetic (i.e., radio frequency altering magnetic) field on the conductive component (i.e., membrane or spacer with thermally conductive and magnetic properties) leads to rapid and constant direct heating of the membrane-water interface, thus, providing an efficient driving force for vapor transport through the membrane. To assess and optimize the transport, we evaluated how operational parameters and material properties related to the coated membrane or spacer impact the distillate flux and rejection. Furthermore, we tested the system at realistic conditions and evaluated solutions with high salinity and high scaling potential. Finally, temperature profiles and transport mechanisms were assessed using numerical simulation.

In order to meet this objective, the following individual goals have been accomplished:

1. Assess the impact of utilizing induction heating (IH) as a heat source to the distillation process by applying a RF altering magnetic field on a thermally conductive iron coated carbon nanotubes (Fe-CNTs) membrane.

This objective includes:

- a. Fabrication and characterization of a thermally conductive magnetic membrane to be used in MD and heated under RF electromagnetic field.

- b. Evaluate the impact of operational parameters (i.e., feed flow velocity and vacuum level) on distillate flux and salt rejection.
  - c. Evaluate the impact of Fe-CNTs membrane parameters (i.e., Fe-NP concentration and layer thickness) on distillate flux and salt rejection.
  - d. Evaluate the performance of salinity feed (35-100 g/L sodium chloride) on distillate flux and salt rejection.
  - e. Simulate the proposed desalination process using CFD to evaluate its limitations and potential.
  - f. Evaluate the ability to scale up the RF-MD system using the similar CFD simulated approach.
2. Evaluate scaling mitigation in RF heated MD system including a thermally conductive magnetic membrane.

This objective includes:

- a. Assess the influence of RF heating on  $\text{CaSO}_4$  scaling in terms of distillate flux and crystal formation compared to conventional MD systems.
- b. Propose a scaling mitigation mechanism.
- c. Evaluate the impact of  $\text{CaSO}_4$  ions concentration on distillate flux and scaling.
- d. Evaluate the impact of feed flow velocity on distillate flux and scaling.
- e. Evaluate the impact of the concentration factor on distillate flux and scaling.

- f. Determine treatment and scaling behavior of simulated RO brine in the proposed RF-MD system.
3. Assess the use of ‘self-heating’ thermally conducting feed spacers exposed to the RF altering magnetic field to overcome TP, CP, and lower the elevated energy required for heating the bulk feed solution, and the heat losses associated to the MD.

This objective includes:

- a. Evaluate the ability of conductive spacers to be heated under RF-IH and measure the received power by spacers.
- b. Evaluate temperature distribution of RF-IH spacers in flow process.
- c. Evaluate the impact of operational parameters (i.e. feed flow velocity, vacuum level, and received workpiece power) on distillate flux and salt rejection.
- d. Evaluate the impact of spacer’s physical properties and orientation on distillate flux.
- e. Simulate the RF heated spacers using CFD to evaluate heating process and calculate the TP coefficients.

In general, the results of this research will advance the understanding of self-heating-based MD processes. In particular, this research will produce understanding of the role of radio frequency electromagnetic field, as a heat source for MD distillation, on distillation efficiency and eliminating MD limitations. To the best of our knowledge, this research introduces induction heated MD process for the first time as a novel MD design.

Therefore, the results of this research will produce the following outcomes: (1) An understanding of the ability and advantage of IH to treat solutions with high salinity; (2) An understanding of the influence of operating conditions and magnetic components' properties on water flux and rejection in IH-MD; (3) A quantification of how IH-MD mitigates scaling; (4) An evaluation of the overall efficiency and cost assessment of IH based MD technology in terms of heating energy consumption per kg of distillate, permeate flux, and salt rejection in comparison to other common desalination technology.

Overall, this research will assess the potential and the ability of IH-MD technology to treat highly contaminated wastewater and optimize the system to effectively treat high salt concentration wastewater or brine, specifically for applications that require high salinity distillation where pressure-based applications such as RO cannot be used. The knowledge gained here will provide information for addressing other industrial applications as well, e.g. concentrating solution or treating contaminated wastewater.

## **CHAPTER 2**

### **LITERATURE REVIEW**

#### **2.1 Introduction**

In this chapter, a literature review is dichotomized into two parts. First part includes a brief description of membrane distillation process along with its governing transport phenomena and configurations, TP and its observed effects on MD processes, effect of membrane properties and operational parameters on MD processes, and finally membrane fouling in MD processes. The second part aims to summarize recent advances made to mitigate TP in MD systems and assess their influence on distillation efficiency. We include a brief description of recent advanced MD processes from the aspects of low or negligible TP, high distillate flux, and improved energy efficiency.

#### **2.2 Principle of MD Process**

The MD process includes a microporous hydrophobic membrane in direct contact of an aqueous warm feed solution on one side in which the hydrophobicity of the membrane hinders the diffusion of liquid phase molecules (as shown in Figure 2.1). The vapor-liquid interface is generated at the entrance of membrane pores due to the temperature gradient across the membrane. Then, evaporated volatile compounds at the high vapor pressure penetrate through the membrane pores and migrate to the low-pressure side. On the low pressure side of the membrane (i.e. permeate side), vapor molecules are collected and condensed as the aqueous permeate of the system [22,25–27,55,56].

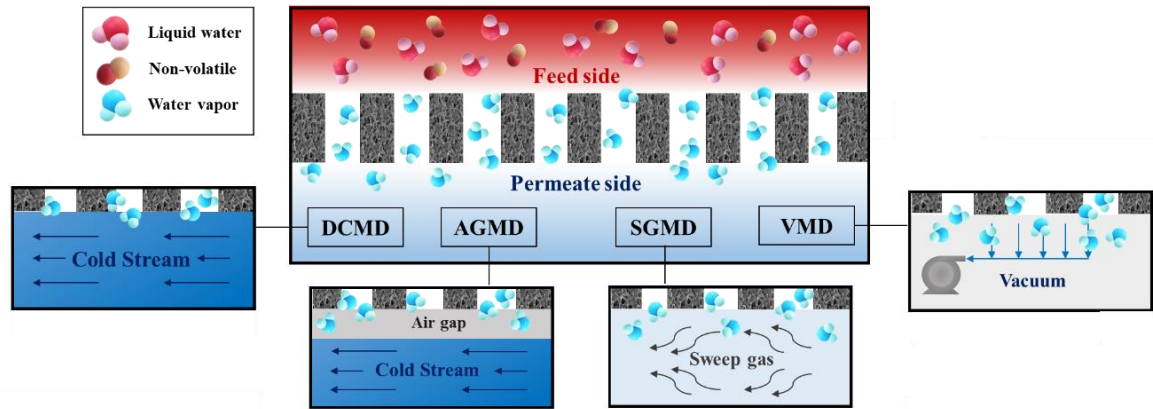


**Figure 2. 1.** Schematic illustration of membrane distillation process and different approaches for the conventional MD process: DCMD, AGMD, SGMD, and VMD

## 2.2.1 Membrane Distillation Configurations

Based on incentive methods of vapor pressure gradient through the membrane and removing transported vapors from the distillate side, MD processes are classified into four basic configurations (Figure 2.1): DCMD, AGMD, SGMD, and VMD [25,27,41,55]. The following section describes these configurations along with some of their advantages and disadvantages.

### 2.2.1.1 Direct Contact Membrane Distillation (DCMD)

In DCMD process, as shown in Figure 2.1, the temperature gradient through the membrane is resulted from direct contact of a low temperature aqueous solution with the permeate side of the membrane, leading to the vapor pressure difference. Accordingly, volatile molecules vaporize and move into the membrane pores, then, vapors are condensed at the permeate side. Even though DCMD is widely used configuration due to its simplicity, it has large conductive heat losses due to the continuous and direct contact between hot feed, membrane, and the permeate cold side [21,25,26,41,56,57].

### **2.2.1.2 Air Gap Membrane Distillation (AGMD)**

AGMD process includes a thin stationary air layer between the membrane and the condensation surface (i.e., the distillate side). The transported vapors across the membrane proceed as well through the air gap and consequently condense on the cooling surface [25,41] (Figure 2.1). The main advantages of this relatively difficult module are less conduction heat loss and pore wetting risk on the distillate side. On the other hand, the air layer increases the mass transfer resistance and so decreases the distillate flux [58,59].

### **2.2.1.3 Sweeping Gas Membrane Distillation (SGMD)**

In SGMD process, an inert gas stream is utilized to sweep and gather the vapor molecules at the permeate side of the membrane (Figure 2.1). Then, collected vapors are condensed with an exterior condenser [25,41]. The benefit of this module in comparison to the AGMD is that the air gap is not stagnate that improves the mass transfer coefficient. In addition, this module has low thermal polarization and no pore wetting risk. However, due to the demand for large condenser, the equipment cost is increased [41,59].

### **2.2.1.4 Vacuum Membrane Distillation (VMD)**

In VMD configuration, as shown in Figure 2.1, a pump is utilized to provide enough vacuum in the permeate side and then vapors eventuate in condensing outside of the membrane module. As a result, conduction heat loss of this configuration is low in comparison to other configurations. Compare to the other MD configurations, VMD can deliver higher distillate flux. Similar to SGMD, this configuration with low thermal polarization requires separate condenser and vacuum [22,59].

### 2.2.2 Heat Transfer in MD Process

MD technology is based on the fact that the temperature gradient between the feed and distillate results in heat transfer from the membrane's hot side to its cold side, and subsequently, a phase transition from liquid to vapor on the membrane's feed side surface. Heat transfer occurs through three regions: the feed boundary layer, the membrane, and the permeate boundary layer (Figure 2.2). The heat transfer through the feed boundary layer ( $Q_f$ , Eq. 2.1) is based on convection as the bulk feed solution temperature ( $T_f$ ) is higher than the interfacial temperature of the feed side and membrane ( $T_{fm}$ ) and can be described by Eq. 2.1 [25,60]:

$$Q_f = h_f(T_f - T_{fm}) \quad \text{Eq. 2.1}$$

Where  $h_f$  is the feed convective heat transfer coefficient.

The heat transfer into the membrane ( $Q_m$ , Eq. 2.2) is based on both conduction ( $Q_{cm}$ ) and latent heat of vaporization ( $Q_v$ ), while the effect of mass transfer on the heat transfer can be neglected [25].

$$Q_m = Q_{cm} + Q_v = \frac{k_m}{\delta_m}(T_{fm} - T_{pm}) + J\Delta H_v \quad \text{Eq. 2.2}$$

Where  $\frac{k_m}{\delta_m}$  and  $T_{pm}$  are the membrane's heat transfer coefficient and the temperature of the membrane's surface in the permeate side, respectively.  $k_m$  and  $\delta_m$  are thermal conductivity and thickness of the membrane, respectively.  $J$  and  $\Delta H_v$  are transmembrane flux and evaporation enthalpy of water, respectively [21,25]. Finally, heat transfer within the permeate side ( $Q_p$ , Eq. 2.3) is based on convection using convective heat transfer coefficient ( $h_p$ ), as  $T_{pm}$  is higher than the temperature of the permeate side ( $T_p$ ) [25].

$$Q_p = h_p(T_{pm} - T_p) \quad \text{Eq. 2.3}$$

It is worth mentioning that the convection heat transfer of the permeate side in a VMD process can be ignored due to the vacuum pressure applied at the permeate side of the membrane [36,61].

At steady-state condition, the heat transfer through all three regions is equal to the overall heat transfer (Q) (Eq. 2.4 and 2.5) [25,36]:

$$Q = Q_f = Q_m = Q_p \quad \text{Eq. 2.4}$$

$$H(T_f - T_p) = h_f(T_f - T_{fm}) = \frac{k_m}{\delta_m}(T_{fm} - T_{pm}) + J\Delta H_v = h_p(T_{pm} - T_p) \quad \text{Eq. 2.5}$$

Where H is the overall heat transfer coefficient and can be described based on the thermal resistance series model (Eq. 2.6) [25,36]:

$$\frac{1}{H} = \frac{1}{h_f} + \frac{1}{\frac{k_m}{\delta_m} + \frac{J\Delta H_v}{(T_{fm} - T_{pm})}} + \frac{1}{h_p} \quad \text{Eq. 2.6}$$

As the surface temperature of both sides of the membrane ( $T_{fm}$  and  $T_{pm}$ ) cannot be calculated or measured experimentally, an iterative mathematical model has been defined to assess these temperatures using Eq. 2.7 and 2.8 [25,62]:

$$T_{fm} = T_f - \frac{J\Delta H_v + \frac{k_m}{\delta_m}(T_{fm} - T_{pm})}{h_f} \quad \text{Eq. 2.7}$$

$$T_{pm} = T_p - \frac{J\Delta H_v + \frac{k_m}{\delta_m}(T_{fm} - T_{pm})}{h_p} \quad \text{Eq. 2.8}$$

Accordingly, higher convective heat transfer coefficients across the feed and permeate boundary layers ( $h_f$  and  $h_p$ ) increase the values of  $T_{fm}$  and  $T_{pm}$  to the extent of  $T_f$  and  $T_p$  values, respectively.

### 2.2.2.1 Temperature Polarization

Temperature polarization (TP) describes a condition in which the temperature of the bulk feed solution differs from the membrane's interface temperature. TP is considered as a critical factor of the MD process with severe impact on flux reduction [63]. During the evaporation of water at the membrane's surface, the latent heat of evaporation cools down the liquid. Thus, the interfacial temperature of the feed side is lower than the temperature of the bulk feed solution [63]. The lower temperature at the membrane-water interface leads to a decrease in driving force as vapor pressure is exponentially related to temperature, according to Antoine's equation [50,64–66]. In this regard, Figure 2.2 describes the temperature profiles for the condition where fluids are in direct contact with both sides of the membrane, a hot liquid on the feed side, and a cold liquid on the distillate side (i.e., DCMD process). As shown in Figure 2.2, thermal boundary layers are formed on both sides of the membrane as water evaporation occurs at the feed side of the membrane's surface and condensation at the distillate side of the membrane's surface. Therefore, temperatures at the membrane-liquids interfaces vary from the bulk temperatures of feed and distillate streams. As a result, the effective temperature gradient of two sides of the membrane ( $T_{fm}-T_{pm}$ ) is lower than the temperature difference between the bulk solutions ( $T_f-T_p$ ), leading to a loss of driving force. The extent of temperatures' gradients determines the intensity of TP. TP can impact the performance of MD processes in terms of distillate flux and energy efficiency [45,67]. It has been shown that due to the temperature difference between the bulk feed solution and the membrane interface, the non-isothermal boundary layer in the vicinity of the membrane surface leads to a decrease in driving force, 50-80% decrease in water vapor mass transfer, and consequently lower distillate flux [60]. In addition, the developed thermal boundary layer decreases the thermal efficiency of MD as

it increases heat loss through the membrane, thus, increasing the energy needed to achieve stable distillate flux along the membrane length [25,63,68,69].

Operating conditions in both sides of the membrane (i.e., flow velocity, module design, spacers, and fluid properties) and membrane properties (i.e., porosity, permeability, thickness, and thermal conductivity) were shown to influence TP by impacting mass and heat transfer. For example, laminar flow conditions with low mixing, high salt concentration, and high feed temperature were determined to increase TP [45,62] as well as membranes with higher thermal conductivity, higher permeability, and lower thickness [70]. The thermal conductivity of membranes is influenced by the membrane's porosity [71]. Higher porosity and relatively larger pore size decrease heat loss across the membrane and consequently increase the driving force, flux, and energy efficiency [70,72]. In addition to the membranes' physical properties, enhanced feed flow, i.e., an increase of feed flow rates and therefore mixing near the membrane's surface, led to a decrease in the thermal boundary layer thickness and reduced TP [73]. Furthermore, according to Eq. 2.7 and 2.8, higher convective heat transfer coefficients of the feed and permeate ( $h_f$  and  $h_p$ ), which can be obtained by increasing the flow velocity and mixing, increase  $T_{fm}$  and  $T_{pm}$  to values close to  $T_f$  and  $T_p$ , respectively, and thus, lead to a lower TP and higher MD efficiency. Commonly used strategies to reduce TP include higher feed flow velocities and the addition of turbulence promoters such as feed spacers [74–76] and corrugated feed channels [77–79]. The recent advancements in MD technology targeted to eliminate TP are discussed in section (2.6).

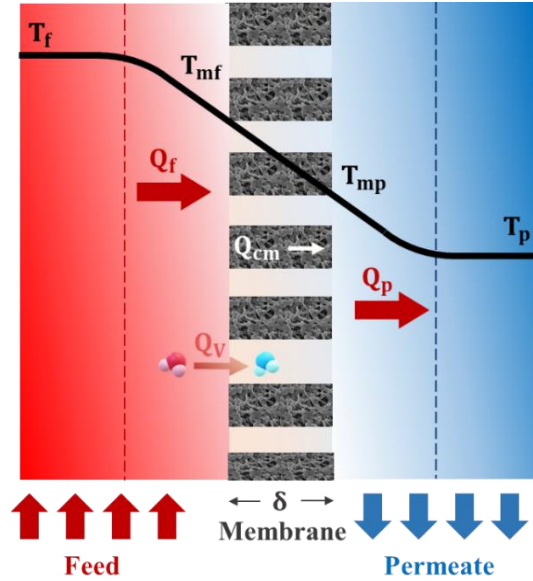


**Figure 2. 2.** Illustration of heat transfer and TP mechanisms in the MD system.

### 2.2.2.2 Temperature Polarization Coefficient (TPC)

As the thermal boundary layer is considered one of the restraining factors of heat transfer efficiency, temperature polarization coefficient (TPC) is used to quantify the degree of boundary layer resistance versus the total heat transfer resistance, as so, it can be used as a valuable tool for assessing and designing MD systems [80]. Generally, TPC is related to the feed convective heat transfer within the thermal boundary layer of the feed side. TPC can be described by the ratio of surface temperature gradient through both sides of the membrane to the temperature gradient of the bulk [22,25,45,55,80] (Eq. 2.9).

$$\text{TPC} = \frac{T_{fm} - T_{pm}}{T_f - T_p} \quad \text{Eq. 2.9}$$

Where  $T_f$  and  $T_p$  are the bulk temperature of feed and permeate solutions, respectively, and  $T_{fm}$  and  $T_{pm}$  are the temperature of feed and distillate fluids at the membrane interface, respectively.

Depending on the impact of the thermal boundary layer on the heat transfer resistance, TPC ranges between 0 and 1. When TPC approaches 0, MD is limited by heat transfer in the

feed side through the thermal boundary layer and TP is notable, indicating an inadequately designed system. However, when TPC value converges to 1, the process is limited by mass transfer through the membrane, leading to less impact of TP, which typically indicates a well-designed system [60].

In order to measure the influence of TP in VMD systems, a slightly different equation was presented using Eq. 2.10 [36,60]:

$$\text{TPC} = \frac{T_{\text{fm}}}{T_f} \quad \text{Eq. 2.10}$$

Based on the Eq. 2.10, when  $T_{\text{fm}}$  approaches the feed bulk solution temperature ( $T_f$ ), i.e., at insignificant TP, the TPC value is closer to 1, whereas TP is notable when TPC value reaches zero as  $T_{\text{fm}}$  is much smaller than  $T_f$  [36,60].

Overall, TPC can be used as a tool for analyzing the behavior of MD systems. In conventional MD systems, TPC values vary between 0.4 and 0.7 [22,25,55,80], corresponding to 60% and 30% dissipation of the bulk temperature gradient (i.e.,  $T_f - T_p$ ) in the thermal boundary layers, respectively [80].

### **2.3 Membrane Characteristics**

The appropriate selection of membrane, as a physical support for a liquid-vapor interface, used in MD process is vital. The membrane must fulfil several requirements concurrently. The presence of only the vapor phase in the membrane pores is an inevitable condition for MD, therefore, hydrophobicity of the membrane has a critical role in this process [81]. In this manner, a wide variety of polymers such as polytetrafluoroethylene (PTFE), polyvinylidene fluoride (PVDF), and polypropylene (PP) are accessible to prepare membrane in the flat sheet or tubular form [22,25,81]. Generally, the membrane in the MD system should have low thermal conductivity, low mass transfer resistance, and good

thermal stability for intense temperatures along with excessive chemical resistance to feed solutions such as acids and bases [25].

### **2.3.1 Membrane Porosity and Tortuosity**

Membrane porosity is defined as the vacant volume fraction of the membrane which can be determined by dividing the volume of the pores over the total volume of the membrane. Higher porosity of membranes displays larger surface area for evaporation. In general, regardless of the type of MD configuration, membranes with high porosity have more distillate flux as well as lower conductive heat loss. Porosity of MD membranes is between 30 and 85% [22,25,26].

Tortuosity ( $\tau$ ) is the aberration of the pores from the cylindrical structure. High tortuosity value leads to the lower distillate flux due to the vapor molecules permeation into tortuous paths, thus, the MD membrane permeability is inversely in proportion to the membrane tortuosity [25,26]. In most theoretical models in MD studies, a value of 2 is frequently considered for membrane tortuosity factor to predict the transmembrane flux [80].

### **2.3.2 Membrane Pore Size and Pore Size Distribution**

The membrane pore size in MD systems varies typically between 0.05  $\mu\text{m}$  and 1  $\mu\text{m}$ . While the increase of pore size causes higher distillate flux, it can lead to liquid penetration into the membrane pores and reduce membrane selectivity. Therefore, depending the feed solution and operational conditions, the optimum value is required to be determined [25,70]. In general, in order to balance between the distillate flux and low liquid penetration, membrane with pore diameter of 0.3  $\mu\text{m}$  is recommended. For VMD configuration, a smaller pore size (0.1 to 0.2  $\mu\text{m}$ ) is more effective since this configuration is more sensitive to wetting [70].

Membranes basically have a pore size distribution rather than an invariable pore size [26]. It has been shown that the narrow pore size distribution is more effective for membranes used in MD processes [82] while some studies showed that the influence of pore size distribution on permeate is insignificant for DCMD [72,83]. Therefore, it is recommended to utilize membranes with a small pore size distribution to decrease the risk for liquid penetration as much as possible, while still attaining the most possible distillate flux [70].

### 2.3.3 Membrane Thickness

In the MD system, the membrane thickness is an important characteristic which does not have straightforward role. In other words, the distillate flux reduces as the membrane becomes thicker due to the increase of mass transfer resistance, while thinner membranes undergo more energy losses because of higher conduction heat through the thin membrane. Therefore, an optimal thickness should be considered in order to obtain highest mass transport while reducing heat losses [25,70]. Eykens et al. [84] determined that for feed solutions with salinity ranging from 3 wt% up to 24 wt%, an optimal membrane thickness is in the range of 2–739  $\mu\text{m}$ .

### 2.3.4 Wetting Resistance

The wetting resistance of membranes in MD processes is evaluated by the liquid entry pressure (LEP), which is the minimum pressure required to make the membrane wet. Membrane characteristics and feed composition have significant influence on the LEP which can be calculated by the Laplace equation (Eq. 2.11):

$$\text{LEP} = \frac{-2 \beta \gamma_1 \cos \theta}{r_{\max}} \quad \text{Eq. 2.11}$$

Where  $\gamma_1$  is the surface tension of the liquid,  $\theta$  is the contact angle,  $r_{\max}$  is the maximum pore size, and  $\beta$  is a geometric factor [70]. Therefore, based on the equation (Eq 2.11),

membranes with high hydrophobicity (high contact angle), small pore size, low surface energy, and high surface tension for the feed solution have a high LEP value. The maximum recommended pore size to avoid wetting is between 0.1–0.6  $\mu\text{m}$  [25]. It is worth mentioning that a small pore size causes low membrane permeability which confirms the necessity of a tradeoff between the high LEP and the high distillate flux by considering a proper pore size and pore size distribution [80]. Furthermore, in VMD, small pore size is recommended since the possibility of liquid penetration into membranes' pores in VMD is higher than other MD configurations [25].

### **2.3.5 Thermal Conductivity**

In MD system, membrane material should have low thermal conductivity in order to reduce the heat loss by conduction through the membrane. Generally, higher thermal conductivity causes lower energy efficiency and distillate flux. The thermal conductivity of PTFE, PP, and PVDF polymers are in the range of 0.25–0.27, 0.11–0.16, and 0.17–0.19 W/m. K, respectively, at 23 °C [85]. Therefore, most hydrophobic membranes' thermal conductivity are close to each other and ranges from 0.04 to 0.06  $\text{W}\cdot\text{m}^{-1}\cdot\text{K}^{-1}$  depending on their porosity [80]. Porosity has important effect on the thermal conductivity of porous membranes while an increase in porosity leads to a decrease in thermal conductivity [70]. Al-Obaidani et al. [23] calculated the reduction of distillate flux up to 26% and thermal efficiency up to 50% by increasing thermal conductivity from 0.1 to 0.5  $\text{W}\cdot\text{m}^{-1}\cdot\text{K}^{-1}$  in DCMD.

### **2.3.6 Chemical and Thermal Stability**

Chemical stability of the membrane has an important influence on its long-term operation. Membrane surface structure could be affected by any reaction between membrane material and the solution. Therefore, high chemical stability of membranes is required for MD

process [86]. Furthermore, thermal stability is another important property of membrane material in MD systems as MD is thermally driven process and the membrane is in direct contact with high temperature solution. For amorphous polymers, over glass transition temperature (i.e.,  $T_g$ ), the polymers' properties change significantly. For example,  $T_g$  of PTFE membrane is 126 °C which indicates high thermal stability of this membrane in MD systems. Generally, the factors that increase the  $T_g$  of the membrane can improve both its chemical and thermal stability. Therefore, in conformity with long term stability, membrane with suitable  $T_g$  should be utilized [86].

## **2.4 Operating Parameters**

This section includes the effect of fundamental operating variables on the distillate flux in MD systems.

### **2.4.1 Feed Solution Temperature**

The influence of the feed solution temperature on distillate flux has been extensively investigated in the different MD configurations [56,64,65,87–91]. It has been proved that the feed solution temperature has a significant effect on increasing distillate flux as the vapor pressure increases exponentially with temperature based on Antoine equation [27]. In addition, based on Srisurichan et al. work [91], the mass transfer coefficient through the membrane increases by working at high temperature since diffusivity and temperature have direct relation. Therefore, higher distillate fluxes can be obtained at higher temperatures in MD process, while higher temperatures need higher heating energy consumption and increase TP effects.

### 2.4.2 Feed Inlet Concentration

As it is well acknowledged, MD can be utilized for the treatment of extremely concentrated solutions without encountering the large decline in the permeability in contrast to the other desalination processes as RO [26]. However, in MD systems, the partial vapour pressure decreases by increasing the feed inlet concentration according to Raoult's law (Eq. 2.12), leading to decreases of the MD process driving force [26,92].

$$P^s = (1 - X_i)P^v \quad \text{Eq. 2.12}$$

In which  $X_i$  is the solute mole fraction in the liquid,  $P_v$  is the pure water vapour pressure at the feed temperature, and  $P^s$  is the partial water vapour pressure at the same temperature [93]. Qtaishat et al. [93] showed about 12% decline in distillate flux by increasing the feed (NaCl) concentration from 0 to 2 Molar.

### 2.4.3 Feed Flow Velocity

Feed flow velocity is one of the important operating parameters in MD processes. It has been shown that the elevated feed flow velocity results in increasing the heat transfer coefficient and mixing in the feed side and decreasing TP and CP, leading to higher MD distillate flux [26]. Ferna et al. [94] demonstrated that operating under turbulent flow regime, which can be obtained in higher flow velocity, resulted in reaching a higher productivity. At higher flow rates, the temperature at the membrane surface reaches close to the bulk feed temperature that will be followed by higher transmembrane temperature difference [26].

## 2.5 Fouling

While fouling in the MD process is less than fouling in conventional pressure-driven membrane separations (i.e., RO), similar to all other membrane processes, membrane

fouling in MD has been known as an important challenge. Fouling decreases the membrane process efficiency by decreasing the distillate flux over time and changing membrane pore structure along with surface properties, leading to wetting of membrane pores [46,47]. Inorganic fouling (i.e., scaling) and organic fouling are main types of fouling in MD process that may block the membrane pores and subsequently decrease the distillate flux. Decrease of distillate flux due to the membrane biofouling which occurs in the other membrane processes as NF, UF, and RO, does not happen in such intensity in MD process because of its operating conditions. The high temperature and salinity of MD process can inhibit the extensive microbial growth, leading to decrease of the biofouling impact.

In MD systems, scaling by precipitation and accumulation of inorganic soluble salts such as  $\text{CaSO}_4$  and  $\text{CaCO}_3$  is known as a critical problem by hindering of water vapor diffusion across the membrane [48–50]. In addition, scale layers on the membrane surface can intensify the effects of TP and CP in MD, thus reducing the active surface of membrane for water evaporation and so notably decreasing water flux [51,52]. The water composition, flow velocity, degree of supersaturation, and temperature have been recognized as governing factors for scale formation rate [95,96]. Controlling and removing  $\text{CaSO}_4$  scaling was shown difficult in comparison to  $\text{CaCO}_3$  [53]. While  $\text{CaCO}_3$  typically precipitates and adheres to heat exchangers and tubing prior to entering the filtration module,  $\text{CaSO}_4$  was shown to form suspended crystals that may reach the membrane surface and deposit on it as scaling [54]. Nghiem et al. [96] showed that membrane scaling occurred by  $\text{CaSO}_4$  was comparatively higher than scaling by  $\text{CaCO}_3$  and led to distillate flux decline by up to 92% following a 40 h experiment [96]. In addition, the elevated feed solution temperature, which is required for MD processes, was shown to increase the rate of  $\text{CaSO}_4$

crystallization [97] (i.e., inverse solubility at  $T > 50$  °C [53,98]). Up to now, multiple MD studies have been done on controlling and limiting membrane scaling [30,96,98–103], leading to control and treatment pathways, including membrane surface modification, pre-treatment of the feed solution, and finally membrane descaling and cleaning through chemical treatment [104–108]. Despite a large number of studies on MD scaling, limited work has been done on MD scaling of high saline water, such as found in RO brines or produced water.

Furthermore, in terms of organic fouling, natural organic matter (NOM) has been known as one of the major sources of distillate decline [109]. NOM includes low molecular weight (LMW) to high molecular weight (HMW) organic compounds, measured as a dissolved organic carbon (DOC). In seawater, humic materials are the main components of NOM, in addition to the protein, carbohydrates (containing polysaccharides), and a range of acidic and LMW species [110]. However, fouling by humic substances in MD process was shown to not be harsh compared to RO process (i.e. osmotic pressure-based separation), mostly due to the driving force differences which is vapor pressure in MD [111]. Operating conditions, feed solution and NOM composition, and membrane characteristics have been shown to impact organic fouling in MD systems [112]. It was shown that the thermal heating process of MD can influence humic characteristics as it disaggregates the humics to lower molecular size substances or other organics [113].

## **2.6 Recent Advanced MD Systems for Overcoming Temperature Polarization**

**Preface:** The contents of this section are in part based on a published review article in Journal of Membrane Science: **Anvari, A.**, Yancheshme, A.A., Kekre, K. M., Ronen, A.,

"State-of-the-art methods for overcoming temperature polarization in membrane distillation process: A review", *Journal of membrane science* (2020): 118413 [114]:

Here, we present recent advancements in MD technology targeted to lower or eliminate TP. These are categorized into three sections and include advanced membranes, flow promoters, and self-heated MD systems.

### **2.6.1 Membrane Modification**

MD separation processes include a hydrophobic microfiltration membrane designed to enable water vapor movement while preventing liquid transport through the membrane. As described in the previous section, membrane properties play a vital role in distillation efficiency. These include the membrane's physical characteristics, selectivity, membrane surface-vapor molecules interactions, and thermal properties along with their subsequent effects on both temperature polarization and mass transfer. In the last decade, multiple approaches have been used to modify MD membrane surfaces, including grafting macromolecules on the membrane surface, blending polymers and nanomaterials, and coating the membrane's surface [115–121]. These are noted as they are relatively common and designed to enhance MD performance (e.g., permeability and selectivity) but were not specifically tailored to mitigate TP. Membrane modifications designed to reduce TP are presented in this section.

Recently, nanostructured membranes were developed to enhance MD efficiency [122–129]. Among nanomaterials, carbon-based nanoparticles (CNPs) with high thermal conductivity such as carbon nanotubes (CNTs) and graphene, have an important role in decreasing TP and enhancing MD performance. Coating polymeric membranes with a CNPs layer increases the thermal conductivity across the membrane surface (i.e., surface

plane) without impacting the thermal conductivity of the bulk membrane, resulting in reduced heat losses.

CNTs have high thermal conductivity (about  $10^3$  W/m. K based on their structure [130]) in addition to various chemical functional groups [131] that may provide mass transport pathways through the membrane. Only lately (i.e., in the last seven years), membranes modified by CNTs have been used as part of MD systems to improve desalination performance by lowering TP and increasing distillate flux [122,126,127,132–134]. Roy et al. (2014) [134] tested a dual-layered hydrophilic-hydrophobic membrane as part of a DCMD system. The fabricated composite membrane had a hydrophilic layer based on carboxylated functionalized multiwall CNTs (CNT-COOH) immobilized on a hydrophobic polypropylene support membrane. The top hydrophilic layer was thermally conducting and functioned as an extra barrier to reduce heat and energy losses [134] while simultaneously increasing membranes' selectivity by decreasing the hydrophobic layer pore wetting [135–137]. While TP is not directly discussed in this work, the thermally conductive layer resulted in high distillate flux, about 51.5% higher than the unmodified membrane, and improved the thermal stability of the membrane.

In terms of TP reduction, Bhadra et al. (2016) [132] addressed the impact of a thermally conductive CNTs layer on the enhancement of the liquid temperature at the membrane's surface. Hydrophobic octadecyl amine CNTs (CNT-ODA) were immobilized on the feed side of the membrane and hydrophilic CNT-COOH on the permeate side of the membrane (Figure 2.3a) [132]. CNT-ODA improves water vapor adsorption by making polar-polar interactions through carbonyl and amine groups, and simultaneously it increases salt ions rejections by repelling liquid solution as the CNT-ODA has a hydrophobic nature. The

presence of the hydrophilic CNT-COOH on the permeate side resulted in the interaction of the COOH group with water vapor molecules, leading to faster water vapor desorption and more distilled water production. In addition, the high thermal conductivity of CNTs on both sides of the membrane surface enhanced  $T_{fm}$  and diminished  $T_{pm}$  (i.e., the temperature of the feed and distillate fluids at the membrane interface), while the overall thermal conductivity of the hydrophobic membrane remained low as CNTs did not entirely fill the pores. Overall, TP reduction in addition to enhancing water vapor interactions as a result of the CNTs layer resulted in up to 70% increase in distillate flux in comparison to a conventional membrane and 37% increase in comparison to a modified membrane with CNTs immobilized only at the feed side.

In addition, graphene oxide (GO) modified membranes have been used in MD as well, [124,125,138] as GO nanoparticles have relatively high thermal conductivity (about 5000 W/m. K). GO coating has not been widely assessed for MD applications [124,125,138], and the current research mainly addresses the hydrophilic nature of GO, resulting in better water molecules and membrane surface interactions and thus increased flux (Figure 2.3b). Graphene has water vapor sorption sites through hexagonal honeycomb lattices containing sp<sup>2</sup>-bonded carbon atoms in addition to the polar functional groups (i.e., hydroxyl and carboxyl), leading to improved interactions between the membrane and water vapor and consequently enhanced water vapor flux. Furthermore, the hydrophilicity of GO was shown to decrease the interactions between GO and foulants, resulting in lower fouling of GO modified membranes and, consequently, higher flux [139,140]. In addition, GO with hydroxylated and carboxylated carbon atoms was shown to have selective sieving of water and salt ions [124,141]. Besides interaction with water molecules, TP reduction mechanism

of GO layer is similar to CNTs and based on providing a thermally conductive layer on top of the polymeric film. TP reduction and selective sorption of water vapors by the GO layer led to an increase in distillate flux up to 64% in comparison to a pristine membrane [124].

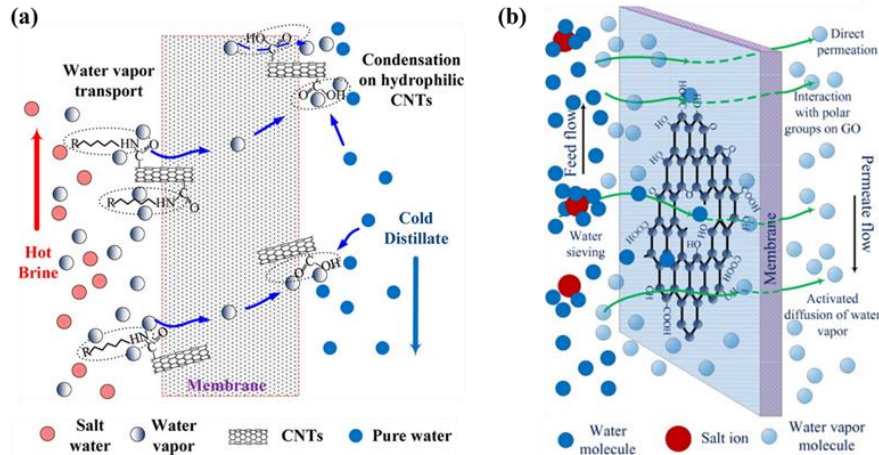


**Figure 2. 3.** (a) CNTs bilayered membrane and water vapor transport mechanism (Reprinted with permission from Ref. [132], Copyright (2016) American Chemical Society); (b) GO membrane and water vapor transport mechanism (Reprinted from Ref. [124]).

A novel approach to mitigate TP is by coating the membrane's surface by photonic nanomaterials [142–144] that can emit heat when exposed to varying wavelengths of radiation (visible, UV, and IR). While these modified membranes reduce TP, they still require a preheated feed solution and, therefore, are not considered as 'self-heated' systems, which are further discussed in section 2.6.3.1.

Politano et al. (2017) [142] used flat PVDF microporous membranes incorporated with silver (Ag) nanofillers to overcome TP and thermal boundary layer effects. By exposing the membranes to UV irradiation at a wavelength around the Ag NPs' plasmonic intensity (366 nm), they are converted to nano-heaters. This resulted in elevated temperature of the membrane-water interface and a TPC of unity (i.e., 1.065) [142]. In addition, the produced thermal energy of Ag NPs increased the outlet feed temperature by up to 4 °C more than

the inlet feed temperature, while for the pristine membrane, the outlet temperature was lower than the inlet as a result of heat losses along the membrane length [142]. Therefore, the presence of UV activated Ag NPs as nano-heaters on the hydrophobic membrane surface leads to a decline in TP and enhanced distillate flux up to 11 times higher than pristine membrane under no irradiation condition (i.e., distillate flux of 25.7 kg/m<sup>2</sup>.h for Ag coated PVDF membrane under UV irradiation compared to the distillate flux of 2.2 kg/m<sup>2</sup>.h for the pristine PVDF membrane without irradiation). In addition to Ag NPs, antimony doped tin oxide (ATO) NPs have been blended with hydrophobic PVDF membranes to increase the surface temperature of the membrane under IR radiation (Figure 2.4a). Owing to the high light absorption properties of ATO NPs, a PVDF/ATO hybrid nano-fiber membrane was successfully used to reduce TP by heating the solution at the membrane-water interface. This was done in addition to preheating the bulk solution up to 70 °C [144]. Similar to photonic Ag NPs, the heat produced by the hybrid membranes elevated the surface temperature of the membranes by up to 13 °C, leading to increased TPC values higher than unity (i.e., 1.161). Distillate flux analysis revealed that ATO NPs increased the permeate flux by 200% while the mechanical strength and porosity of the hybrid membranes declined [144]. Even though the results proved the possible application of these membranes for enhanced seawater desalination using solar energy, the system was not proven to be energetically preferred as it still requires preheating of feed solution to 70 °C in addition to the IR irradiation (100 W).

Besides NPs, novel 2-D metal hybrid materials with advanced properties may be used for mitigating TP. For example, MXene is a 2D metal hybrid (Figure 2.4, b1 and b2) with excellent thermal properties, photonic absorption, and semiconducting properties [145],

which make it practical for heating by irradiation and therefore TP reduction [146]. The photothermal efficiency of MXene over NPs was proven by exposing a MXene-coated PVDF membrane to one min of 50 W LED light (equal to  $5.8 \text{ kW/m}^2$ ), resulting in an increase in surface temperature by up to  $49 \text{ }^\circ\text{C}$  (Figure 2.4, b3). While the MXene coated membrane showed photonic conversion efficiency of around 43%, the increased distillate flux was not significant (around 10%) [146] as a result of the additional coating layer and the increased mass and heat transfer resistances. To increase the flux and obtain similar efficiency as the pristine PVDF membrane under similar conditions, the feed solution was preheated to  $65 \text{ }^\circ\text{C}$ .

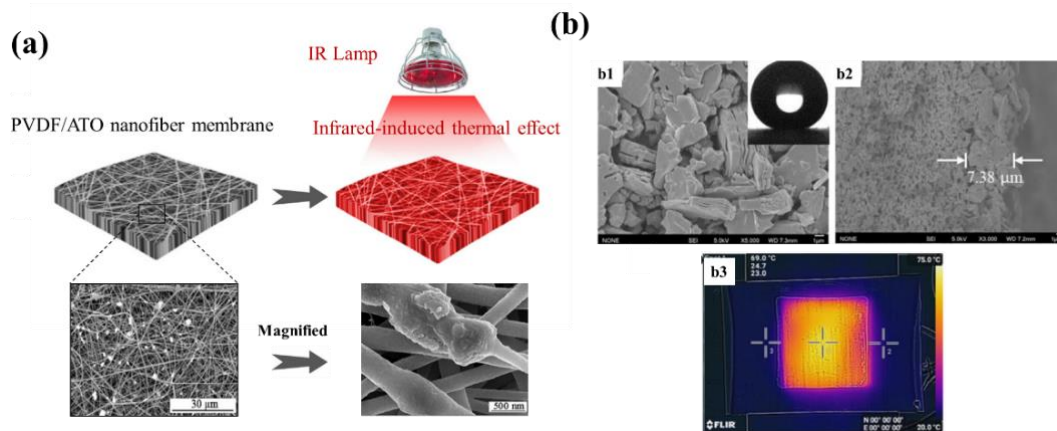


**Figure 2. 4.** (a) Schematic diagram of PVDF/ATO membranes, including IR irradiated and SEM images (Reprinted from Ref. [144], Copyright (2019), with permission from Elsevier); (b) FESEM images of MXene coated PVDF membrane: (b1) surface and (b2) cross-section and (b3) IR thermal image of MXene-coated PVDF membrane after 1 min of light irradiation (average initial temperature of  $22 \text{ }^\circ\text{C}$ ) (Reprinted from Ref. [146], Copyright (2018), with permission from Elsevier).

## 2.6.2 Flow Promoters

Another approach to reducing TP is by enhancing the characteristics of the feed flow, including flow rates and stream turbulence. While efficient, increasing flow rates is not energetically favorable, as more energy must be utilized to provide higher flow rates. In

addition, high flow rates may lead to internal pressure in the flow channel, exceeding the liquid entry pressure (LEP) of the hydrophobic membrane and leading to a decrease in membrane selectivity [147,148]. Furthermore, high flow rates may lead to high shear stress and eventually cause physical damage to the membrane's active layer [147]. To overcome flow rate limitations, frame-like turbulence promoters (i.e., feed spacers) have been demonstrated as alternative methods to improve flow characteristics, resulting in reduced TP and enhanced MD performance [149,150].

Spacers are used to improve the mixing in the vicinity of the membrane's surface, leading to a reduction in the thermal boundary layer thickness [74,151,152] and an increase in the distillate flux by enhancing the heat transfer coefficient, i.e., decreasing TP [76,153]. Although the presence of feed spacers may also lead to a pressure drop in the filtration channel, as a result of kinetic losses by directional changes of the flow and drag produced by the spacer, the lower TP and higher distillate flux were shown to overall decrease the specific energy requirement and subsequently improve the energy efficiency of MD systems [147]. Spacer's orientation along with its geometric properties (e.g., spacer porosity ( $\epsilon$ ), filament diameter ( $d$ ), and filament distance ( $H$ ) (Figure 2.5a)) were determined to have a significant effect on the mass and heat transfer and consequently distillate flux values [151,154–160].

The influence of spacers on TP and the overall MD performance has been evaluated using both experimental work and numerical simulations. For example, Kim et al.[147] evaluated five types of polymeric non-woven net feed spacers, with varying mesh sizes and porosity. Results show a maximum of 43% increase in distillate flux by utilizing the thinnest and densest spacer (i.e., high number of thin filaments or lower porosity) in comparison to

empty flow channels (i.e. no spacer). The increase in MD performance was determined to be a result of the enhanced heat transfer coefficient across the membrane's boundary layers and reduced TP. This was shown to be specifically important for heated feed flows with elevated temperature, which typically lead to a more severe TP [147].

The importance of spacers on controlling the heat transfer coefficient was also addressed by Taamneh et al. (2017) [152] using numerical simulations. Results showed that the spacers' filament orientation might increase the average shear stress and heat transfer coefficient by up to two times in comparison to an empty feed channel [152]. Figure 2.5b shows the results of numerical simulations addressing the heat transfer coefficient (Figure 2.5, b1) and shear stress (Figure 2.5, b2) for a feed channel with and without a spacer. In addition, it was determined that the filament orientation had a notable effect on quantity improvements of the heat transfer. Therefore, a higher degree of turbulence and consequently, convection heat transfer were achieved with a high angle of filament orientation. A 45° orientation of spacer filaments to the flow direction obtained the best performance in terms of heat transfer and distillate flux [152]. Similar trends have also been shown in additional studies [155,159].

Recently, three-dimensional (3D) printing technology has been effectively used to design optimized feed spacers for enhanced MD systems [161–163]. Thomas et al. (2018) [162] utilized 3D printing to fabricate five different triply periodic minimal surfaces (TPMS) based spacers (Figure 2.5c) for enhanced MD. TPMS spacers are different than conventional polymeric spacers as they have a special design by combining the interpenetrating networks and having zero mean curvature, leading to an increase in turbulence and decrease TP [164]. Following fabrication, the TPMS spacers were assessed

according to their impacts on the heat and mass transfer in a DCMD system. Results show that TPMS based spacers led to an increase in distillate flux and heat transfer coefficient by up to 60% and 63%, respectively, in comparison to commercial spacers.

The spacer's orientation and geometrical properties described above addressed polymeric spacers, mainly composed of polypropylene (PP), which are thermally non-conductive. However, the spacer material (i.e., metallic or polymeric) was shown to have a significant impact on the thermal boundary layer and distillate flux by decreasing TP along the membrane length [165,166]. Tan et al. (2019) [166] assessed the impact of two metallic feed spacers made of nickel and copper on distillate flux in a DCMD system. Both spacers had high thermal conductivity and varying spacer densities (3 mm and 1.5 mm mesh and foam, Figure 2.5d). The metallic spacers were able to maintain higher uniform temperatures along the surface of the membrane in comparison to a polymeric feed spacer, with the highest temperature obtained for the dense metallic foam. Furthermore, the metallic foam also reduced the specific energy (i.e., lower input energy per unit amount of distillate) of the MD process [166]. This was explained to be a result of the higher spacer density, providing higher thermal conductivity and subsequently higher heat accumulation. It can be inferred that metallic spacers can effectively improve heat transfer, leading to lower TP. However, as distillate flux is still relatively low in comparison to systems with polymeric spacers, additional research is required to understand transport phenomena in metallic spacer filled channels and to optimize their design to achieve higher distillate flux.

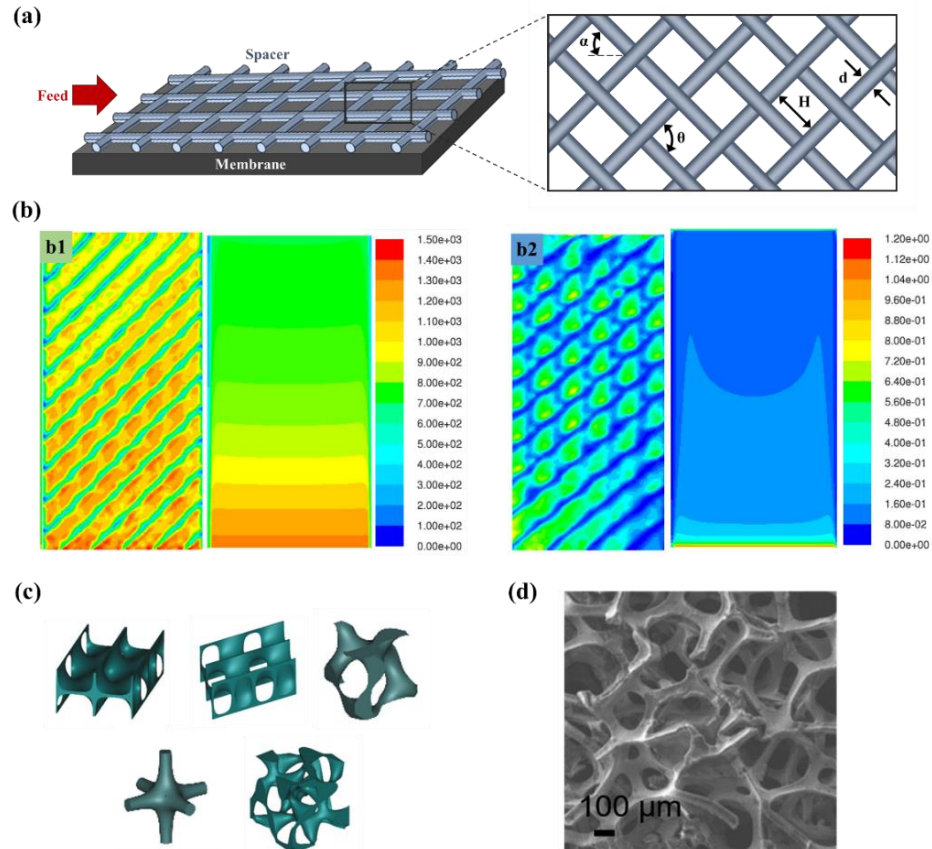


**Figure 2. 5.** (a) Schematic of feed spacer and its structural parameters; (b) Simulation results of (b1) heat transfer coefficient ( $\text{W}/\text{m}^2\cdot\text{K}$ ) and (b2) shear stress (Pa) for spacer filled channels (left side) compare to the empty channel (right side) (Reprinted from Ref. [152], Copyright (2017), with permission from Elsevier); (c) Different configurations of 3D-printed spacers (Reprinted from Ref. [162], Copyright (2018), with permission from Elsevier) (d) SEM image of metallic foam (Reprinted from Ref. [166], Copyright (2019), with permission from Elsevier).

### 2.6.3 Self-heating MD Systems

Recently, novel approaches have been developed to directly heat the feed solution on the membrane's surface or in the vicinity of it, to overcome TP and enhance MD performance in terms of distillate flux and energy efficiency. In addition to high flux, these systems have eliminated the need for expensive heat management resulting from metal corrosion and scaling of heat exchangers in the preheating process. In self-heated systems, the feed is heated in the membrane module and prevents the need for preheating a large volume of the

bulk solution. Heating of the membrane's surface has been mainly done by photothermal heating (solar) and Joule heating (Ohmic heating). In all methods, the inlet feed temperature is typically at room temperature or varied between 20-35 °C, which is significantly lower than typical MD systems with feed at 60-70 °C.

### **2.6.3.1 Photothermal Heating (Solar)**

The use of renewable energy in MD technology has been gaining interest as a potential substitute for conventional fossil-fuel energy to minimize energy consumption, cost, and environmental footprint. As MD technology can operate at a low-temperature gradient, solar heating can be considered as an effective renewable, and environmentally friendly heat source for thermal evaporation energy [167–171]. Generally, solar-driven MD systems use localized heating to reduce the external energy added to the thermal evaporation process. In conventional MD solar systems, the feed solution is heated either prior to entering the membrane module using a solar energy collector or directly in the membrane module by placing a solar absorber above the feed channel or using photothermal nanofluids as the feed solution [171–177].

While these approaches are able to decrease the energetic cost, they still produce a relatively low distillate flux as they are impacted by TP limitations. Recent solar MD systems use localized solar heating based on a photothermal effect to overcome TP. When the photothermal material is exposed to light, it generates heat at the membrane-feed interface, resulting in water vaporization and a significant decrease in TP. Furthermore, as heating is done directly at the membrane surface, no preheating of the bulk feed solution by external heaters is required. Figure 2.6a shows a schematic diagram of a solar-driven DCMD system.

In terms of the developed solar absorbers, photothermal nanoparticles (e.g., silver and carbon black NPs) coated on the membrane surface have been used to produce localized heating and increase the temperature of the feed solution directly on the membrane surface under light irradiation [142,143,178,179]. Politano et al. (2019) [143] presented a metal nanostructure modified membranes containing silver nanoparticles (Ag NPs), and plasmonic excitation of the Ag NPs under ultraviolet radiation (irradiance of 23 kW/m<sup>2</sup>) was shown efficient in heating the membrane surface and reducing TP. NPs' size was shown to influence the absorption of light so that an optimum NPs' size should be calculated based on the balance between temperature increase and plasmonic absorption. Moreover, achieving a homogeneous size distribution and a suitable degree of dispersion should be considered during the synthesis of NPs to attain the maximum heating efficiency. Ag NPs modified membranes, as described by Politano et al. (2017) [142], require an optimum size in the range of 25-35 nm with an average of 31 nm based on the ideal trade-off between the effects of size on temperature increase and plasmonic absorption. In addition to size, NPs' quantity was shown to impact the heating rate and, consequently, interfacial temperature values. The higher quantity of NPs (i.e., higher number density) exhibited higher interfacial temperature and TPC values [143]. As a result, hydrophobic membranes modified with 25 wt.% Ag NPs showed the best MD performance in terms of TPC (i.e., values more than unity, 1.065) and distillate flux (i.e., around 9 to 11 times higher than pristine membranes) while the initial feed temperature was 30 °C [143]. While these results are encouraging and prove the possible application of solar-heated membranes for distillation, their energy efficiency, described as the water evaporation heat flux over the total heat flux, including plasmonic heat flux, was relatively low (i.e., 28.4 %). In another

study, Ye et al. (2019)[179] embedded 20 wt.% of 16-40 nm Ag NPs at the surface and inside a hydrophobic electrospun nanofibrous membrane. The NPs were heated by UV-light irradiation (50 W, 3.2 kW/m<sup>2</sup>) and assessed in a continuous DCMD configuration with a 3.5 wt.% NaCl feed solutions at 20 °C. Results indicate a relatively high distillate flux of 2.5 kg/m<sup>2</sup>.h with a high energy efficiency of 53 ± 7% [179] in comparison to other Ag NPs membranes [143]. While Ag NPs proved efficient for photothermal self-heated MD processes, the system's long-term operation and commercial desalination potential is still limited as Ag NPs may leach to the solution over time.

Carbon black (CB) NPs were also evaluated as photothermal nanomaterials under sunlight irradiation and shown to directly heat the feed solution at the membrane-water interface, leading to TP reduction [178]. Dongare et al. (2017) [178] fabricated a CB NPs-embedded polyvinyl alcohol (PVA) membrane to provide localized heating under solar illumination. The CB-PVA membrane, designed as a dual-layer hydrophilic/hydrophobic structure, proved efficient with increased distillate flux (0.5 kg/m<sup>2</sup>. h) and high salt rejection. This is a result of the composite hydrophilic PVA porous layer on the hydrophobic PVDF membrane and a coated layer of plasmonic CB NPs (Figure 2.6b). This system reduces the need for bulk feed preheating and extensive power requirements in comparison to conventional MD systems [178]. Similar to other photothermal NPs embedded membranes, the photosensitive properties of CB NPs dispersed into PVA solution were optimized (5.5 wt.%) based on the highest distribution and efficiency of absorbed energy. In addition to NPs loading, the system had higher flux efficiency for higher ambient temperatures, higher module's length and width, and lower flow velocities as the direct heating of the membrane is influenced by the water-CB NPs contact time. When exposed to a 0.7 kW/m<sup>2</sup> irradiance,

the smaller module (8.1 cm × 3.48 cm) displayed a solar efficiency of 21.5% at an ambient temperature of 25 °C, whereas the larger module (100 cm × 10 cm) displayed increased solar efficiency to the extent of up to 53.8% at an ambient temperature of 40 °C [178]. In another study by Wu et al. (2017) [180], higher photothermal efficiency (greater than 74.6%) was attained for a self-assembled photothermal CB NPs based membranes under simulated sunlight (1 sun unit, 1.3 kW/m<sup>2</sup>) which was higher than the solar efficiency of Ag NPs membranes.

Additional research has shown that while photothermal NPs may increase the flux and reduce TP, a thick deposited layer may lead to pore blocking and flux decline. Wu et al. (2017) [180] evaluated a photothermal MD process based on NPs and compared two membrane coatings. SiO<sub>2</sub>/Au nano shells-based membranes were compared to self-assembled CB membranes. While both photothermal membranes exhibited a compelling increase of up to 33% in the permeate flux when irradiated, their overall flux efficiency was lower than the control membrane when no irradiation was applied as a result of pores blockage. Comparison of the two NPs showed solar efficiency of 40-43% for low concentration of CB NPs (0.1 wt./vol.%) and high concentration of metal nanoshell (SiO<sub>2</sub>/Au), accordingly, while the high concentration of CB NPs (0.5 wt./vol. %) had an overall solar efficiency greater than 74.6%. In addition, TPC analysis compared to ‘no irradiation’ condition confirmed the impact of photothermal irradiation on TP reduction. Low concentration of CB NPs and high concentration of SiO<sub>2</sub>/Au increased TPC by up to 15%, while a high concentration of CB NPs increased TPC by about 33% [180].

Furthermore, a vapor gap MD system was developed by Gong et al. (2019) [181] to increase solar energy efficiency while preventing pore blockage as the result of high

loading of photothermal NPs on the membrane surface. Light absorption and localized heating occurred on free-standing graphene–nickel foam, which was placed above a membrane. This structure allowed water vapor to diffuse into the gap and pass through the membrane. Results showed that under the illumination of  $1 \text{ kW/m}^2$ , thermal energy was effectively transferred in the thin water layer in the graphene nanochannels, leading to the high solar energy efficiency of 73.4% and high distillate flux ( $1.1 \text{ kg/m}^2\cdot\text{h}$ ). To further improve the solar efficiency and heating, Alabastri et al. (2020) [182] coupled a solar-heated MD process with a dynamic heat recovery system (Figure 2.6c). In this system, heat exchange between the distillate and feed allowed recovery of the condensation heat from the distillate and reusing it to preheat the feed. A CB NPs-embedded PVDF membrane was heated under  $0.475 \text{ kW/m}^2$  irradiation through light-absorbing photonic CB NPs, resulting in direct heating of the feed solution with an initial temperature of  $25 \text{ }^\circ\text{C}$ . Heating was done at the membrane-water interface, and the distillate heat was recovered using an aluminum or copper sheet, as a heat exchanger in contact with the feed solution (Figure 2.6c). Results show reduced TP and relatively high distillate flux ( $1.1 \text{ kg/m}^2 \cdot \text{h}$ ), leading up to a 500% increase in comparison to a solar-heated system without a heat exchanger.

Overall, surface heating obtained by the coated photothermal NPs demonstrated enhanced thermal efficiency and reduced TP. However, the obtained distillate flux values are still low for large scales applications and require additional optimization in terms of material engineering and synthesis of plasmonic NPs with optimal properties (e.g., size, concentration) and absorption coefficient. Furthermore, membrane modification may still lead to pore blockage along with long-term limitations such as particle leaching. Therefore, in addition to NPs, photonic materials with notable light absorption and high photothermal

conversion properties should be considered. In this manner, polydopamine (PDA) and bio-derived eggshell membranes are described as potential materials for solar-driven MD applications [183,184]. As Polydopamine (PDA) has notable light absorption, high photothermal conversion properties, and is easy to apply on polymeric membranes, it has been selected as an appropriate material for solar MD systems [183]. Photothermal coating of PDA on a hydrophobic membrane showed a higher solar conversion efficiency (45%), under  $0.75 \text{ kW/m}^2$  illumination, compared to silver NPs (28.4%) [143], nitrocellulose (31.8%) [185], and CB NPs (21.5%) [178] (at ambient temperature of 20-25 °C). The higher efficiency could also be influenced by the high density and uniformity of the PDA coating.

Another novel membrane used for photothermal applications is a 'green' bio-derived free-standing membrane, produced from daily bio-waste of eggshells. Eggshell is an efficient material for heat localization with long-term stability for repeated usage in the solar-driven MD process, as it has large broadband photo-absorption with high localized heating properties [184]. In addition, the use of eggshells for membrane fabrication is cost-effective and sustainable. The eggshell membranes can be obtained by dipping raw eggshells in the hydrochloric acid aqueous solution overnight to remove all hard-inorganic components from eggshells. Han et al. (2019) [184] fabricated carbonaceous membranes (cESM) through modification of eggshell membranes with graphene oxide and carbon nanotubes (CNTs), both having high thermal and electrical conductivity. The cESM-CNTs membrane was observed to have the highest (99%) photo-absorption efficiency in the UV, IR, and visual spectra. Therefore, both the photothermal effect and the thermal conductivity led to high energy efficiency (75.6% under  $1 \text{ kW/m}^2$ ) but relatively low distillate flux in the range

of 1.11 kg/m<sup>2</sup>.h for seawater desalination. The attained flux and efficiency for cESM membranes were reported to be 2.52 times higher than a pristine PVDF membrane and higher than previous studies on solar MD using CB NPs [184]. Despite the higher energy efficiency of the proposed material, the distillate flux was still very low. Therefore, this novel material requires additional optimization in terms of size and concentration.

In addition to advanced photothermal materials, solar driven-MD can be enhanced by the optimization of the optical design to increase the efficiency/number of photons reaching the heated material. Dongare et al. (2019) [186] demonstrated an effective enhancement in distillate flux of a solar MD system by focusing the sunlight into hot spots on the photothermal membrane. This was done by arranging a lens array with diameters of 1 and 2 inches (Figure 2.6d) on the surface of CB coated PVDF membrane while the input energy (i.e., solar energy of 0.7 kW/m<sup>2</sup>) was constant. Results showed an increase in distillate fluxes up to 38% and 58% with 1- and 2-inches lens arrays, respectively, in comparison to the solar-driven MD system in the absence of any lenses (Figure 2.6e). The increased distillate flux was a result of increased surface temperatures at the focused spots, which was highest for the larger lens, as the saturation vapor pressure is exponentially dependent on the temperature [186].

To summarize, the incorporation of photothermal materials and localized heating under solar irradiation can raise and maintain the temperature of the feed solution at the membrane–water interface. Consequently, these solar-based MD systems can provide high energy efficiency along with desalination performance, whereas the distillate fluxes are still low. The current photothermal materials have several limitations (e.g., leakage, pore blockage) that prevent their further advancements. In addition, the commercialization of

solar-based MD is still challenging as they are able to operate only when exposed to light (i.e., only during sunny days) and a large membrane surface area is required to receive adequate solar or UV energy, thus, leading to large scale treatment plants with a high capital cost.

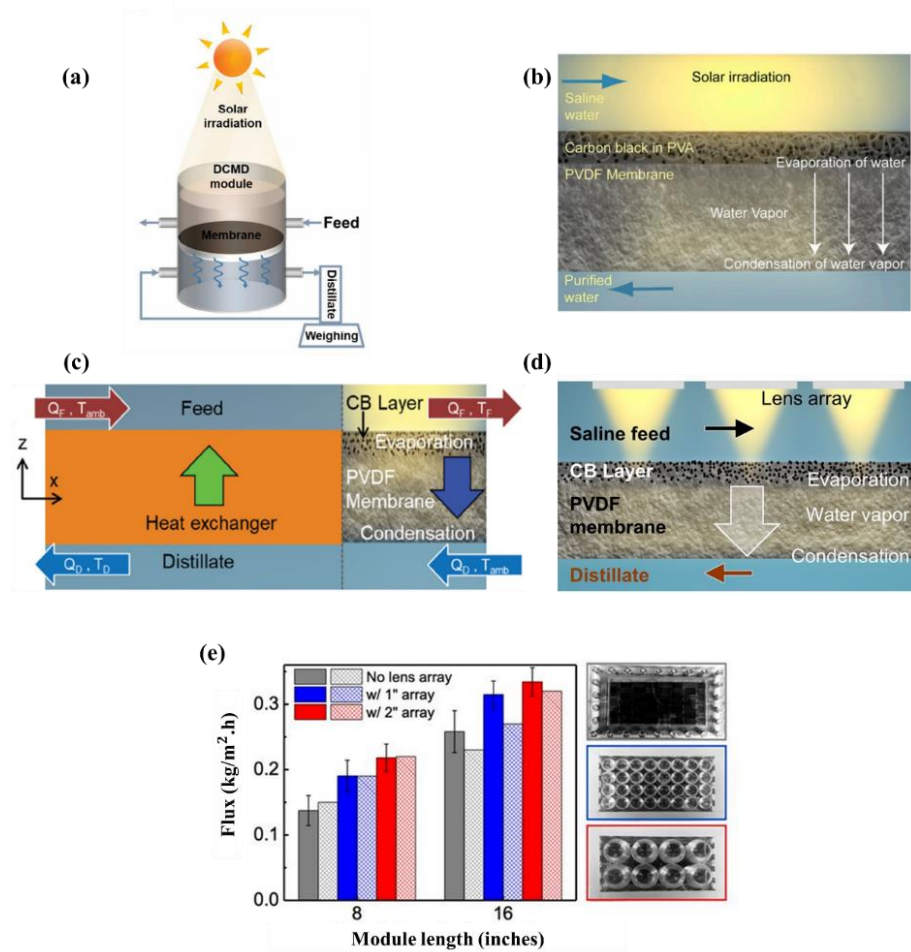


**Figure 2. 6.** (a) Schematic of the solar-driven DCMD system (Reproduced from Ref. [183], Copyright (2018), with permission from the Royal Society of Chemistry); (b) CB-PVDF dual-layer membranes used in solar-driven system [178]; (c) Schematic of the solar-driven DCMD system coupled with a dynamic heat recovery (HX) system,  $Q_F$  and  $Q_D$  represent the feed flow and distillate flow, respectively (Reproduced from Ref. [182], Copyright (2020), with permission from the Royal Society of Chemistry); (d) Schematic of a solar-driven MD system under focused illumination [186]; (e) Impact of light focusing on distillate flux in solar-driven MD system [186].

### 2.6.3.2 Joule Heating

Joule heating (Ohmic heating) is the production of heat by passing an electrical current through a medium (liquid or solid) with limited conductivity [187]. In Joule heated MD process [188], the temperature gradient required for water evaporation could be provided directly on the membrane surface. The membrane surface needs to be electrically conductive, but with some resistivity to allow surface heating. CNTs have been shown efficient for Joule heating as they are relatively cheap with high thermal and electrical conductivity in conjunction with medium resistance [189,190] and can be used as a Joule heating element (Figure 2.7a). Dudchenko et al. (2017) [188] developed a conductive hydrophilic/hydrophobic composite membrane (Figure 2.7b) as an applicable Joule heating element for DCMD process. The porous CNTs layer was spray-coated layer by layer on a hydrophobic PTFE membrane with crosslinking of polyvinyl alcohol (PVA). Similar to other [134–136] dual-layer hydrophilic–hydrophobic membranes, the hydrophobic layer prevents liquid transport (i.e., attaining high salt rejection around 99%) while vapor formation occurs at the hydrophilic layer. When an electric current was applied through the CNTs layer, it heated up and conducted heat to the liquid, thus, directly heating the saline solution at the membrane-water interface (Figure 2.7c). Results show that a high frequency (10 kHz) alternating current at high potentials (20 V<sub>pp</sub>) is required in order to prevent CNTs degradation by electrochemical oxidation and to preserve the porous structure and conductivity at high salinity feed solutions [188]. Therefore, applying 50 W of electrical power resulted in direct heating of the feed solution at the membrane-feed interface and subsequently diminished TP.

In addition, relatively high permeate flux could be gained at low flow velocities even for high saline brines (100 g/L NaCl) as a result of the adequate contact time between the solution and the heating element. In contrast, high flow velocities led to lower permeate flux. For example, a permeate flux of 7 LMH was measured for a low feed flow velocity of 1.5 mm/s with 100 g/L salinity while the permeate flux was around 3.5 kg/m<sup>2</sup>.h at a feed velocity of 6.6 mm/s. In terms of energy consumption, the specific heating energy consumption ( $Q_{sh}$ ) (i.e., the ratio of total heating energy to distillate flow rate) was in the range of other MD processes but relatively high ( $1.25 \pm 0.02$  kWh/kg) [191,192].

In addition to CNTs based Joule heating, a nichrome resistance wire (NRW) incorporated with braid-reinforced PVDF hollow fiber membranes (Figure 2.7d) [193] was used in a Joule based enhanced MD system. The electro-thermal membranes alleviated TP impacts through direct heating of the membrane surface by applying direct current. As hollow fiber structures have a higher surface area than flat sheet membranes, they can provide a more heated surface area. Under air condition, the heating rate of NRW-PVDF membranes was calculated to be around 0.27 °C/s, and they also displayed a good electrothermal ability in the feed saline solution (as shown in IR images of Figure 2.7e), leading to high TPC values of more than a unity (in the range of 1 to 1.05). NRW membranes showed up to 2.5 times higher flux and lower specific energy consumption (SEC) values than the non-electrically heated membranes as a result of increased interfacial temperature and minimized TP. Despite the decreased SEC compared to the non-electrical system under similar operating condition, the specific energy values were not very low, as the SEC at a high current of 0.15 A was obtained around 60 kWh/kg with initial feed temperature of 30 °C and the lowest SEC value was calculated as 11.86 kWh/kg at feed temperature of 70 °C [193].

While at higher feed temperature, SEC value was comparatively lower, it was still high in comparison to reported values for conventional and self-heated MD systems [188,191,192,194].

Overall, membrane heated by Joule heating may be useful at low flow velocities but still suffer from limitations due to high salinity. Furthermore, the required capital cost of the system may be high due to the required modifications and expensive electrodes.

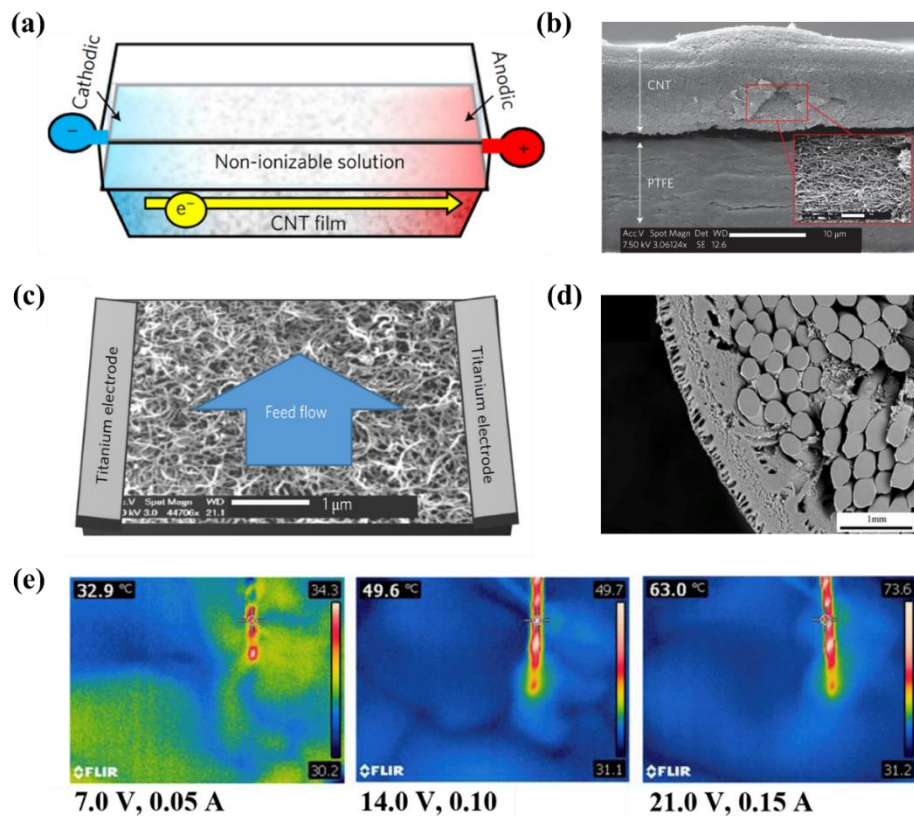


**Figure 2. 7.** (a) Joule heating effect of CNTs layer in a non-ionizable environment (Reprinted from Ref. [188], Copyright (2017), with permission from Springer Nature); (b) Cross-section SEM image of dual-layer hydrophilic/hydrophobic CNTs/PTFE membrane (Reprinted from Ref. [188], Copyright (2017), with permission from Springer Nature); (c) Direct heating of feed solution on the CNTs/PTFE membrane; (Reprinted from Ref. [188], Copyright (2017), with permission from Springer Nature); (d) Cross-section SEM of NRW membrane (Reprinted from Ref. [193], Copyright (2019), with permission from Elsevier); (e) IR image of electro-thermal NRW membrane in the feed solution at different current and initial feed solution of 30 °C (Reprinted from Ref. [193], Copyright (2019), with permission from Elsevier).

## CHAPTER 3

### MATERIALS AND METHODS

**Preface:** The contents of this section are in part based on the following published articles in Journal of Membrane Science and Journal of Separation and Purification Technology:

- I. **Anvari, A.**, Kekre, K. M., Yancheshme, A.A., Yao, Y., Ronen, A., " Membrane distillation of high salinity water by induction heated thermally conducting membranes ", Journal of membrane science 589 (2019): 117253 [194].
- II. **Anvari, A.**, Kekre, K. M., Ronen, A., " Scaling mitigation in radio-frequency induction heated membrane distillation", Journal of membrane science 600 (2019): 117859 [195].
- III. **Anvari, A.**, Yancheshme, A.A., Ronen, A., " Enhanced Performance of Membrane Distillation using Radio-Frequency Induction Heated Thermally Conducting Feed Spacers", Separation and Purification Technology 250 (2020): 117276 [196].

#### 3.1 Materials

Flat sheet hydrophobic PTFE membranes (pore size 0.2  $\mu\text{m}$ , thickness 150  $\mu\text{m}$ , and water entry pressure > 45 psi) were purchased from Sterlitech (Sterlitech Inc. Kent, WA). Multi-wall carbon nanotubes functionalized with Carboxylic groups via Plasma treatment (CNTs-COOH) (outer diameter (30 to 50 nm), length (10-20 $\mu\text{m}$ ), and purity >95 %) were purchased from CheapTubes (CheapTubes Inc., Brattleboro, VT). Polyvinyl alcohol (PVA) (MW 146-168 kDa), 50 wt% Glutaraldehyde solution, Hydrochloric acid (HCl) 37%, Iron (III) chloride hexahydrate ( $\text{FeCl}_3$ ), Iron (II) sulfate heptahydrate ( $\text{FeSO}_4$ ), Sodium chloride (NaCl), Sodium hydroxide (NaOH), Calcium sulfate ( $\text{CaSO}_4$ ) were

purchased from Sigma Aldrich (t. Louis, MO). Potassium chloride (KCl) was purchased from MP Biomedicals LLC (Solon, Ohio). Magnesium chloride (MgCl) and Magnesium sulfate (MgSO<sub>4</sub>) were purchased from LabChem (Zelienople, PA 16063).

Four commercial stainless-steel 316 meshes (McMaster Carr) (Figure 3.1) were evaluated as feed spacers, spacers had a thermal conductivity of  $13 \frac{W}{m.K}$ . While corrosion was not observed on the SS 316 spacer during our experiments and is not expected to be an issue under standard operating conditions, highly corrosive feed solutions may require using spacers made from corrosion resistant alloys such as SS 904L, Super Duplex alloys [197,198] or other metal alloys (e.g., titanium alloys [198]) with high corrosion resistance and induction heating capability. A non-conductive commercial polypropylene (PP) spacer (SWM, GA) was used for comparison.

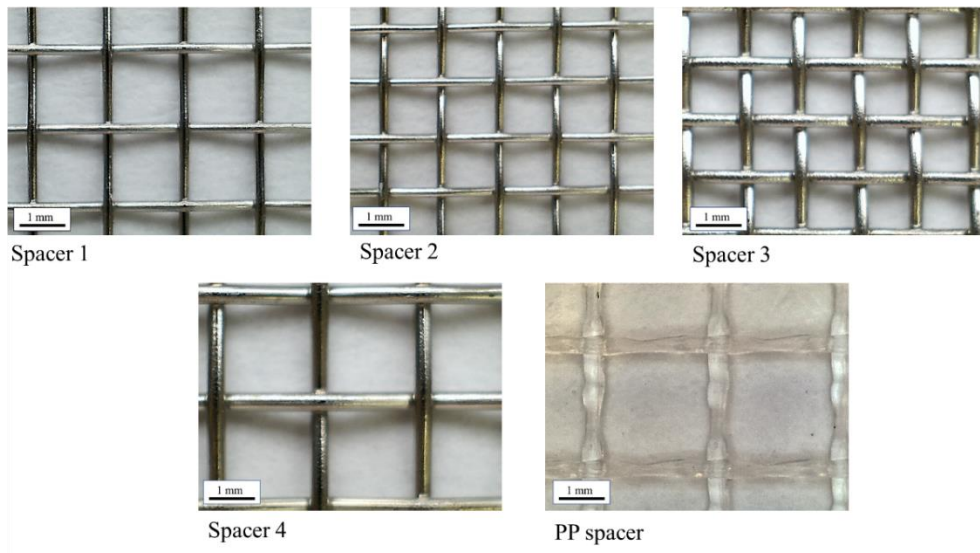


**Figure 3. 1.** Images of the SS and PP feed spacers.

### 3.2 Feed Solutions

For the MD experiments without considering scaling, 35 g/L NaCl brine solution, representing seawater was used. In addition to this solution, two other brine solutions as

10 g/L NaCl solution (saline water) and 100 g/L NaCl solution (RO concentrated brine) were tested to assess concentration impact.

Furthermore, for scaling assessments, deionized (DI) water and a NaCl brine solution (35 g/L NaCl) with different concentrations of CaSO<sub>4</sub> (0, 1.8, 2.7, and 3.6 g/L) were used as the feed solutions in all experiments. In addition, the simulated RO brine included 35 g/L NaCl, 1.80 g/L CaSO<sub>4</sub>, 2.91 g/L MgSO<sub>4</sub>, 4.52 g/L MgCl<sub>2</sub>, and 1.03 g/L KCl [54].

The saturation index (SI) of solutions was calculated based on eq. 3.1 [199]. Solutions with SI = 0 are at equilibrium while the solutions with SI < 0 and SI > 0 are undersaturated and supersaturated, respectively.

$$SI = \log \left( \frac{s}{s^0} \right) \quad \text{Eq. 3.1}$$

Where  $s$  is the solubility of CaSO<sub>4</sub> at  $I$  (i.e., ionic strength),  $s^0$  is the solubility at  $I=0$  (i.e. solubility product). As  $I$  is equal to the molality of (NaCl + 4×molality of CaSO<sub>4</sub>),  $s$  is the solubility of CaSO<sub>4</sub> at any particular concentration.

### **3.3 Synthesis of Iron Oxide Coated Multiwall Carbon Nanotubes (Fe-CNTs)**

Iron oxide coated multiwall carbon nanotubes were prepared as described by Ntim et al. (2011), [200]. Briefly, CNTs were dispersed in an aqueous solution of FeCl<sub>3</sub>: FeSO<sub>4</sub> (2:1) using a horn sonicator (Fisher Scientific FB705). 5M NaOH solution was added to the dispersion, to reach a pH of 10. The solution was stirred moderately at 70 °C for 5 min and vigorously stirred at 85 °C for 1 h. The modified MWCNTs, coated with iron oxide, were washed and acidified to pH 5 with 1 M hydrochloric acid.

### **3.4 Fabrication of Fe-CNTs/PTFE Membrane**

Membrane fabrication was according to previous studies using CNTs and PVA [188,190,201]. The CNTs were linked together with a matrix provided by PVA through

covalent bonding of carboxyl groups of the CNT-COOH and hydroxyl groups of PVA. The prepared Fe-CNTs powder ( $2.3 \text{ mg/cm}^2$ ) dispersed in the DI water and  $0.46 \text{ mL/cm}^2$  of 1 wt.% PVA solution were sprayed layer by layer on a PTFE membrane. Spray coating was done using an in-house built spray coater including an airbrush (Master Dual-Action Siphon Feed Airbrush, Model S68) which was attached to XY plotter. As the membrane is hydrophobic, the heating/drying process was done using a heat gun (TCKLIFE, HGP73AC) to immediately dry each sprayed layer. Then, the Fe-CNTs sprayed layer was stabilized by a crosslinking solution (1.1 vol% Glutaraldehyde and 0.55 vol% hydrochloric acid) and heated at  $90 \text{ }^\circ\text{C}$  for 1 h. The prepared membrane was dried and kept at room temperature.

### **3.5 Surface Characterization**

Membranes' surface and cross-sections were characterized by scanning electron microscopy (SEM, FEI Quanta 450FEG SEM). The iron-coated carbon nanotubes morphologies were imaged by transmission electron microscopy (TEM, FEI Quanta 450FEG). Fourier-transform infrared spectroscopy (FTIR, Perkin-Elmer Spectrum 100) and energy dispersion of X-ray (EDX, FEI Quanta 450FEG) were used in order to detect the formation of the Fe-O bonds and scaling on the membrane surface along with the percentage of iron oxide coated on the Fe-CNTs membrane surface, respectively. A goniometer (Ossila Limited L2004A1) was used to assess membrane hydrophilicity (i.e., contact angle) using deionized (DI) water.

### **3.6 Experimental Design**

#### **3.6.1 Vacuum Membrane Distillation (VMD) system with RF heated membrane**

The radio-frequency induction heated-vacuum membrane distillation (RF-VMD) (see system diagram in Figure 3.2) contains three main components, a membrane module, an induction heating system, and a vacuum distillate collector. The membrane module was fabricated by CNC machine using a Nylon sheet (McMaster Carr) and can hold a flat sheet membrane with an effective area of 32 cm<sup>2</sup>. The membrane module including Fe-CNTs/PTFE membrane, was placed on the heating coil of an IH system (UltraFlex SH-2 with power ranging from 60-2000 W and frequency of 283 kHz). Feed solution at RT (20 °C) was continuously fed (velocities varied between 1.05 to 11.25 cm/min) to the membrane module using a peristaltic pump (Masterflex 77201-60). In order to keep the temperature and feed concentration constant, the concentrate stream was not recycled back into the feed tank following MD but was used as a single pass system (except in concentration factor experiments (section 4.2.6)). In all experiments, the feed solution's temperature was continuously monitored and controlled using a cooling bath. For section 4.2.6 experiments (concentration factor experiments), temperature was kept constant while the salt concentration increased as the concentrate stream was recycled back into the feed tank following MD, thus increasing the ions concentrations in the feed. In addition, the feed solutions were continuously mixed using magnetic stirrer to prevent the precipitation of CaSO<sub>4</sub> in the feed solution. Distillate was collected using a vacuum pump and condenser. Vacuum level varied between 20 and 70 kPa. The salinity of condensed and concentrated solutions was continuously monitored by using electrical conductivity (EC, Thermo scientific- Orion Star A329).

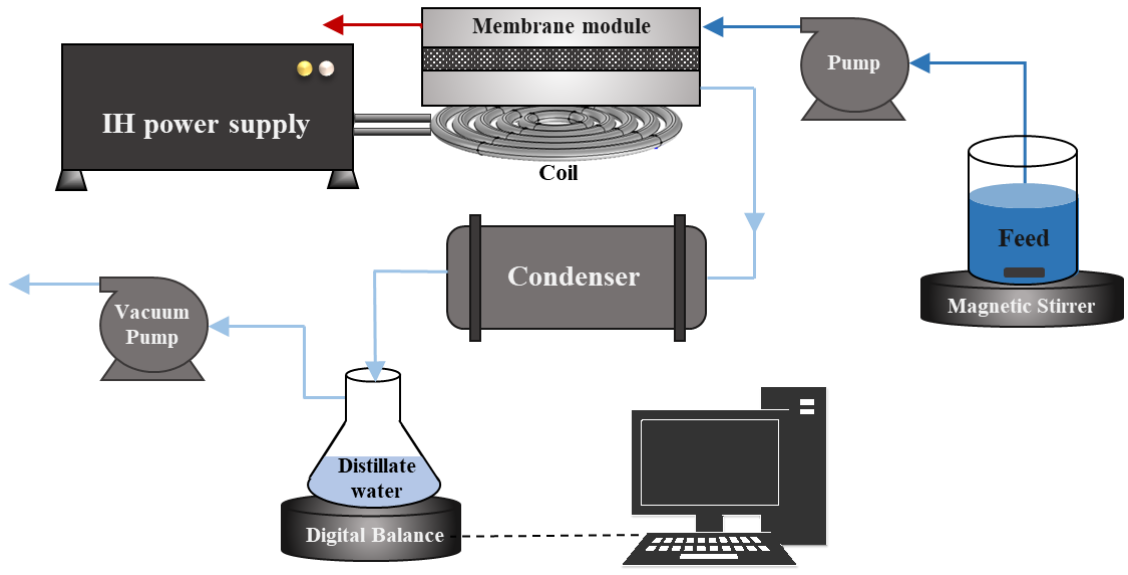


**Figure 3. 2.** Schematic diagram of the RF-VMD system.

### 3.6.2 Vacuum Membrane Distillation (VMD) system with RF heated spacer

For this part of experiments, the membrane module in the RF-VMD setup (Figure 3.2), contains pristine PTFE membrane instead of a dual layer Fe-CNTs/PTFE membrane and is modified with SS feed spacers (Figure 3.3a). Feed solution (35g/L sodium chloride in deionized water) at room temperature was continuously fed to the membrane module with varying velocities (28.5-300 cm/min). The distillate was collected using a condenser and a vacuum pump operating at varying vacuum levels (10-30 kPa). Furthermore, during our experiments, no changes in membrane structure were detected and the PTFE membranes were reused with no change in their selectivity and transport properties.

The impact of four SS spacers was evaluated according to their varying mass, filament distances (i.e., H), porosity (i.e., opening size), and diameter (D). In addition, the spacers were evaluated at orientations ( $\alpha$ ) of  $45^\circ$  and  $90^\circ$  (Figure 3.3b, Table 4.4 of section 4.3.5) and compared to PP spacer with similar H, D, and porosity as the S4 spacer. As all the SS

spacers were purchased as commercial products, it was difficult to decouple the mass and structure of the spacers. Therefore, the spacers were evaluated in two groups (S1 and S2 vs. S3 and S4) with relatively similar mass, while the distance between filaments (H) and porosity were varied per each group (Table 4.4 of section 4.3.5). All spacers were placed horizontally and adjacent to the PTFE membrane (Figure 3.3a).

Initially, all parametric assessments were done using an S1 type spacer (Section 4.3.4), having the following physical properties: a mass of 1.5 gr per assessed spacer area, H of 1.45 mm, and a porosity of 73%. Following evaluating the impact of flow velocity, applied power, and vacuum level on distillate flux, the additional SS spacers were assessed and rated based on the highest distillation values obtained (section 4.3.5).

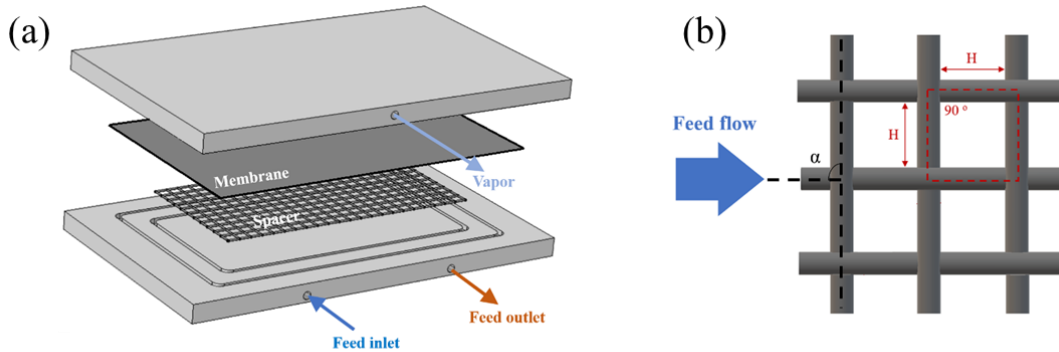


**Figure 3. 3.** Schematic diagram of the (a) Membrane module; (b) Spacer’s parameters.

### 3.7 MD Performance

The performance of the MD process was assessed based on distillate flux ( $\text{kg}/\text{m}^2\cdot\text{h}$ ), according to Eq. 3.2.

$$J = \frac{M}{A \cdot \Delta t} \quad \text{Eq. 3.2}$$

Where  $M$  is the mass of collected condensate (kg),  $A$  is the active membrane area ( $32 \text{ cm}^2$ ), and  $\Delta t$  is the operational time (h).

Feed and distillate salinity were continuously monitored and salt rejection was calculated using Eq. 3.3:

$$\text{Rejection (\%)} = \left(1 - \frac{C_p}{C_f}\right) \times 100 \quad \text{Eq. 3.3}$$

Where  $C_p$  and  $C_f$  are salt concentration or electrical conductivity of the permeate and feed solutions, respectively.

For scaling analyses, the normalized flux (N.F) was measured based on the ratio of distillate flux to the initial distillate flux of DI water ( $J/J_o$ ) and presented as a measure of  $\text{CaSO}_4$  scaling. Each experiment was replicated at least three times and error bars represent the standard deviation. In addition, results were analyzed to determine statistical significance ( $p < 0.01$ ). In addition,  $\text{CaSO}_4$  crystals' number in the concentrate solutions was measured by imaging a 1 mL of solution using a microscope (Zeiss Axio Examiner Z1) and analyzing the images by image processing software (ImageJ).

### **3.8 Thermal Imaging and Temperature Profiles**

Temperature profiles of the SS spacers and feed solutions were measured at static and flow conditions using a digital IR thermal imaging camera (FLIR T440) equipped with a FLIR Lepton IR sensor. The SS spacers were placed in the open module and exposed to the RF magnetic field at static and flow conditions. Images were taken at initial conditions and following several seconds of RF heating. In addition to the IR surface imaging, surface and cross-section temperature profiles of RF heated spacers and feed solutions were numerically predicted using a commercial finite-element package (COMSOL Multiphysics v5.5) (Section 3.13).

### 3.9 Temperature Polarization Coefficient (TPC)

The temperature polarization coefficient (TPC) was calculated and used to quantify the degree of heat transfer resistances due to the TP versus the total heat transfer resistance [80]. In VMD systems, TP is mainly considered to be a result of the thermal boundary layer of the feed side [202], therefore, TPC was calculated according to Eq. 3.4:

$$\text{TPC} = \frac{\bar{T}_{\text{fm}}}{\bar{T}_f} \quad \text{Eq. 3.4}$$

Where  $\bar{T}_{\text{fm}}$  and  $\bar{T}_f$  are the average temperature of the feed at the membrane interface and the average temperature of bulk feed solution, respectively. These values were calculated using numerical simulation (Section 3.13). High TPC values (unity or higher) express lower TP while low TPC values (converging to zero) express notable TP [60].

### 3.10 Workpiece Power ( $P_w$ )

For RF heating, the power consumed by the system (i.e., the IH system) is constant for a specific coil and is not influenced by the volume or mass of the workpiece (i.e., the heated element or spacer). Therefore, for a constant supplied power (e.g., 60-90W in this work), multiple layers of SS spacers or multiple VMD modules can be heated, thus, increasing the overall distillate flux and decreasing the specific heating energy accordingly. The connection between the power consumed by the system ( $P_c$ ) and the power at the workpiece ( $P_w$ ) which is further transported to the feed solution [203] can be calculated according to Eq. 3.5:

$$P_c = \frac{P_w}{\eta_{\text{el}}\eta_{\text{th}}} \quad \text{Eq. 3.5}$$

Where  $\eta_{\text{el}}$  is electrical efficiency and  $\eta_{\text{th}}$  is thermal efficiency, which are in the range of 0 to 1 and vary by coil and workpiece properties (e.g., effective coil diameter, current

penetration depths in the coil and workpiece, electrical resistivities of the coil and workpiece, relative magnetic permeability of the workpiece, etc.).

The power consumption of the heated element, i.e., the SS spacer, was estimated according to Eq. 3.6, based on the required power to heat a given mass of workpiece to a final temperature [203]:

$$P_w = mc \frac{T_{fs} - T_{is}}{t} \quad \text{Eq. 3.6}$$

where  $m$  is the mass of the heated workpiece (g),  $c$  is the specific heat (J/g °C),  $T_{fs}$  and  $T_{is}$  are final and initial average temperatures of the spacer (°C), and  $t$  is the heating duration (s).

### 3.11 Temperature and Heating Rate Calculations of RF Heated Spacers

The heating rate of SS spacer was calculated based on the temperature difference over a duration of time according to the:  $\frac{T_{fs} - T_{is}}{t}$ , where  $T_{fs}$  and  $T_{is}$  are final and initial average temperatures (°C), and  $t$  is heat time (s) [203]. The average final temperatures of SS spacer over a duration of 5 seconds were measured using digital IR thermal imaging (Figure 3.4), while keeping the initial temperatures at 20-23°C.

In IH system, the eddy currents are not uniformly distributed [203,204] and the RF heating is non-uniform along the spacer, leading to an uneven temperature distribution [204] (See Figure 3.4 as an example). Therefore, the IR image of spacer was divided into three regions (top and bottom, both sides, and center) and 5 sections to calculate the average spacer's temperatures. The average temperature was calculated according to the overall weighted area of each temperature using a graphical analysis software (ImageJ). In addition, the heating rate of the SS spacer was calculated based on the temperature difference over a duration of time (i.e., five seconds). All measurements were done in triplicates for the SS

spacer at a coil power of 60W to 90 W and then the final temperatures and heating rates were averaged accordingly.

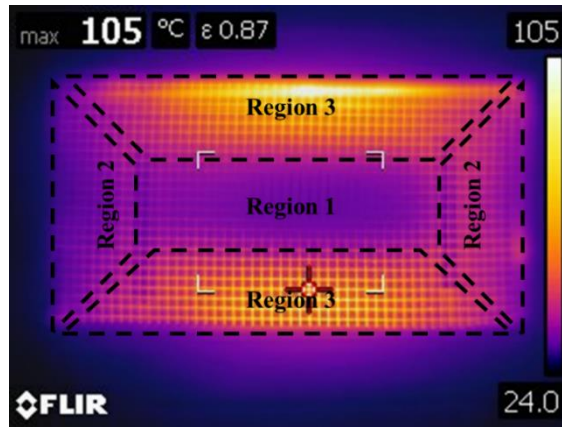


**Figure 3. 4.** IR thermal image of the S1 spacer after 5 seconds of induction heating.

### 3.12 Heating Energy Calculations

The specific energy used to heat the feed solution was calculated according to the energy required to provide a transmembrane temperature gradient divided by a unit volume of distillate water [166] according to Eq. 3.7:

$$Q_s \left( \frac{\text{kWh}}{\text{L}} \right) = \frac{\text{Heating energy [kW]}}{\text{Volume of distillate water per time [L/h]}} \quad \text{Eq. 3.7}$$

Where  $Q_s$  is the specific heating energy. For RF heated systems, the heating energy can be calculated using Eq. 3.6. In addition, the gain output ratio (GOR) was calculated to analyze the efficiency of the RF heating energy. GOR is defined as the ratio of energy required for water evaporation to the net added energy according to Eq. 3.8 [188].

$$\text{GOR} = \frac{J \times h_v}{Q_{in}} \quad \text{Eq. 3.8}$$

Where  $h_v$  is water evaporation enthalpy and  $Q_{in}$  is the net input thermal energy, which is based on  $\text{kW/m}^2$  consumed energy.

### 3.13 Numerical Modeling and Simulation

#### 3.13.1 VMD process with RF heated membrane

A comprehensive numerical approach was applied in order to describe water transport through a hydrophobic flat-sheet PTFE membrane used in the RF-VMD system. Three-coupled transport equations (i.e., momentum, mass and energy (eq. 3.9-3.12)) were numerically solved using FEM (Finite Element Method) to describe the temperature and flux gradients near and through the membrane. All simulations were performed in a 2D framework with the aid of COMSOL Multiphysics v5.5.

Momentum transport equation:

$$\rho(\mathbf{u} \cdot \nabla)\mathbf{u} = -\nabla p + \mu \nabla^2 \mathbf{u} \quad \text{Eq. 3.9}$$

Continuity equation:

$$\nabla \cdot \mathbf{u} = 0 \quad \text{Eq. 3.10}$$

Heat transport equation:

$$\rho c_p \mathbf{u} \nabla T = K \nabla^2 T \quad \text{Eq. 3.11}$$

Mass transport equation:

$$\mathbf{u} \nabla C_i = D_i \nabla^2 C_i \quad \text{Eq. 3.12}$$

Where  $\rho$  is the density ( $\text{kg/m}^3$ ),  $P$  is pressure (Pa),  $\mathbf{u}$  is the 2D velocity vector (m/s),  $\mu$  is viscosity (Pa. s),  $c_p$  is the specific heat capacity at constant pressure,  $K$  is the thermal conductivity (W/m. K),  $T$  is the temperature (K),  $D$  is diffusion coefficient ( $\text{m}^2/\text{s}$ ), and  $C$  is molar concentration ( $\text{mol/m}^3$ ).

The model was developed based on the following assumptions: steady-state condition, no water transport through the membrane pores, i.e. full hydrophobicity of membrane, 100%

rejection of salt, laminar flow for two phases in all contactors, negligible heat loss to the environment, and no-slip condition at the surface of membrane. Operating and initial conditions are similar to our experimental system (Table 3.1).

**Table 3. 1.** Operating and initial parameters

<b>Parameter</b>	<b>value</b>
<b>Membrane length</b>	80 mm
<b>Height flow channel</b>	1 mm
<b>Membrane pore size</b>	0.2 $\mu\text{m}$
<b>Membrane thickness</b>	150 $\mu\text{m}$
<b>Vacuum pressure</b>	20 kPa
<b>Feed flow velocity</b>	2.33cm/min
<b>Feed concentration</b>	35 g/L
<b>Inlet temperature</b>	20 $^{\circ}\text{C}$

The transport equations including momentum transport in the feed, membrane and the permeate channel, mass transport for salt in the feed and vapor in the membrane pores, energy convection and conduction for all three layers of contactor (Figure 3.5), with the appropriate boundary conditions (Table 3.2), were considered according to Hayer et al. [205]. In all simulations, the membrane and the Fe-CNTs layer were considered as a uniform domain with a boundary heat source at the membrane-water interface. This is done to simplify the numerical model as the thickness of the coated layer (30  $\mu\text{m}$ ) responsible for heat generation, is small in comparison to the membrane module.

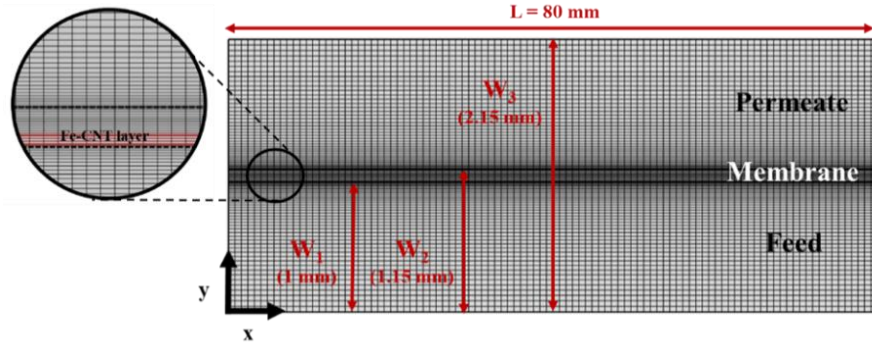


**Figure 3. 5.** Computational domain and mesh grid including three distinct regions; feed (saline water stream), membrane, and permeate (pure water vapor).

**Table 3. 2.** Adopted boundary conditions (BCs) in computational model.

Feed Side						
Position	Momentum transfer		Mass transfer		Heat transfer	
$x = 0$	$u = u_{inlet}$	Velocity	$C_i = C_{inlet}$	Concentration	$T = T_{inlet}$	Temperature
$x = L$	$p = p_{atm}$	Pressure	$D_i \nabla C_i = 0$	Outflow	$K \nabla T = 0$	Outflow
$y = 0$	$u = 0$	Wall	$N_i = 0$	Mass Flux	$q = 0$	Insulation
$y = w_1$	Eq. 3.13	Velocity	$N_i = 0$	Mass Flux	$T = T_{membrane}$	Temperature
Membrane Side						
Position	Momentum transfer		Mass transfer		Heat transfer	
$x = 0$	$u = 0$	Wall	$N_i = 0$	Mass Flux	$q = 0$	Insulation
$x = L$	$u = 0$	Wall	$N_i = 0$	Mass Flux	$q = 0$	Insulation
$y = w_1$	$p = p^v$	Pressure	$p^v / RT$	Concentration	$Q = 781.25 \text{ W/m}^2$	Heat source
$y = w_2$	$p = p_{permeate}$	Pressure	$p_{permeate} / RT$	Concentration	$T = T_{permeate}$	Temperature
Permeate Side						
Position	Momentum transfer		Mass transfer		Heat transfer	
$x = 0$	$p = p_{vacuum}$	Pressure	-	-	$K \nabla T = 0$	Outflow
$x = L$	$u = 0$	Wall	-	-	$q = 0$	Insulation
$y = w_2$	Eq. 3.14	Velocity	-	-	$T = T_{membrane}$	Temperature
$y = w_3$	$u = 0$	Wall	-	-	$q = 0$	Insulation

Outlet velocity from feed side to the membrane and inlet velocity from membrane to the permeate side are calculated, respectively, as follow (Eq. 3.13 and 3.14) [37]:

$$u = \frac{(\partial C_{\text{membrane}} / \partial y) D_{\text{eff}} M_w}{\rho_w} - u_{\text{membrane}} \frac{\rho_v}{\rho_w} \quad \text{Eq. 3.13}$$

$$u = \frac{(\partial C_{\text{membrane}} / \partial y) D_{\text{eff}} M_w}{\rho_v} - u_{\text{membrane}} \quad \text{Eq. 3.14}$$

Where  $M_w$  (kg/mol),  $\rho_w$  and  $\rho_v$  (kg/m<sup>3</sup>) are water molecular weight, density of water and vapor, respectively. Moreover,  $D_{\text{eff}}$  is the effective diffusion coefficient of water vapor into membrane. Effective diffusivity can be estimated using both Fick's diffusion ( $D_v$ ) and Knudsen diffusion ( $D_{\text{knd}}$ ) mechanisms (Eq. 3.15- 3.17) [37]:

$$1/D_{\text{eff}} = 1/D_v + 1/D_{\text{knd}} \quad \text{Eq. 3.15}$$

$$D_v = \varepsilon \mu_v / \tau \rho_v \quad \text{Eq. 3.16}$$

$$D_{\text{knd}} = \frac{2\varepsilon}{3\tau} d_p \sqrt{\frac{2RT}{\pi M_w}} \quad \text{Eq. 3.17}$$

Where  $D_v$  (m<sup>2</sup>/s) is the effective Fick's diffusion coefficient,  $\varepsilon$ ,  $\tau$ , and  $\mu_v$  (Pa.s) are membrane porosity, tortuosity, and water vapor viscosity, in turn. Also,  $d_p$  (m) and  $R$  (J/mol. K) are membrane pore diameter and universal gas constant.

In addition, as COMSOL has no simple built-in induction heating process, we developed the model by applying a constant heat flux on the feed-membrane interface as IH based Fe-CNTs layer produced and conducted heat to the water. The rate of heat production ( $Q$ ) was calculated based on the obtained average temperature changes of the feed solution. Simulation results were compared to the experimental results.

### 3.13.2 VMD process with RF heated spacer

Heating the thermally conductive spacers and temperature profiles of the feed solution were numerically simulated using Finite Element Method with the aid of COMSOL. The numerical simulations were done in static and flow conditions:

#### 3.13.2.1 Thermally Conducting Spacers in Static Conditions

In order to verify the heating of the SS spacers, we used a 3D model configuration which included the following elements: flat spiral induction copper coil, SS spacers (i.e., S1 and S4), and stagnant air in between (Figure 3.6).

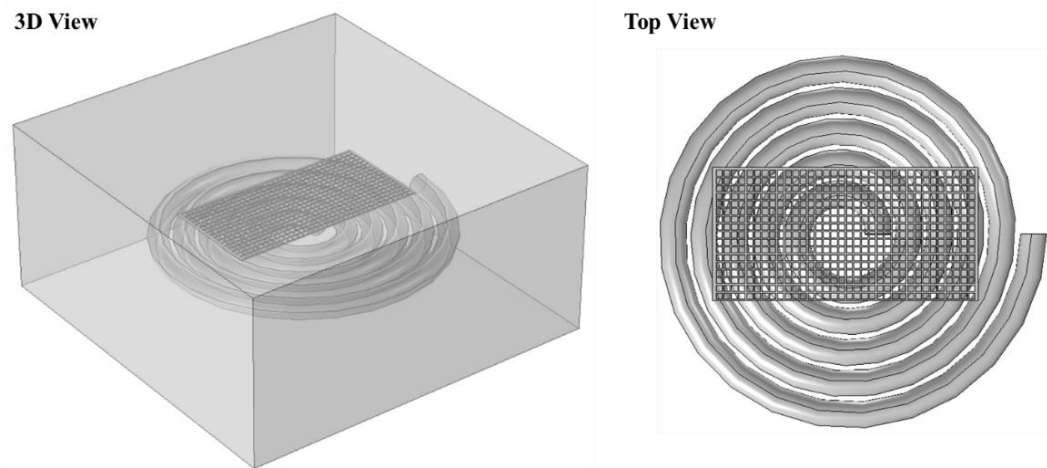


**Figure 3. 6.** Configuration of coil, spacer, and air domains used for 3D numerical simulations-static condition.

Calculating the heat produced in the workpiece required solving both heat transfer and magnetic field propagation simultaneously. The model was solved with a transient approach incorporating the following governing equations (Equations 3.18-3.24)[206]:

Energy balance:

$$\rho_s C_{p,s} \frac{\partial T}{\partial t} - \nabla \cdot k_s \nabla T = Q_e \quad \text{Eq. 3.18}$$

Where  $\rho_s$  is the density,  $C_{p,s}$  is the specific heat capacity,  $k_s$  is the thermal conductivity of workpiece, and  $Q_e$  represents the heat source which comes from the electromagnetic losses. The RF heating results in eddy currents into the workpiece (i.e., metallic spacer) that produce heat due to resistivity of workpiece (i.e., Joule effect). Thus, the heat source term in Eq. 3.18 ( $Q_e$ ) is mainly attributed to resistive losses and calculated by Eq. 3.19.

$$Q_e = \frac{|J'|^2}{2\sigma} \quad \text{Eq. 3.19}$$

Where  $\sigma$  and  $J'$  represent the electrical conductivity of the material and conduction current density, respectively. The electromagnetic field in the induction heating is calculated by Maxwell-Ampere's law (Eq. 3.20):

$$\nabla \times H' = J' + j\omega D' \quad \text{Eq. 3.20}$$

Where  $H'$  is the magnetic field intensity, and  $D'$  is the electric flux density. The constitutive relation to the magnetic flux density is given as (Eq. 3.21-3.24):

$$B = \mu' H' \quad \text{Eq. 3.21}$$

$$B = \nabla \times A' \quad \text{Eq. 3.22}$$

$$E = -j\omega A' \quad \text{Eq. 3.23}$$

$$J' = \sigma E \quad \text{Eq. 3.24}$$

where  $B$ ,  $\mu'$ ,  $A'$ , and  $E$  are magnetic flux density, magnetic permeability, magnetic potential, and electric field intensity, respectively [206].

Numerical simulations were validated with the experimental results by comparing the temperature distribution and obtained average surface temperature of the spacers.

### 3.13.2.2 Thermally Conducting Spacers in Flow Conditions

A similar model was incorporated to simulate the temperature profile of the solution in contact with the RF heated spacers. Three additional partial differential equations (PDEs)

were solved including momentum balance (addressing the liquid flow), energy balance (convection heat transfer from the spacer to the solution), and the continuity equation (Equations 3.9-3.11).

Numerical simulations with flow condition have been done in two steps; first we considered flow conditions without MD related process (i.e., Section 4.3.3), aiming to evaluate the heating process in flow condition and the heat transfer from the spacer to the feed solution, all preceding equations were solved in 3D domain with steady-state conditions. All simulations were done for a cold feed (23 °C) with a solution containing 35 g/L of NaCl. Vacuum level, latent heat, and water conductive heat transfer were not used at this stage as the purpose was to describe the temperature distribution along the feed channel following exposure to the heated spacers.

In the next step, feed channel temperature distribution and TPC values of the MD process (Section 4.3.6) were calculated by incorporating continuity, momentum, and convective heat transfer (Eq. 3.9-3.11) in the feed domain. As 3D simulation is time-intensive and requires a high computational load, we considered only the feed domain and added an additional boundary condition, i.e., the outward heat flux from the top face of the feed is equivalent to the latent heat of evaporated stream in MD process. This was incorporated to include the impact of water evaporation (Boundary heat flux =  $J_{\text{exp}} \cdot h_v$ ). Model geometry and corresponding boundary conditions are shown in Figure 3.7 and Table 3.3, respectively.

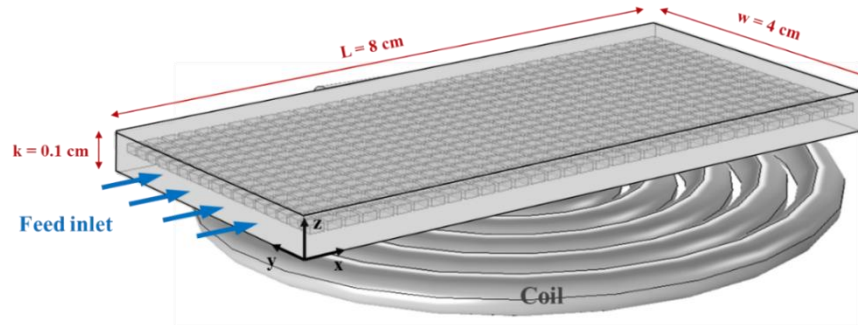


**Figure 3. 7.** Configuration of coil, spacer, and feed solution domains used for 3D numerical simulations – Flow condition

**Table 3. 3.** Adopted boundary conditions (BCs) in computational model.

Feed Side					
Momentum Transfer			Heat Transfer		
@ x = 0	$u = u_{in}$	Velocity	@ x = 0	$T = T_{in}$	Temperature
@ x = L	$p = p_{atm}$	Pressure	@ x = L	$KVT = 0$	Outflow
@ y = 0	$u = 0$	Wall	@ y = 0	$q = 0$	Insulation
@ y = w	$u = 0$	Wall	@ y = w	$q = 0$	Insulation
@ z = 0	$u = 0$	Wall	@ z = 0	$q = 0$	Insulation
@ z = k	$u = 0$	Wall	@ z = k	$J_{exp} \cdot h_V$	Heat flux

In order to validate our simulation results for the flow condition, we compared the predicted outlet flow temperature (average T at x=L, Figure 3.7) by simulation and corresponding values from our experiments for the case of S4 spacer. Table 3.4 compares the results of simulation and experimental values for two different flow velocities with relative errors of less than 6%. Then, simulated  $\bar{T}_{fm}$  values were used to evaluate TPC values along the membrane length.

**Table 3. 4.** Validation data for flow condition simulations.

Spacer S4			
Inlet feed velocity (cm/min)	Feed outlet T (°C)		Relative error %
	Experimental	Simulation	
100	43.5	40.97	5.8
300	31	30.14	2

## CHAPTER 4

### RESULTS AND DISCUSSIONS

#### 4.1 Membrane Distillation of High Salinity Water by Induction Heated Thermally Conducting Membranes

**Preface:** The contents of this section are in part based on a published article in Journal of Membrane Science: **Anvari, A.**, Kekre, K. M., Yancheshme, A.A., Yao, Y., Ronen, A., " Membrane distillation of high salinity water by induction heated thermally conducting membranes ", Journal of membrane science 589 (2019): 117253 [194].

##### 4.1.1 Introduction

The goal of this section is to develop and optimize a novel, efficient and robust VMD system utilizing induction heating (IH) as a heat source to the distillation process. To enhance membrane heating, we used a composite dual layer membrane. The top membrane layer contained hydrophilic magnetic iron oxide nanoparticles (FeNPs) coated on carbon nanotubes (CNTs) and the lower layer was a commercial hydrophobic polytetrafluoroethylene (PTFE) membrane. Ferromagnetic particles such as FeNPs are ideal for IH applications as they have high ferromagnetic properties and saturation magnetization [207,208]. As RF-IH can heat conductive and magnetic surfaces rapidly, efficiently, and contactless [209], it can be used to directly heat the surface of the composite membrane. IH transfers energy directly to the metallic element (i.e., workpiece) with minimal heat loss to the surrounding environment, leading to significant power savings. The efficiency of delivered power vs. transferred heat to the element was shown to be higher than 90% when heating systems based on electric-radiant and gas were about 55% and 50 %, respectively [209–212]. To efficiently heat nanoparticles by IH, a high frequency

in the range of kHz is required [213]. An illustration of the RF-VMD process with a composite dual layer membrane is presented in Figure 4.1.

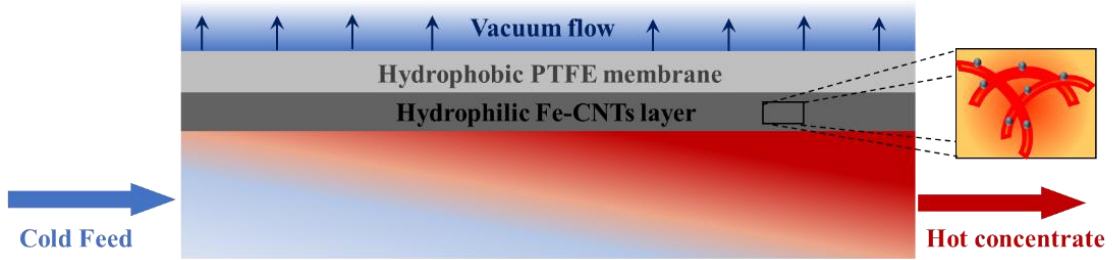


**Figure 4. 1.** Illustration of the RF-VMD process. Bottom layer: temperature profile in the feed; Middle layer: composite membrane; Top: vacuum chamber. Right image: enlargement of the Fe-CNTs layer.

#### 4.1.2 Characterization of Fe-CNTs Powder

Following synthesis, Fe-CNTs powder was imaged by SEM and TEM to detect the nanoparticles' presence on the CNTs and quantified by EDX and FTIR to determine the FeNPs' concentration and structure. Due to their nature, FeNPs heat rapidly and to elevated temperature in comparison to CNTs as a result of magnetic hysteresis. Therefore, to allow homogenous heat transport throughout the membrane surface by conduction, it is required that FeNPs are in direct contact with the CNTs. Comparison of SEM images of untreated CNTs and the synthesized Fe-CNTs powder (Figure 4.2 a, b) shows that the CNTs are coated by iron oxide nanoparticles. TEM micrographs of Fe-CNTs powder (Figure 4.2c) show the presence of iron oxide nanoparticles on the CNTs, as single particles or in clusters, with a typical diameter of 10-20 nm. Furthermore, the electrical resistance of the powder did not decrease following the FeNPs modifications, and the CNTs seem undamaged with a relatively uniform diameter, which confirms their stability. EDX data (Figure 4.2d) indicates the presence of a relatively high load, about 45 % Wt. of iron on the surface of CNTs. These results are in agreement with previous data by Ntim et al. where

CNTs were coated by 40 Wt. % of iron [200]. IR spectrum confirms the presence of iron in the Fe-CNTs powder at 525 and 545  $\text{cm}^{-1}$  (Figure 4.2e) which are typical for Fe—O bonds of iron oxide [200].

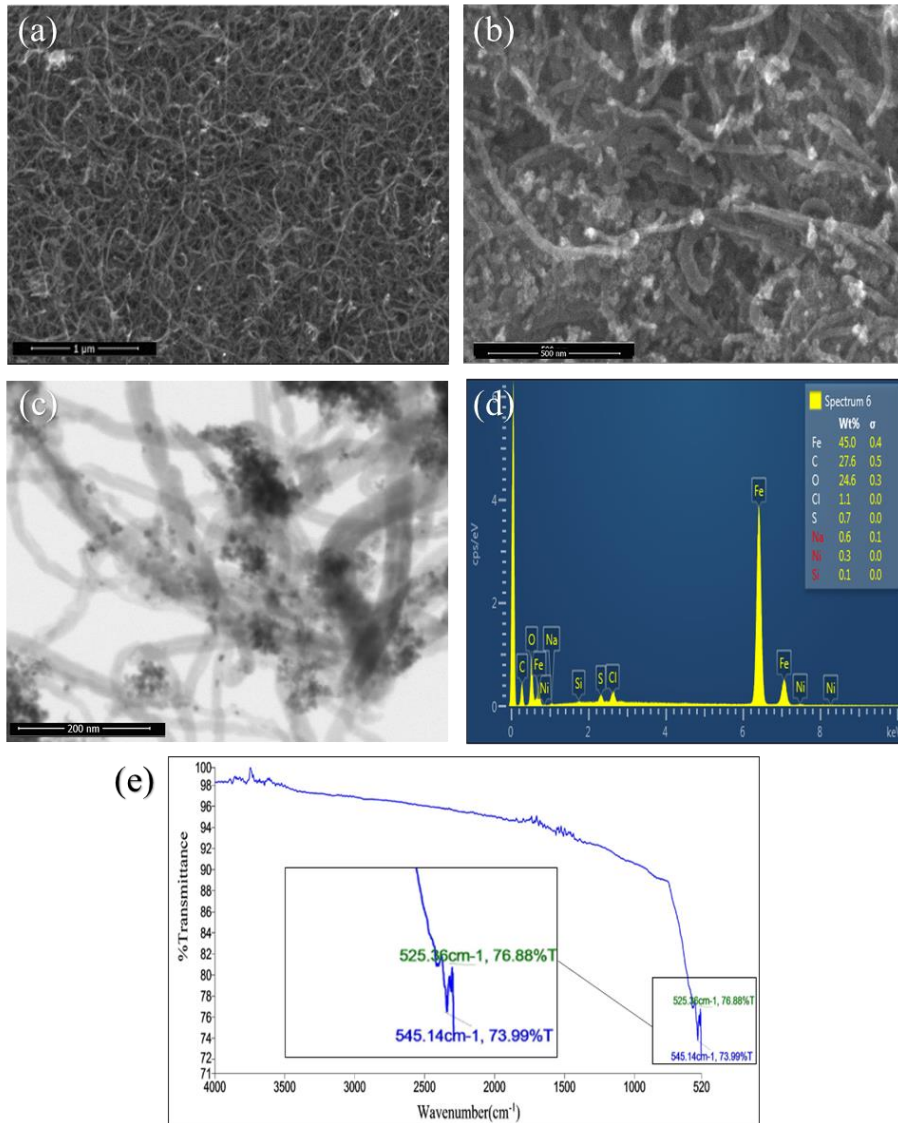


**Figure 4. 2.** Characterization of the synthesized Fe-CNTs powder: (a) SEM image of CNTs; (b) SEM image of Fe-CNTs; (c) TEM image of Fe-CNTs; (d) EDX analysis of Fe-CNTs film; (e) FTIR analysis of Fe-CNTs.

### 4.1.3 Fe-CNTs Coating Characterization

IH efficiency is influenced by the membrane's conductivity and the mass loading of Fe-CNTs. Therefore, controlling membrane properties, i.e. thickness and Fe-CNTs mass loading are critical parameters which can impact the distillate flux. As we deposit the Fe-CNTs layer on the PTFE support membrane by a spray coating process, the layer's thickness can be controlled through spray duration and the number of sprayed layers. Figure 4.3a shows an example of a coating layer with an average thickness of  $30\pm 2\mu\text{m}$ . In addition to the layer's impact on IH performance, which is discussed in section 4.1.5.3, the Fe-CNTs coating decreases the membrane contact angle, i.e. increase hydrophilicity (Figure 4.3 b, c). While the PTFE membrane is hydrophobic with a water contact angle (WCA) of  $128\pm 1.8^\circ$ , the WCA of the coated Fe-CNTs/PTFE membrane decreased significantly to  $19.5\pm 1.5^\circ$ . The change in surface properties is mainly due to the use of carboxylated CNTs and PVA as a cross-linker. The hydrophilicity of Fe-CNTs layer increases the overall distillate flux by forming a 'wet zone' with elevated temperature and elevated partial water vapor pressure near the hydrophobic PTFE membrane. Furthermore, it increases salt rejection by preserving the hydrophobic membrane's pores from wetting [134]. In addition, the modified layer serves as an additional barrier which decreases heat and energy loss. According to previous work [30] and our experience, spraying the Fe-CNTs solution did not penetrate the membrane's pores, therefore, properties of the PTFE membrane i.e. porosity, hydrophobicity, and pore size are kept unmodified following the spray coating.

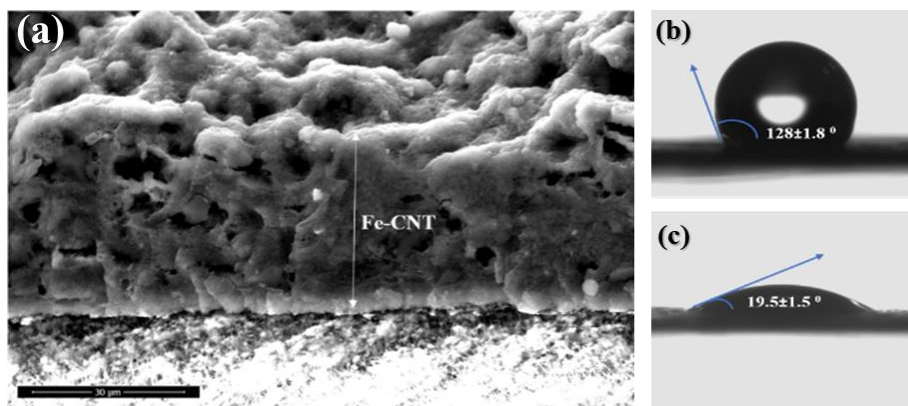


**Figure 4. 3.** Surface characterization of the Fe-CNTs layer: (a) SEM cross section of Fe-CNTs/PTFE membrane; (b) Water contact angle of PTFE commercial membrane; (c) Water contact angle of Fe-CNTs/PTFE membrane.

#### 4.1.4 Static Heating

To estimate the required membrane thickness and mass loading for MD in flow conditions (section 4.1.5), the ability to heat water was initially estimated under static conditions by placing a water droplet with a volume of 10  $\mu\text{L}$  on the membrane surface and measuring the temperature increase rate by an IR temperature detector (Helect Non-Contact Digital Laser, H1020). Two mass loadings of FeNPs and CNTs were evaluated according to our assessment of the mechanical stability and robustness of the layer, additional layer thicknesses were also assessed in section 4.1.5.3. The deposited Fe-CNTs mass was calculated according to the volume and mass of spraying solution used per fabricated membrane. The thickness of the membrane was evaluated by imaging of the membrane cross-section using SEM. For a 30  $\mu\text{m}$  layer thickness, we estimated a mass of 23 g Fe-CNTs/ $\text{m}^2$  (addressed as high load coating) and for a thickness of 14  $\mu\text{m}$ , we estimated a mass of 12 g Fe-CNTs/ $\text{m}^2$  (addressed as low load coating). For both membranes, a constant IH (283 kHz, 2 kW) resulted in instantaneous surface heating leading to a temperature increase of the water droplet (Figure 4.4). Heating rate was dependent on the mass loading

and calculated according to the temperature gradient per time ( $\frac{\Delta T}{\Delta t}$ ). For the high load membranes, water evaporated in about 20 s while for the low load membrane, the process took about 3 minutes. A heating rate of about 7°C/s was detected for the high load coating in comparison to the low load coating which was about 18 times lower (0.39°C/s). According to these results, all following experiments were performed using a high load coating membrane.

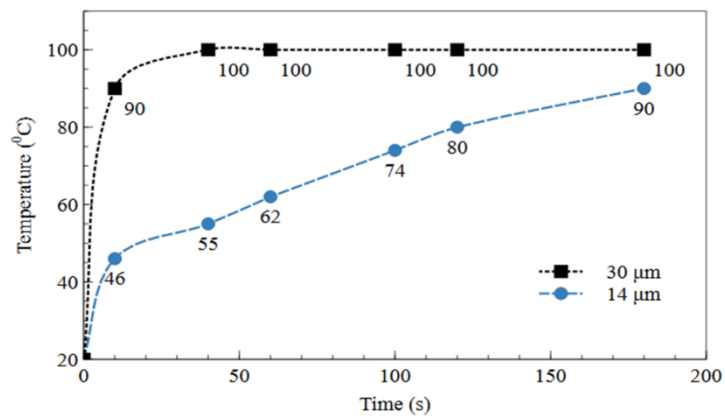


**Figure 4. 4.** Water droplets temperature on the Fe-CNTs membrane as a function of membrane coating thickness and contact time.

#### 4.1.5 Flow Experiments

To examine the impact of the modified Fe-CNTs membrane on the MD process, VMD flow experiments were performed. A cold feed solution at room temperature (RT) was directly heated on the Fe-CNTs coated PTFE membrane by IH. The feed solution penetrated the porous hydrophilic Fe-CNTs layer in which iron nanoparticles were rapidly heated by IH. Subsequently, heat was conducted to and by CNTs and transported to the water. The elevated temperature of the water leads to an increase in vapor pressure and vapor transport across the hydrophobic base support (Figure 4.1). Distillate flux was obtained by vacuum and condensation of the water vapors. To find optimum operational

conditions and understand the system limitations, we performed a parametric evaluation by changing operational parameters: vacuum, flow velocity, layer mass and thickness, and solution salinity. Results, in terms of distillate flux and salt rejection, are presented and discussed in the following sections.

#### **4.1.5.1 Impact of Flow Rate**

The impact of feed flow velocity on distillate flux and salt rejection was evaluated using constant operational parameters (i.e. 35 g/L NaCl feed concentration and 30 kPa vacuum pressure), while flow velocity varied between 1.05 to 11.25 cm/min. Low flow velocities were selected to allow high contact time between the feed solution and the membrane surface, thus, obtaining the maximum efficiency of the IH. The hydraulic residence time (HRT) in the system changed according to the flow velocity, ranging from 457s to 43s for 1.05 to 11.25 cm/min, accordingly.

While in conventional MD processes, high flow velocities are required to increase the distillate flux as the feed cools down when it is in contact with the cold membrane surface, we see a opposite phenomenon in the IH based MD system (Figure 4.5a). Low flow velocity of 2.33 cm/min leads to a high distillate flux of about 4 kg/m<sup>2</sup>.h while increasing the flow velocity leads to a decrease in flux to a minimum of about 2.8 kg/m<sup>2</sup>.h at the highest flow velocity measured. Salt rejection also decreases while flow velocity increases. Distillate flux changes according to the temperature of the solution, therefore, at high flow velocity, the short contact time with the membrane surface leads to less heat transport and lower temperature at the water-membrane boundary. The decrease in distillate flux as a result of lower water vapor pressure is described by the Antoine equation in which water vapor pressure has an exponential dependence on temperature [50,64–66].

In our results, we see that flow velocity can be optimized to maximize the flux and salt rejection. This can be illustrated by considering the effect of flow velocity on the HRT and concentration polarization. The increase of feed flow rate improves the mixing in the flow channel. This leads to two phenomena at the boundary layer: 1) a decrease in temperature due to the short contact time and 2) a decrease in the concentration layer thickness. A lower thickness of boundary layer is followed by an increase in distillate flux [148] while concentration polarization formed by concentration at the feed-membrane interface [214]. In RF-VMD, at very low flow velocities (lower than 2.33 cm/min), concentration polarization is relatively notable due to the rapid increase of temperature and water evaporation through the membrane, leading to lower distillate flux. Increasing the flow velocity improves mixing and decreases concentration polarization by lowering the concentration boundary layer. However, the impact of high flow velocity, more than 2.33 cm/min in our specific case leads to a decrease in HRT, lower water temperatures, and lower distillate flux. It can be concluded that increasing the flow velocity more than a certain value has a negative impact on the distillate flux while at very low flow velocities, the influence of the concentration boundary is dominant.

Furthermore, salt rejection is also influenced by the flow velocity and increases to the maximum value of about 99 % at a flow velocity of 2.33 cm/min, whereas at higher flow velocities of 11.25 cm/min, it reduced to about 96%. The decrease in salt rejection can be explained by the low boundary layer resistance, for flow velocities more than 2.33 cm/min, which allows salt to pass through the membrane [148]. Ergo, the optimized operation flow velocity at 2.33 cm/min was determined in terms of highest distillate flux and salt rejection.

#### **4.1.5.2 Impact of Vacuum Level**

Assessing the vacuum level for the RF-VMD system was required to find optimum operating conditions with a maximum distillate flux while retaining a high salt rejection. Therefore, the influence of vacuum level on the performance of Fe-CNTs membrane was evaluated at two flow velocities and a range of vacuum levels. Vacuum level was shown to impact the flux and salt rejection as expected according to the relevant literature [148](Figure 4.5b).

For both evaluated flow velocities, distillate flux increased linearly with the increase of vacuum pressure on the permeate side as a result of the overall increase in driving force as described by Wang et al. (2012) [215]. In terms of membrane selectivity, salt rejection decreased with the increase in vacuum level, since the pressure may exceed the liquid entry pressure of the hydrophobic membrane. According to the obtained results, an optimal working pressure of 20 kPa was determined as it retains maximum salt rejection and relatively high distillate flux.

#### **4.1.5.3 Impact of Membrane Coating Thickness**

Since in RF-VMD, water temperature is influenced by the mass of conductive/magnetic material subjected to the magnetic field, the thickness and mass of the membrane coating should have a significant influence on the MD distillate flux. As previously discussed for the static heating experiments (section 4.1.4), Fe-CNTs mass loading can be defined according to the deposited solution volume and by analyzing SEM cross section images of the membrane. While a thick hydrophobic membrane leads to reduced distillate flux due to the increase of mass resistance [70], a thick conductive layer improves distillate flux for

RF-VMD because of higher heat production and enhancement of the driving force. It should be noted that the hydrophobic layer is not modified.

The impact of the Fe-CNTs layer thickness on the distillate and rejection was evaluated for a range of coating thicknesses (6-30 $\mu\text{m}$ ) using previously optimized operational parameters (i.e. flow velocity of 2.33 cm/min and a vacuum pressure of 20 kPa). Figure 4.5c shows the correlation between mass loading, layer thickness, and distillate flux. Salt rejection was not impacted by the thickness and remained elevated, i.e. 99 %. The thickness of the Fe-CNTs layer directly impacts the distillate flux. A thicker Fe-CNTs layer leads to higher distillate flux as a result of increase in driving force due to the increased temperature gradient at the membrane-water interface. Our results show that the distillate flux can be increased 4 times only by controlling the deposited mass on the hydrophobic PTFE membrane. Furthermore, since the deposited layer impacts only the hydrophilic layer which has high porosity, it has no impact on mass transport between the coating and the active membrane (PTFE) and therefore no limitations on distillate flux. According to the results, a 30  $\mu\text{m}$  width layer membrane was selected for further experiments as it was mechanically stable and produced high distillate flux.

#### **4.1.5.4 Impact of Feed Concentration**

MD can be used for the treatment of extremely concentrated solutions with limited influence on distillate flux in comparison to pressure-driven membrane processes such as RO which are impacted by concentration polarization [26]. Nevertheless, flux in MD systems is influenced by the decrease of partial vapor pressure according to Raoult's law, leading to a decrease in the MD process driving force with the increase in salt concentration [92].

As RF-VMD distillate flux production is based on the same physical principles as other thermally driven membrane processes and influenced by temperature and salinity, it is important to determine the influence of high salt concentration on its performance. Three feed solutions with increasing salinities simulating common wastewater/water species, i.e. 10 g/L (saline water), 35g/L (seawater), 100 g/L (RO concentrated brine) were tested and compared to conventional MD (Figure 4.5d). Experiments were performed according to the optimal conditions obtained in the previous steps.

While conventional VMD [24,26] and self-heating MD based on altering current [188] show a decrease in flux as a function of increased salinity, RF-VMD shows (Figure 4.5d) a linear increase in flux with the increase of feed salinity whereas salt rejection stayed constant i.e. 99 %. As increased salinity leads to a decrease in partial vapor pressure of water, an additional phenomenon overcomes the decrease in partial pressure and leads to the increase of distillate flux.

Wang et al. [216], and Sefy et al. [217] showed that hydrogen-bonds in pure water are weakened in the presence of magnetic fields. Furthermore, Chang et al. showed that in the presence of ions, the magnetic field decreases water clusters' size; therefore, a high concentration of ions such as  $\text{Na}^+$  and  $\text{Cl}^-$ , may decrease the energy required to break hydrogen-bonds between water molecules. The applied magnetic field enhances the mobility of  $\text{Na}^+$  and  $\text{Cl}^-$  ions which damages the hydrogen network of the water. As a result, water molecules' mobility in a highly-concentrated sodium chloride solution increases [218]. Therefore, our hypothesis is that a high frequency magnetic field and high salt concentration may lead to elevated water temperature coupled with increased water evaporation as a result of the hydrogen bonds weakening [216–219]. According to our

results, which show higher flux at high salinity, we estimate that the influence of high salinity on mobility in IH is dominant over the decrease of partial vapor pressure. Experimental comparison between the RF-VMD system and conventional VMD shows a significant advantage to the RF-VMD system with a distillate flux of about  $5 \text{ kg/m}^2\cdot\text{h}$  for a  $100 \text{ g/L}$  NaCl solution in comparison to about  $0.3 \text{ kg/m}^2\cdot\text{h}$  for a conventional VMD at similar conditions. According to these results, thermally conductive membrane distillation by IH can be considered a promising technology for treatment of high salinity brine due to the overall high distillate flux and salt rejection.

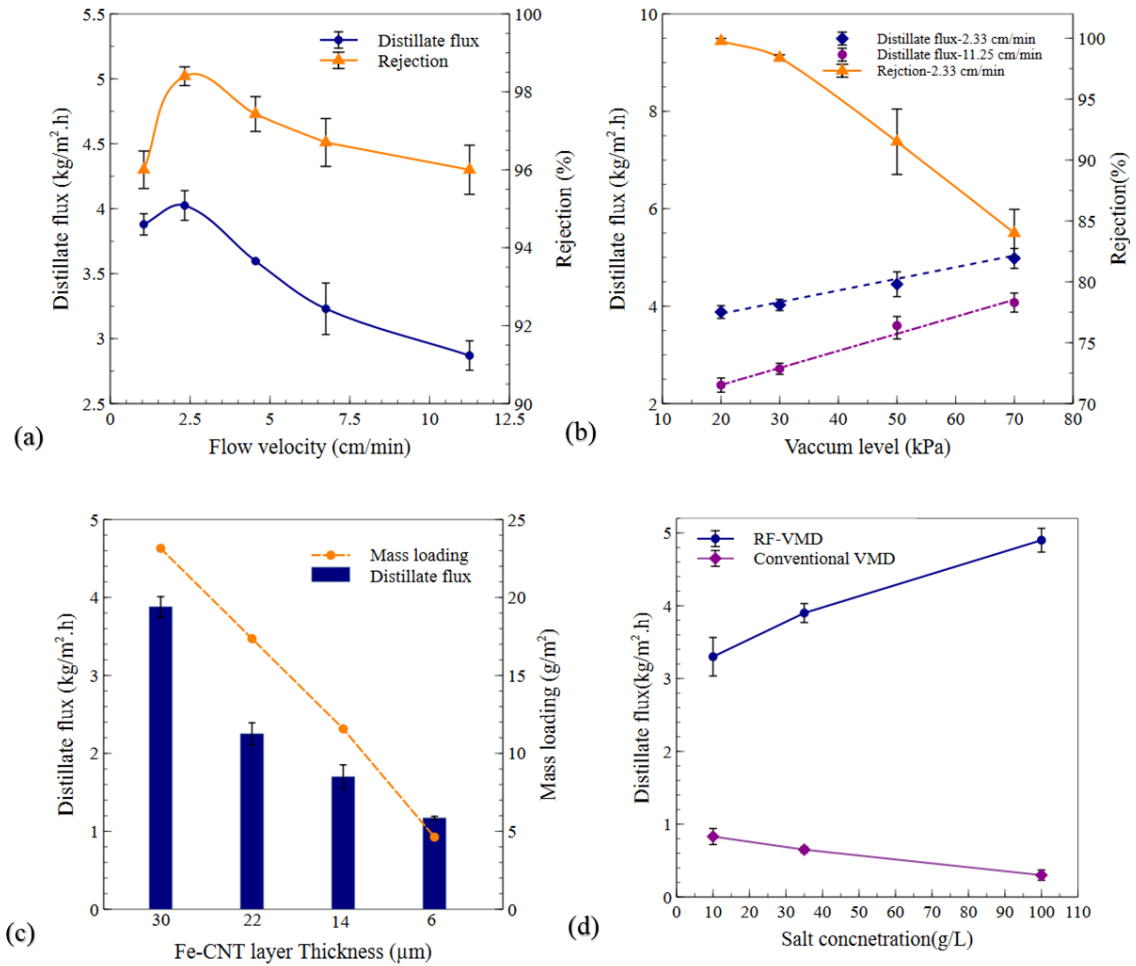


**Figure 4. 5.** (a) Impact of flow velocity on distillate flux and salt rejection at 30 kPa vacuum pressure; (b) Impact of vacuum level on distillate flux and salt rejection with 2.33

and 11.25 cm/min feed flow velocity; (c) Impact of Fe-CNTs loading and layer thickness on distillate flux at 20 kPa vacuum pressure, and 2.33 cm/min feed flow velocity; (d) Impact of feed salt concentration on distillate flux of RF-VMD and conventional VMD at 20 kPa vacuum pressure, and 2.33 cm/min feed flow velocity.

#### **4.1.6 Comparison between Conventional VMD and RF-VMD**

To evaluate the feasibility of the RF-VMD system, we compared it to conventional VMD in terms of distillate flux and specific heating energy. We used a commercial unmodified PTFE membrane in a conventional VMD setup under the same operating conditions. Both membranes were fed with a solution containing 35 g/L NaCl and kept under the previously optimized operating conditions. The feed to the RF-VMD system was kept at  $20 \pm 2$  °C and the feed to the conventional VMD was preheated to  $65 \pm 2$  °C. Temperature was selected according to our measurements as the average temperature in the RF-VMD was about 65 °C with a flow velocity of 2.33 cm/min (data acquired using IR temperature meter and from COMSOL simulation).

Results (Figure 4.6a) show that RF-VMD distillate flux is significantly higher than conventional VMD flux as a result of the heated membrane surface while salt rejection was 99% for both systems. The difference can be attributed to three phenomena: first, the Fe-CNTs layer provides an additional layer with a hydrophilic–hydrophobic structure on the PTFE membrane. The porous hydrophilic layer heats the solution while the hydrophobic layer rejects the liquid solution (water and dissolved ions). Since water convectively transports from the feed solution into the hydrophilic layer and heats up inside, water vapor formation on the Fe-CNTs/PTFE membrane will be higher than at the surface of a PTFE membrane. Second, the hydrophilic–hydrophobic dual layered structure provides low heat loss through the membrane compared to a thin commercial PTFE membrane. The hydrophilic layer is assumed to lead to water absorption and heating, while both the

hydrophilic and hydrophobic layers prevent heat loss through the membrane matrix. Finally, while conventional MD suffers from temperature polarization due to the temperature difference between the heated feed and cold membrane interface ( $T_{fb} > T_{fm}$ ) (Figure 4.6b) [24], in the RF-VMD module, thermal polarization is negligible since the bulk feed temperature is notably lower in comparison to the interfacial temperature ( $T_{fb} < T_{fm}$ ) (Figure 4.6c). As a result, more water vapor forms at the Fe-CNTs/ PTFE interface, resulting in high distillate flux.

Specific heating energy consumption ( $Q_s$ ), which is the ratio of heating energy (W) to distillate flow rate (kg/h) was calculated for both systems (see Eq. 4.1).

$$Q = \dot{m}c_p(T_f - T_{room}) \quad \text{Eq. 4.1}$$

Where  $Q$  is the heating energy consumption,  $\dot{m}$  is the feed solution mass flow rate,  $c_p$  is the specific heat of feed,  $T_f$  is the feed temperature, and  $T_{room}$  is the room temperature[220].

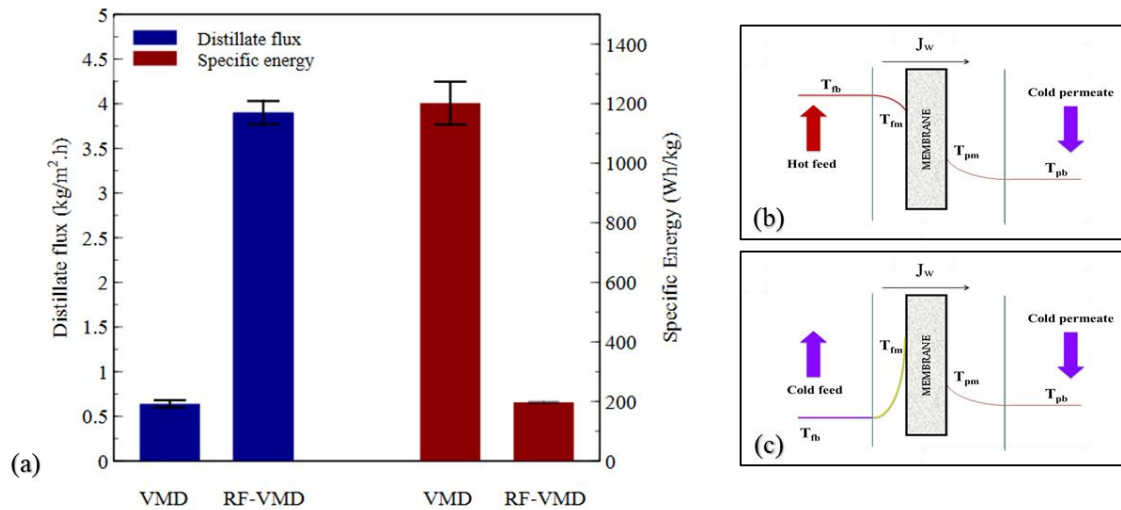
Results indicate that the RF-VMD system has a lower specific energy i.e. 197 Wh/kg in comparison to the conventional VMD, i.e. 1202 Wh/kg (Figure 4.6a). The attained specific heating energy of the RF-VMD system is lower than some values reported in the literature on conventional MD systems [191,220,221] along with self-heating MD systems [188,222,223].

Table 4.1 shows a comparison of performance and energy consumption of direct heating MD systems as described in the literature. Three heating approaches are evaluated, including photothermal, ohmic, and IH heating. The RF-MD system is among the higher performances in terms of high distillate flux with lowest heating energy. The calculated values of gain output ratio (GOR) (Table 4.1), which defines the ratio of the water

evaporation energy to the energy input of the system[188], show a high energy efficiency of RF-VMD. This is attributed to the role of the IH coupled with the dual layered membrane structure, the heating of Fe-CNTs layer, negligible thermal polarization, and low heat loss. According to the experimental results, RF-VMD systems can be considered as an efficient MD technology in terms of relatively low heating energy consumption with high distillate flux and high salt rejection.

**Table 4. 1.** Comparison of performance and energy from different direct heating MD systems

Heating method	Heating materials	Input energy (kW/m <sup>2</sup> )	Flux (kg/m <sup>2</sup> .h)	Q <sub>s</sub> (kWh/kg)	GOR	Efficiency (%)	Ref.
Solar irradiation	cESM-CNTs	1	1.15	0.87	0.78	>75.6	[222]
Solar irradiation	Carbon black-PVA	0.7	0.5	1.4	0.48	53.8	[223]
Ohmic heating	CNTs-PVA	11.1	7.5	1.23	0.54	NA	[188]
Induction heating	Fe-CNTs	0.781	4	0.2	3.45	>84	This study



**Figure 4. 6.** (a) Distillate flux and specific heating energy of Fe-CNTs/PTFE membrane in RF-VMD and unmodified PTFE membrane in conventional VMD at 2.33 cm/min feed flow velocity and 20 kPa vacuum pressure; Temperature Polarization membrane in (b) conventional VMD (c) RF-VMD.

#### 4.1.7 Simulation and Scale up

Conventional and IH based VMD, 2D models were developed and compared with the experimental data to verify the models' accuracy. This was done by comparing the calculated distillate fluxes, based on mean vapor flux on distillate–membrane interface, with obtained experimental distillate fluxes.

Simulated and experimental data including distillate flux at a range of feed flow velocities are shown in Table 4.2 for both RF-VMD and conventional VMD. All data was collected at a feed concentration of 35 g/L NaCl with 20 kPa vacuum pressure, while the feed inlet temperature for RF-VMD and conventional VMD was  $20^{\circ}\text{C} \pm 2$  and  $65^{\circ}\text{C} \pm 2$ , respectively. For the IH based system FEM model, we used a constant heat flux equal to 2.46 W ( $781.25 \text{ W/m}^2$ ) to simulate the produced heat at the membrane surface as a result of IH. This value was obtained according to measurements of the average temperature of the feed solution on the surface of Fe-CNTs membrane exposed to the magnetic field. The computational influence of feed flow velocity on the water distillate flux is in consistent with the experiment results. Higher feed velocity decreases the distillate flux of RF-VMD due to the decrease in hydraulic contact time while distillate flux of conventional VMD increases with higher feed velocity as a result of mixing and low boundary layers[148].

Simulation results were corresponding to the experimental results with average errors of less than 4.0%, thus, confirming that the developed two-dimensional FEM model based on the momentum, mass, and heat transfer is precise. Therefore, the model can be used to predict the impact of parametric changes on conventional VMD operation and VMD with a self-heating membrane such as seen when applying IH in our case.

**Table 4. 2.** Comparison between simulation and experimental results of distillate flux for RF-VMD and conventional VMD

System	Flow velocity (cm/min)	T <sub>in</sub> (°C)	Experimental flux (kg/m <sup>2</sup> .h)	FEM model flux (kg/m <sup>2</sup> .h)	Error (%)
<b>RF-VMD</b>	2.33	20	4.025	4.17	3.6
<b>RF-VMD</b>	4.55	20	3.6	3.71	3.05
<b>RF-VMD</b>	6.75	20	3.23	3.21	0.62
<b>RF-VMD</b>	11.25	20	2.87	2.65	7.6
<b>VMD</b>	2.33	65	0.65	0.62	4.6
<b>VMD</b>	11.25	65	1.39	1.42	2.16
<b>VMD</b>	14	65	1.53	1.58	3.26

Average error: 3.56%

The differences between solution temperature and distillate flux along the membrane module for both systems are shown in Figure 4.7. Data was calculated with a hot feed (65 °C) for conventional VMD and a cold feed (20 °C) for the RF-VMD system. All simulations were done at constant flow velocity 2.33 cm/min and 35 g/L of NaCl. Our results show a rapid decrease in temperature along with a decrease in distillate flux for the conventional VMD module (Figure 4.7 a, b). According to the data, flux reached minimum value within the first two centimeters of the module as a result of the heat loss due to water evaporation [188] and contact with the cool membrane surface. In contrast, the RF-VMD module (Figure 4.7 c, d) reached a high flux value within the first two centimeters of the module with an overall rapid increase in solution temperature and distillate flux. Simulations are in agreement with experimental results, confirming that the RF-VMD system results in elevated membrane surface temperatures and higher distillate fluxes in comparison to conventional VMD.

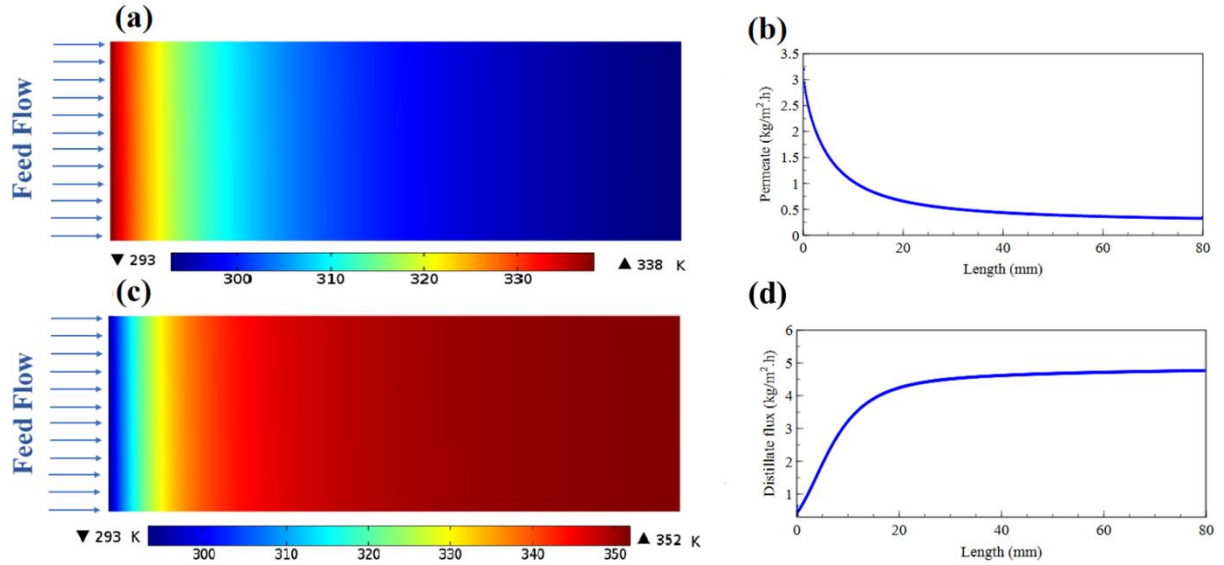


**Figure 4. 7.** (a) FEM simulation of feed temperature distribution and (b) distillate flux values along the membrane in the conventional VMD model with feed temperature 65 °C; (c) FEM simulation of feed temperature distribution and (d) distillate flux values along the membrane in the RF-VMD model with feed temperature 20 °C; feed flow velocity for both systems: 2.33 cm/min.

We also evaluated the ability of scaling up the RF-VMD system using the same FEM simulated approach. Our scaled model is based on a larger membrane (1-meter length, 1-meter wide, and 1 mm height flow channel). Results show that the temperature in the flow channel is influenced by the longer residence times. Therefore, a longer membrane module leads to an overall higher temperature and higher distillate flux even when flow velocities are relatively high (Figure 4.8a).

Heat flux can be enhanced for IH based systems by increasing the Fe-CNTs layer thickness, induction heating power source, frequency, and coil structure. We evaluated the heat flux required to use an RF-VMD system for industrial application with a higher flow velocity i.e. 750 cm/min. Our results show that even at high flow velocities, distillate flux can be significantly increased by controlling the heat flux. Therefore, heat fluxes of 781.25 W/m<sup>2</sup> and 4000 W/m<sup>2</sup> showed the ability to distillate 0.5 and 8 kg/m<sup>2</sup> hr., accordingly (Figure

4.8b). Based on the scale up estimations (Figure 4.8c), the specific heating energy to distill one kg of water is about 0.5 kWh at heat flux of  $4000 \text{ W/m}^2$ . This confirms the efficiency of RF-MD in comparison to conventional VMD systems and the other self-heating MD according to data acquired from the literature and our FEM model [188].

Scaling up the RF-VMD requires addressing engineering challenges related to the tradeoff between flow rates, heat loss, and concentration polarization near the heated membrane and additional technical aspects related to the size and power of the IH system and inducer coil.

As the hydraulic contact time impacts the performance and flux of the system, increasing the flow velocity would require optimization of ratio between flow velocity and heat flux. This can be done through several mechanisms i.e. increasing the Fe-CNTs layer thickness, increasing the induction power, varying the magnetic frequency, and controlling the coil structure. Furthermore, to gain higher flux, a higher surface area is required; therefore, hollow fiber modules should be considered instead of flat sheets, which are less efficient in terms of surface area per volume. Finally, scaling up the IH system will require considering the materials used for the modules, as they must be made on non-conductive and non-magnetic materials as polymers and plastics.

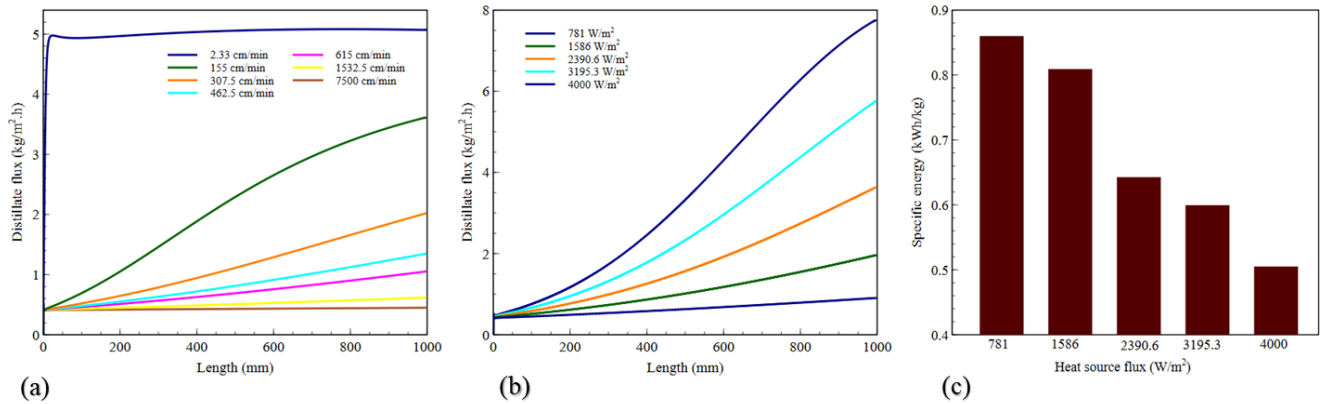


**Figure 4. 8.** Impact of system scaling on system performance by using a FEM simulation of a scaled-up system: (a) Distillate flux along a membrane module as a function of flow rate with heat source flux: 781.25 W/m<sup>2</sup>, (b) Distillate flux along a membrane module as a function of heat source energy with flow velocity 750 cm/min; (c) Specific heating energy of RF-VMD as a function of heat source energy at 750 cm/min feed flow velocity.

#### 4.1.8 Conclusions

Composite magnetic-hydrophilic/hydrophobic membranes were fabricated by spraying nano particles of iron oxide coated CNTs on the surface of hydrophobic PTFE membrane. Radio frequency electromagnetic field was successfully employed as a means to directly heat the saline water on the surface of the membrane in a VMD conformation. Heating was found to be related to the loading of Fe-CNTs on the base support, where higher mass loading provides higher distillate flux. The process was optimized in terms of conductive layer thickness, feed flow rate, and vacuum level. The system behaves different from conventional VMD processes and optimum distillate flux was obtained at low flow velocities. Flux was shown to be affected by the hydraulic residence time in the flow cell as a result of heat transport by diffusion and convection from the membrane to the surrounding solution. In addition, RF-VMD was shown to be more efficient for feed solutions containing high salinity. Therefore, it can be potentially used for concentrated

brine treatment. Our CFD simulations were validated by experimental results and predict the ability to use IH-VMD for larger scale systems.

## **4.2 Scaling Mitigation in Radio-Frequency Induction Heated Membrane Distillation**

**Preface:** The contents of this section are in part based on a published article in Journal of Membrane Science: **Anvari, A.**, Kekre, K. M., Ronen, A., " Scaling mitigation in radio-frequency induction heated membrane distillation", Journal of membrane science 600 (2019): 117859 [195].

### **4.2.1 Introduction**

In this section a comprehensive investigation of scaling and scaling mitigation behavior of MD system, based on RF-IH under high salinity feed conditions, specifically addressing  $\text{CaSO}_4$  scaling due to its severity, will be done. We evaluate and analyze the impact of operating parameters and feed concentration on distillate flux and scaling properties (i.e., crystal size and quantity) and compare the RF-based approach (RF-VMD) to a conventional VMD system (C-VMD).

### **4.2.2 Distillate Flux Under Scaling Conditions**

In order to characterize the impact of RF-IH on  $\text{CaSO}_4$  scaling, C-VMD and RF-VMD systems were fed with synthetic solutions designed to simulate seawater salinity (35 g/L NaCl and 1.8 g/L of  $\text{CaSO}_4$ ).  $\text{CaSO}_4$  concentration was selected to be close or above the saturation limit of  $\text{CaSO}_4$  according to specific temperatures. At 25°C and 65 °C, the maximum saturation concentrations are 2.4 g/L and 1.5 g/L, respectively [224,225].

Scale development of both systems was evaluated according to operational parameters of the MD system, i.e. flux changes over time. Both systems had similar inlet conditions based

on previous section (Section 4.1), i.e., flow velocity of 2.33 cm/min and a vacuum pressure of 20 kPa, but different feed temperatures of 65°C for C-VMD and 20 °C for the RF-VMD. While distillate flux changed during our experiments, no decrease in rejection was observed in both systems (NaCl rejection>99%). Although the deposited inorganic salt layer was shown to decrease the hydrophobicity of the PTFE membrane and cause a decrease in rejection [47], the modified dual hydrophilic/hydrophobic membrane structure was previously shown to reduce the influence of scaling on membrane rejection [134].

Distillate flux changes are addressed as normalized flux (N.F) values and are presented as a function of time (Figure 4.9). The C-VMD system ( $J_0=0.6\pm0.3$ ) resulted in a 50% reduction in N.F over 7 hours of experiment, the reduction is attributed to the precipitation of  $\text{CaSO}_4$  crystals on the membrane surface due to CP. Scaling occurs as calcium and sulfate ions are rejected by the membrane, leading to their supersaturation and precipitation on the membrane surface. In addition to CP, the elevated temperature was shown to decrease the solubility of  $\text{CaSO}_4$  due to its exothermic formation energy [226]. In all experiments, the average solution temperature was 65 °C, leading to supersaturation and resulting in  $\text{CaSO}_4$  crystals formation on the membrane surface. While scaling led to the N.F decline in the C-VMD, an opposite behavior was seen in the RF-VMD system ( $J_0=3\pm0.2$ ), where N.F values increased by up to 115% and stabilized within the first two hours of heating as presented and discussed in our previous section. The proposed explanation for the RF-MD scaling mitigation mechanism is presented in the next section (section 4.2.3).

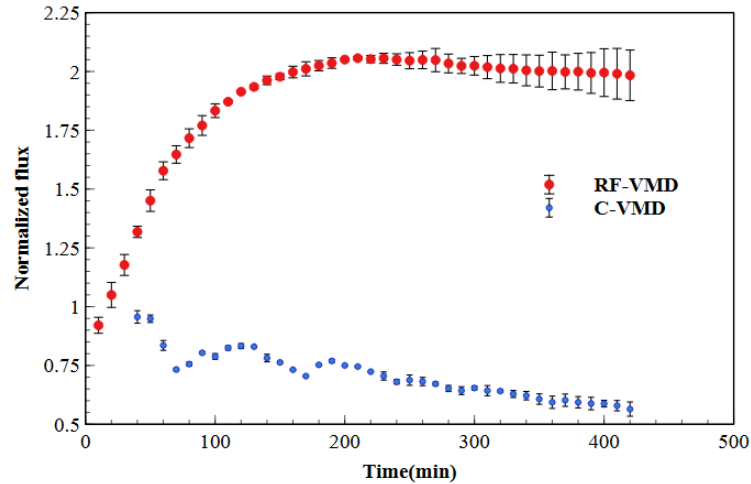


**Figure 4. 9.** N.Fs of C-VMD and RF-VMD systems as a function of time at feed velocity of 2.33 cm/min and vacuum pressure of 20 kPa for the distillation of 35 g/L NaCl with 1.8 g/L CaSO<sub>4</sub> solution and feed inlet temperatures of 65 °C and 20 °C, respectively.

EDX and SEM images of the membranes' surface following distillation (feed solution of 1.8 g/L CaSO<sub>4</sub> and 35 g/l NaCl) are presented in Figure 4.10. SEM image of the C-VMD shows the presence of cubical needle-like shaped crystals, which are hypothesized as the reason for N.F decline (Figure. 4.10a). EDX analysis (Figure 4.10c) indicates the presence of calcium, oxygen, and sulfate elements, which are the main components of CaSO<sub>4</sub> crystals. In contrast, no apparent crystals were detected at the surface of the membrane following the RF-VMD processes (Figure 4.10 b, d). EDX data also confirms the presence of iron nanoparticles embedded in the CNTs matrix composing the membrane. The data obtained by EDX and SEM images are consistent with the distillate flux results, indicating that the RF-MD distillation process may result in limited or complete mitigation of CaSO<sub>4</sub> scaling.

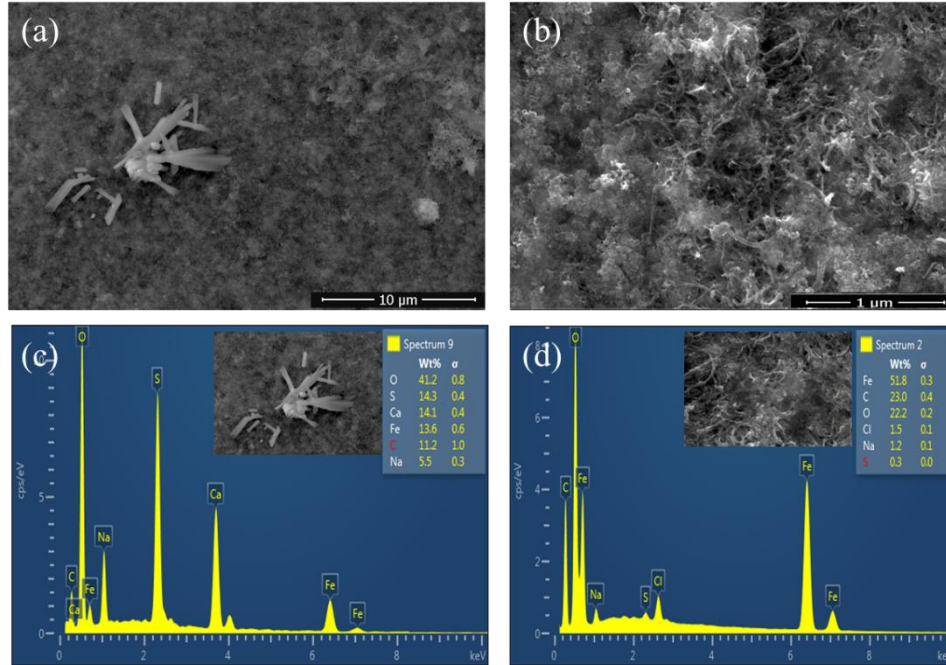


**Figure 4. 10.** Morphological images of used membranes’ surface in (a) C-VMD; (b) RF-VMD systems, and EDX images of selected parts of membranes in (c) C-VMD; (d) RF-VMD systems for the distillation of 35 g/L NaCl with 1.8 g/L CaSO<sub>4</sub> solution. Feed velocity of 2.33 cm/min, vacuum pressure of 20 kPa, and feed inlet temperatures of 65 °C and 20 °C, respectively.

#### 4.2.3 Proposed Scaling Mitigation Mechanism

Previous studies have described the influence of magnetic fields on ions and inorganic salt crystallization along with their fouling behavior by several mechanisms including an increase of nucleation and crystal growth in the bulk solution due to an increase in ion collision frequency in the magnetic fields and rapid ions reactivity in the water, leading to the lack of ions in the solution to precipitate [227–229]. In the current work, the RF-VMD system exhibits an increase in N.F rather than the decline as seen in C-VMD as a result of CaSO<sub>4</sub> scaling.

The results of this study provide a qualitative description of the RF-IH mechanism that leads to scaling mitigation and reduction. In order to address scaling phenomenon under RF-IH conditions, two plausible factors should be considered: (1) the influence of the high-

frequency electromagnetic field on  $\text{Ca}^{+2}$  and  $\text{SO}_4^{-2}$  ions collision, leading to crystallization in the bulk solution; (2) the influence of high frequency magnetic field on the mobility of  $\text{Na}^+$  and  $\text{Cl}^-$  ions, leading to damage of intermolecular bonding of  $\text{CaSO}_4$  crystals in addition to the damage of intermolecular bonding of water molecules. Ions exposed to an electromagnetic field were shown to be influenced by Lorentz force, which is perpendicular to the magnetic field and enhances linearly according to the ion's charge [230,231]. This leads to movement and fluctuation of ions and to enhance their collisions, resulting in improved crystal nucleation and the formation of small suspended  $\text{CaSO}_4$  crystals in the bulk solution [227–229,231–233]. As permeate drag force is influenced by size and mass [234], the suspended small crystals tend to remain in the solution rather than reach the membrane surface. Furthermore, Silva and et al. [235] showed that  $\text{Ca}^{2+}$  ions were more hydrated in a solution exposed to a magnetic field, resulting in the formation of small insoluble crystals because of the weak adhesion between cations and anions. Small suspended crystals can be more easily removed from the surface of the membrane by shear as a result of the cross-flow. The formation of crystals with small size under magnetic fields was addressed in several studies considering magnetic fields as a method to increase crystallization of inorganic salts in the bulk solution [227–229,236,237]. In order to prove the influence of RF-IH on the formation of crystals in our system's bulk solution, the concentrate stream was collected and evaluated for the average crystal number and size (Figure 4.11a-d). Several mL from the concentrate were imaged using light microscopy and images were analyzed by an image processing software. As theorized, a higher number of suspended crystals were detected following the RF-VMD ( $13,620 \pm 1,853$  crystals/ $\text{mm}^2$ ), while for C-VMD, a significant lower concentration of crystals was measured (i.e., 6 times

less,  $2,380 \pm 493$  crystals/ $\text{mm}^2$ ). In both cases, suspended crystals had an average size of 5-10  $\mu\text{m}$ , therefore, we assume larger crystals deposited on the membrane surface.

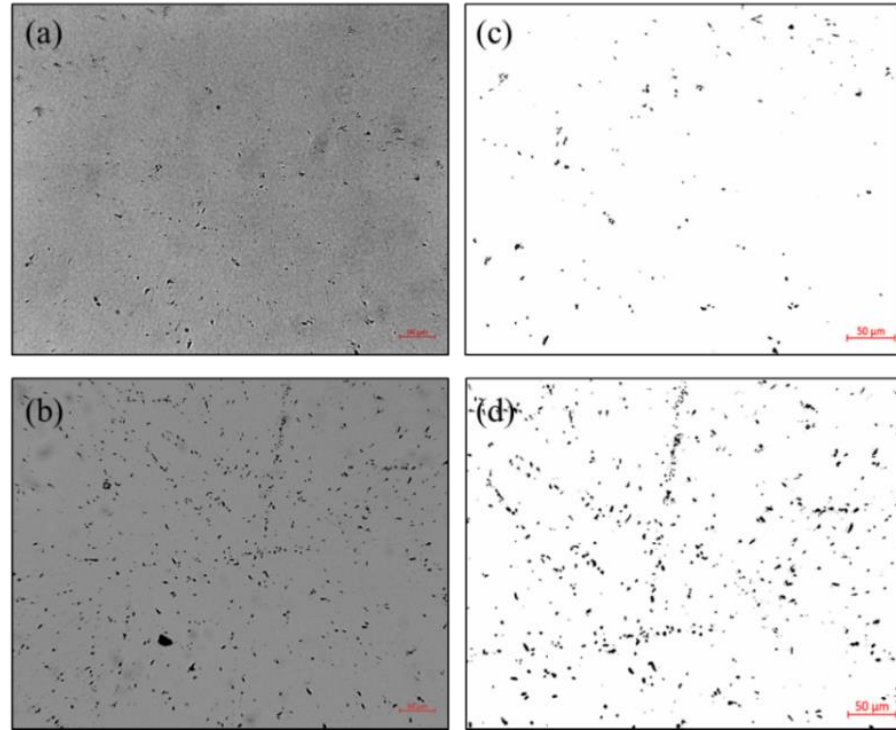


**Figure 4. 11.** Light microscopy images of the concentrated flow of (a) C-VMD; (b) RF-VMD, and ImageJ counting images for the concentrated flow of (c) C-VMD; (d) RF-VMD.

In addition to the influence of the high-frequency magnetic field on calcium and sulfate ions, the mobility of other ions may also contribute to scaling mitigation. High-frequency magnetic fields were shown to increase the mobility of  $\text{Na}^+$  and  $\text{Cl}^-$  ions [218]. High ion mobility and magnetic fields were shown to decrease  $\text{CaCO}_3$  scaling [230]. We assume a similar phenomenon occurs in our system, where the RF-IH leads to breaking of crystals' structure and prevents the formation and deposition of  $\text{CaSO}_4$  scaling.

As a result of both factors, scaling formation was limited in the RF-VMD system and no distillate N.F decline was observed. Furthermore, the N.F increased over time as a result of mainly direct heating of the feed on the surface of the membrane, the negligible TP along

with limited heat loss, and breaking of water hydrogen-bonds due to the high mobility as discussed previously. The temperature of Fe-CNTs layer exposed to the high frequency electromagnetic field increased over time until reaching a steady-state, therefore, the solution in contact with the heated layer is heated while passing through it, leading to higher distillate flux over time until it stabilizes (Figure 4.9). A schematic illustration of the proposed RF-IH impact on  $\text{CaSO}_4$  crystals deposition and mitigation in comparison to the scaling in the C-MD system is presented in Figure 4.12.

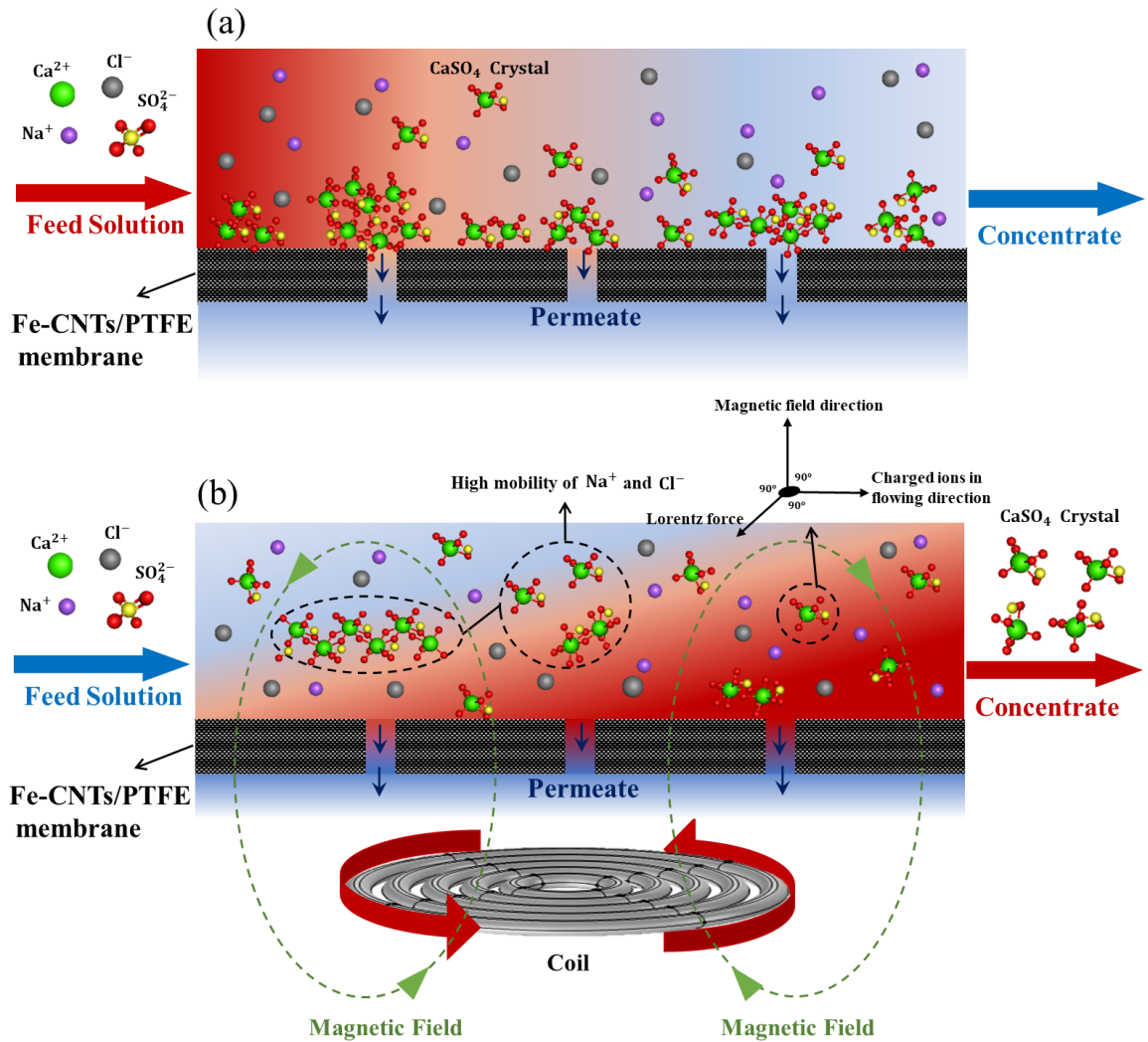


**Figure 4. 12.** Schematic illustration of (a)  $\text{CaSO}_4$  scaling in the C-VMD system (b) declined  $\text{CaSO}_4$  scaling in the RF-VMD system.

To assess the influence of ions and concentrations on scaling, we evaluated three solutions and measure the changes in N.F as a function of time; (S1) a solution containing only 35 g/L of NaCl; (S2) a solution containing a mixture of 35 g/L NaCl and 1.8 g/L CaSO<sub>4</sub>, and (S3) a solution containing only 1.8 g/L CaSO<sub>4</sub>. All the experiments were done at feed flow velocity of 2.33 cm/min, vacuum pressure of 20 kPa, and feed inlet temperature of 20 °C. When assessed with the RF-VMD system, there was no decline in N.F for all solutions (Figure 4.13); therefore, scaling formation can be considered negligible. The limited scale formation is assumed to be a result of the high-frequency magnetic field as discussed in the previous section. Furthermore, it should be noticed that for all the feed solutions, distillate flux increased to values higher than the initial flux value (i.e.,  $J > J_0$ , or  $N.F > 1$ , where  $J =$  up to 7 kg/m<sup>2</sup>.h and  $J_0 = 3 \pm 0.2$  kg/m<sup>2</sup>.h) as a result of the heating process through the membrane module (i.e., thermally conducting membranes with limited TP) and impact of the high frequency magnetic field on the mobility of ions, leading to enhanced water evaporation through breaking hydrogen bonds [218]. A maximum value of  $N.F = 2.5$  was measured for the solution containing only NaCl (S1) but, in contrast to the expected increase in N.F with the increase in ionic strength, the presence of both salts (i.e., NaCl and CaSO<sub>4</sub> in S2) led to a reduced N.F value ( $N.F = 2$ ). Furthermore, the solution containing only CaSO<sub>4</sub> (S3) resulted in the lowest N.F value ( $N.F = 1.4$ ). While sodium and chloride ions have shown to increase N.F (S1), the presence of calcium and sulfate led to a negative impact (S2). This is assumed to be a result of small crystals formed in the bulk solution as some of the sodium and chloride ions are presumed to break/damage the CaSO<sub>4</sub> crystals instead of weakening the water intermolecular forces (hydrogen bonds). The solution containing only calcium and sulfate (S3) led to the lowest N.F value as a result of crystal

formation and a relatively low ionic strength in comparison to the previous NaCl pure solution (S1). This demonstrates that both mobility and bulk crystallization, which are affected by the magnetic field, have an important role in the low or negligible scaling of RF-VMD systems.

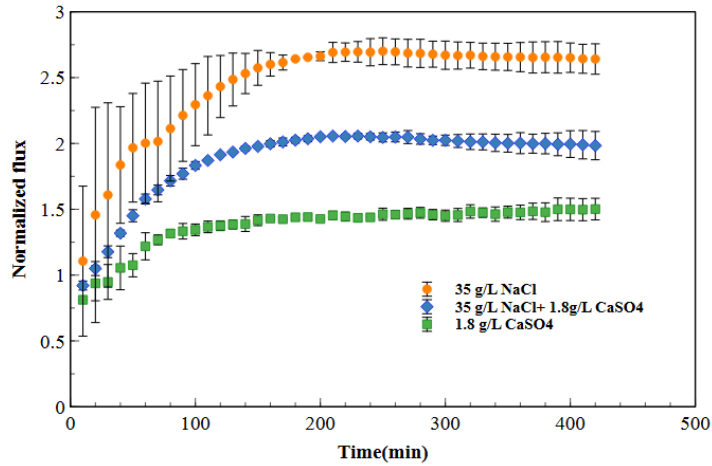


**Figure 4. 13.** Influence of RF-VMD on N.F as a result of solution composition. Feed velocity of 2.33 cm/min, vacuum pressure of 20 kPa, and feed inlet temperature of 20 °C.

#### 4.2.4 Impact of CaSO<sub>4</sub> Concentration

The influence of CaSO<sub>4</sub> concentration at supersaturation on the scaling was assessed for both MD systems. CaSO<sub>4</sub> concentration in the feed solutions was varied between 1.8 to 3.6 g/L (saturation index (SI) of 0.78 to 0.8, Eq. 3.1).

Based on the literature [37,54,238], the RO brine was initially used at a concentration of 1.8 g/L CaSO<sub>4</sub>. Higher concentration (i.e., supersaturated values such as 3.6 g/L) was assessed to describe extreme conditions where the RO brine is concentrated as part of a brine management approach or when assessing wastewater such as produced water. While the feed solution reached supersaturated conditions, it was continuously mixed at high velocity (high rpm) to prevent precipitation of CaSO<sub>4</sub> in the feed tank as done by Ge et al. [54] and Hou et al. [99]. The feed was not filtered to remove preformed crystals prior the

experiments as this will impact the concentration of ions entering the MD system. According to Yan et al. [37], CMD systems are influenced by different fouling mechanisms for filtered and unfiltered solutions as a result of the formed crystals in the feed. It was shown that for hypersaline supersaturated solutions (e.g. 3.6 g/L CaSO<sub>4</sub>), crystallization of CaSO<sub>4</sub> was based on homogenous nucleation in the bulk solution and heterogeneous nucleation on the surface of membrane simultaneously, both impacting the scaling behavior. The small bulk crystals speed up the homogeneous nucleation which can easily migrate and deposit on the membrane surface. Meanwhile, at the RF-VMD, the heating occurs while the solution is in the MD cell, therefore, it is expected to reach supersaturation conditions in the flow cell and when in contact with the membrane. Therefore, we did not filter the feed as we wanted to compare both systems (C-VMD and RF-VMD) at similar concentrations and assess 'realistic' conditions, where the system is exposed to both crystal formation mechanisms.

In this study, as expected for supersaturation conditions ( $SI > 0$ ), the C-VMD system (Figure 4.14a) showed a decrease in N.F with the increase of Ca<sup>+2</sup> and SO<sub>4</sub><sup>-2</sup> concentrations due to crystals formation and growth. Following a 420 mins filtration experiment, distillate flux was reduced by more than 50% for all CaSO<sub>4</sub> containing solutions with the maximum reduction for the highest concentration of CaSO<sub>4</sub> (i.e., 3.6 g/L of CaSO<sub>4</sub>). The N.F of the RF-VMD system, however, did not decrease over time (Figure 4.14b) and displayed a similar trend as previously shown (Figure 4.13). Interestingly, while the high concentration of CaSO<sub>4</sub> did not decrease N.F with time, it decreased the maximum N.F value. For the solution containing 1.8 g/L of CaSO<sub>4</sub>, the maximum N.F obtained by the system was 25% lower than the solution containing only NaCl, and for a higher concentration of 3.6 g/L

CaSO<sub>4</sub>, the N.F was reduced to about 44% of the N.F with only NaCl. The change in N.F values is hypothesized to be a result of the presence of Ca<sup>+2</sup> and SO<sub>4</sub><sup>-2</sup> ions and their crystals in the bulk solution and their influence on hydrogen bonds breaking by Na<sup>+</sup> and Cl<sup>-</sup> ions as previously discussed.

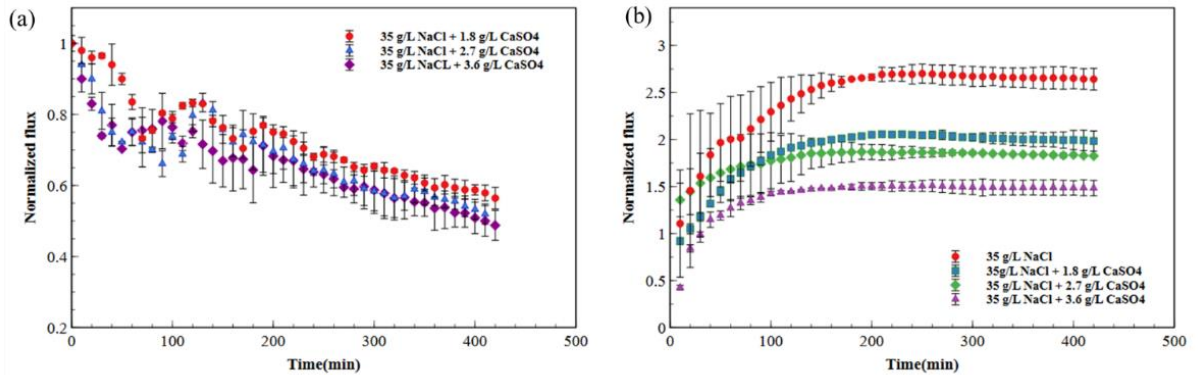


**Figure 4. 14.** Influence of CaSO<sub>4</sub> feed concentration on the N.F of (a) C-VMD; (b) RF-VMD systems. Feed velocity of 2.33 cm/min, vacuum pressure of 20 kPa, and feed inlet temperatures of 65 °C and 20 °C for C-VMD and RF-VMD, respectively.

SEM images of the membranes following the distillation of solutions containing high CaSO<sub>4</sub> concentration (3.6 g/L CaSO<sub>4</sub>) are shown in Figure 4.15 and include EDX analysis to confirm crystal composition. While imaging of the membranes following C-VMD and RF-VMD shows the presence of CaSO<sub>4</sub> crystals, there is a significant difference in crystal size and concentration between the assessed systems. SEM analysis of the C-VMD membrane (Figure 4.15a) showed multiple large CaSO<sub>4</sub> crystals, with sizes larger than 200 μm. When comparing these results with the previous data regarding the lower CaSO<sub>4</sub> concentration (1.8 g/L CaSO<sub>4</sub>, Figure 4.10a), we see an increase in crystal size and overall number of crystals. This confirms the data obtained regarding the influence of CaSO<sub>4</sub> concentration and N.F decrease, as seen in Figure 4.14a. While for the RF-VMD system, no crystals were found on the membrane surface for low CaSO<sub>4</sub> concentrations (1.8 g/L

CaSO<sub>4</sub>, Figure 4.10b), higher concentration of CaSO<sub>4</sub> in the treated solutions resulted in sporadic small crystals with sizes ranging between 20-180 μm, indicating that scaling formation was relatively minor (Figure 4.15b). As solutions in both systems had similar ionic strength and compositions, and both solutions reached similar average temperatures (65 °C), scaling mitigation is assumed to be a function of the magnetic field according to the proposed fouling mitigation mechanisms. Briefly, the high mobility of Na<sup>+</sup> and Cl<sup>-</sup> ions in the RF magnetic field limits crystal size and prevents them from precipitating and growing on the membrane surface. Instead, multiple smaller crystals are removed at the concentrated stream as a result of shear.

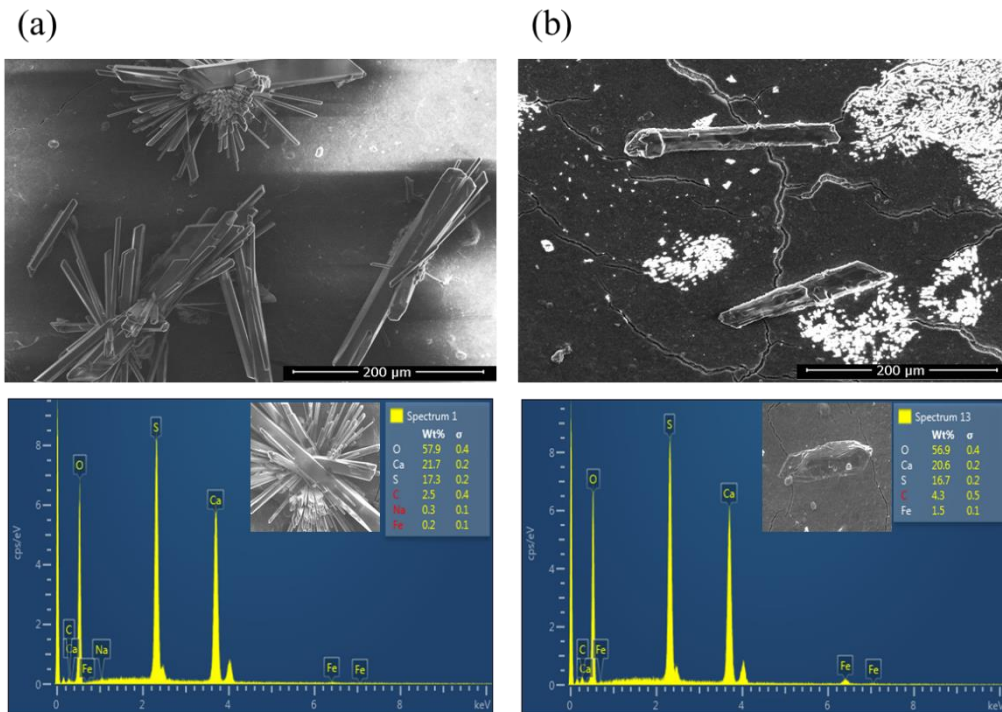


**Figure 4. 15.** EDX and SEM images of membranes surface at 3.6g/L CaSO<sub>4</sub> feed concentration in: (a) C-VMD; (b) RF-VMD systems.

#### 4.2.5 Impact of Feed Flow Velocity on Distillate Flux

Our previous section (4.1) showed that in RF-VMD systems, feed flow velocity impacts the temperature of the solution at the membrane-water interface, as a result of contact time

between liquid and heated membrane (i.e. hydraulic retention time, HRT). Therefore, higher feed velocity resulted in lower solution temperature and lower distillate flux. In addition, flow velocity was hypothesized to impact scaling as the solubility of  $\text{CaSO}_4$  in water decreases with increasing temperature [97]. Moreover, at higher velocities, feed containing ions is exposed to the magnetic field for a shorter time, leading to limited influence of the magnetic field on the mobility and crystallization in the bulk. Therefore, there is a tradeoff between high flow rate and scaling. For a high flow velocity with low HRT, the solution is not heated as required due to the limited contact time between the liquid and the membrane surface. Therefore, low distillate flux is expected. On the other hand, as temperatures are relatively low,  $\text{CaSO}_4$  solubility is higher and there is limited crystallization on the membrane surface. In addition, at short HRTs,  $\text{Na}^+$  and  $\text{Cl}^-$  ions are less impacted by the RF-IH and will do limited damage to the formed crystals in addition to limited impact on water evaporation. At low flow velocities, high solution temperatures are expected at the membrane-solution interface, and therefore, higher distillate flux is expected. However, at higher temperatures,  $\text{CaSO}_4$  solubility decreases, and more scaling is expected. In addition,  $\text{Na}^+$  and  $\text{Cl}^-$  ions are expected to be impacted by the RF-IH magnetic field, thus, ion mobility can damage the formed crystals and decrease the scaling phenomenon.

To validate our hypothesis, the influence of feed flow velocity on  $\text{CaSO}_4$  scaling was assessed at a flow velocity range of 2.33 to 11.25 cm/min, corresponding to flow rates of 1 to 5 ml/min and a residence time of 206 to 43 seconds, respectively. Experiments were done using similar solutions as before (1.8 g/L and 3.6 g/L  $\text{CaSO}_4$  with 35 g/L NaCl). Results revealed that increasing the flow velocity to the extent of 6.75 cm/min, improved

the N.F by 20% and 25% for 1.8 and 3.6 g/L feed concentrations, respectively (Figure 4.16). As expected, at feed velocities lower than 6.75 cm/min (about 3 ml/min), the solution temperature increases to higher values due to the longer membrane-liquid contact time but at the same time, the elevated temperature leads to a decreased  $\text{CaSO}_4$  solubility and increased scaling, even under the influence of RF-IH magnetic fields. Therefore, the overall distillate flux is relatively low. On the other hand, increasing the flow velocity to values higher than 6.75 cm/min led to a decrease in solution temperature due to shorter membrane-liquid contact time, at the same time, the lower temperature limited scaling due to a higher  $\text{CaSO}_4$  solubility. As a result, the overall distillate flux is relatively low. Overall, for RF-VMD systems, high HRT may positively influence the solution's temperature and distillate flux but at the same time have a negative impact on  $\text{CaSO}_4$  solubility. HRT may also influence the mobility of ions, which was shown to impact crystallization and distillate flux. For the assessed RF-VMD system, a maximum distillate flux was obtained at a feed flow velocity of 6.75 cm/min regardless of the  $\text{CaSO}_4$  concentrations.

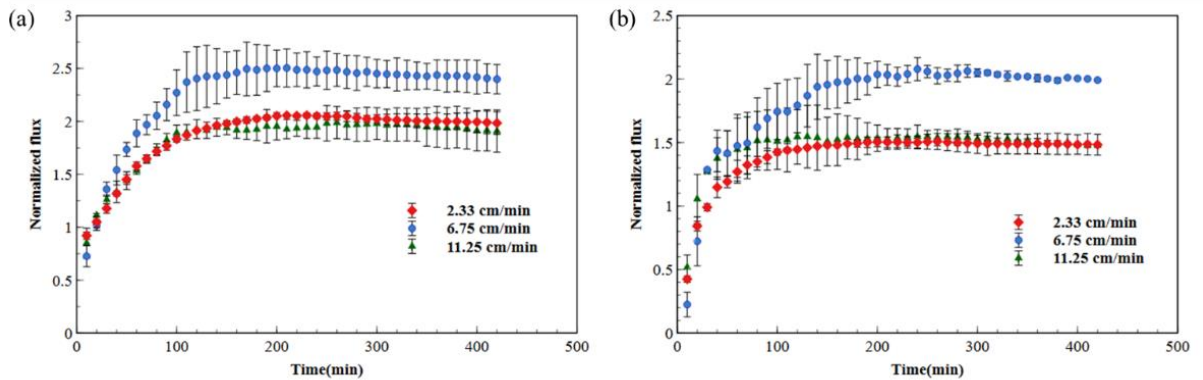


**Figure 4. 16.** Influence of feed flow velocity on the N.F of RF-VMD system at 35 g/L NaCl with (a) 1.8 g/L; (b) 3.6 g/L  $\text{CaSO}_4$  feed solution.

#### 4.2.6 Impact of Concentration Factor on Distillate Flux

As CaSO<sub>4</sub> solubility increases with the increase in ionic strength [239], we evaluated the influence of high salts concentrations on scaling in both systems to assess the influence of the RF-IH. The salt rejection was determined to be high (about 99%) in both systems. Therefore, the concentration factor (CF) was calculated according to Eq. 4.2 [100].

$$CF = \frac{C_f}{C_i} \quad \text{Eq. 4.2}$$

Where C<sub>f</sub> and C<sub>i</sub> are the concentration of both salts in the feed solution with recycled concentrate and the initial feed concentration (g/L), respectively. The values of  $\frac{C_f}{C_i}$  were calculated based on the described ratio in the previous studies [54,99,240], which are based on the ratio of cumulative permeate volume to the initial volume of feed solution (R) at any point. Therefore, we used the defined equation by Martinetti et al. [240] and Hou et al. [99] which is  $CF = \frac{1}{1-R}$  to calculate CF values.

The solubility values (s) were calculated at a range of concentration factors (CFs) and ionic strengths with saturation indexes of 0.7 to 1, according to Eq. 4.3 [241].

$$\log s = \log s^0 + 4S \frac{\sqrt{I}}{1+A_{sp}\sqrt{I}} + \frac{B'}{2} I - \frac{C'}{2} I^2 \quad \text{Eq. 4.3}$$

where I is the ionic strength, which is equal to the molality of (NaCl + 4×molality of CaSO<sub>4</sub>), s is the solubility (mol/L) of CaSO<sub>4</sub> at I, s<sup>0</sup> is the solubility at I=0 (at 65 °C, s<sup>0</sup> = 34.41×10<sup>-6</sup> [241]), S is the limiting Debye-Hückel slope (at 65 °C, S=0.55 [239]). A<sub>sp</sub>, B', and C' are empirical parameters according to temperatures [241], where at 65 °C, A<sub>sp</sub>=1.564, B' = 0, and C' = 0.009.

To evaluate the impact of the RF-IH at higher salt concentrations such as found in concentrated RO brine or produced water and to assess how increased salinity may

influence N.F and scale formation, the concentrate stream was recycled back into the feed tank following MD, thus increasing the ions concentrations in the feed containing 35 g/L NaCl with/without 1.8 g/L CaSO<sub>4</sub>. Results of previous studies [54,239] and our calculated values (Figure 4.17a) show that increasing the ionic strength to the extent of about 1.5M (corresponding to a CF of about 2) increases CaSO<sub>4</sub> solubility, while higher ionic strengths lead to lower solubility or have limited effect. Figure 4.17b addresses these values by displaying the CaSO<sub>4</sub> concentrations and corresponding solubility values at different CFs. For C-MD, the decrease in N.F can be correlated with an increase in CF (Figure 4.17c) and attributed to the CaSO<sub>4</sub> scaling and decrease in partial vapor pressure [93]. Lower N.F values of salt solutions containing NaCl in the absence of CaSO<sub>4</sub> are only associated with the lower partial vapor pressure (i.e., driving force) because of the high NaCl concentration [93], whereas in the presence of CaSO<sub>4</sub>, the decrease of N.F can be a result of both lower vapor pressure and scaling at the membrane surface. At CF below 2, both feed solutions (with and without CaSO<sub>4</sub>) had a similar N.F decrease trend (Figure 4.17c) while in the presence of CaSO<sub>4</sub> the N.F is 10% lower. The difference is attributed to the decrease in partial vapor pressure due to the additional CaSO<sub>4</sub> ions. At these CF values, the ionic strength is lower than 1.5 mol/L (as shown in figure 4.17a) and the concentration of CaSO<sub>4</sub> in the feed solution is lower than the saturated solubility (Figure 4.17b), leading to limited or no crystallization. At higher CF values (above CF of 3), the solution is above the solubility limit of CaSO<sub>4</sub>, leading to 20% more flux reduction in comparison to the solution containing only NaCl. This is hypothesized to be a result of scaling on the membrane surface. The influence of CaSO<sub>4</sub> scaling and supersaturation can be seen in CF values between two and four, resulting in 55% flux reduction in comparison to the solution

containing only NaCl which suffered from 40 % flux reduction. Our results are consistent with data from the literature[54]. Ju et al. showed that an increase in ionic strength to more than 1.5mol/L (corresponding to the CF more than 3.5 ) led to CaSO<sub>4</sub> scaling [54]. As expected, SEM imaging of the membrane following C-VMD with CaSO<sub>4</sub> at CF=4 exhibited very large CaSO<sub>4</sub> crystals (with sizes ranging between 300-950 μm) on the membrane surface (Figure 4.17c). The large crystals and scaling layer on the membrane surface can also increase the concentration boundary layer resistance on the membrane surface in addition to blocking the membrane pores to prevent vapor transport, leading to a notable decrease in the N.F [37].

In contrast, for the RF-VMD system, high-frequency magnetic fields increased N.F values as previously shown; this is especially seen when the solution contains high salinity without CaSO<sub>4</sub>. Therefore, distillate flux was shown to increase with the increase in CF (Figure 4.17d) and the N.F reached values of about 400% when the solution was concentrated four times (i.e., CF of four). This phenomenon was hypothesized to be a result of the high-frequency vibration of Na<sup>+</sup> and Cl<sup>-</sup> ions, leading to a decrease in water molecules' bonds [218] as previously discussed. In contrast to C-VMD, where CaSO<sub>4</sub> ions in the feed led to a decrease in distillate flux due to scaling, the RF-IH process was shown to mitigate membrane scaling, leading to constant and stabilized N.F over time (Figure 4.14b). A decrease of about 40% in N.F was measured for solutions with CaSO<sub>4</sub> in comparison to the solution containing only NaCl at high CF due to the negative impact of Ca<sup>+2</sup> and SO<sub>4</sub><sup>-2</sup> ions. Interestingly, even at CF larger than two, the reduced value of N.F for feed solutions with CaSO<sub>4</sub> is approximately constant, inferring that the ionic strength has a negligible impact on scaling procedure under the influence of an RF-IH magnetic field. SEM images

of the membranes following RF-VMD experiments with  $\text{CaSO}_4$  solutions (at  $\text{CF}=4$ ) show that although some  $\text{CaSO}_4$  crystals can be detected at the membrane surface, they are relatively small ( $<100\ \mu\text{m}$ ) and limited in number (Figure 4.17d).

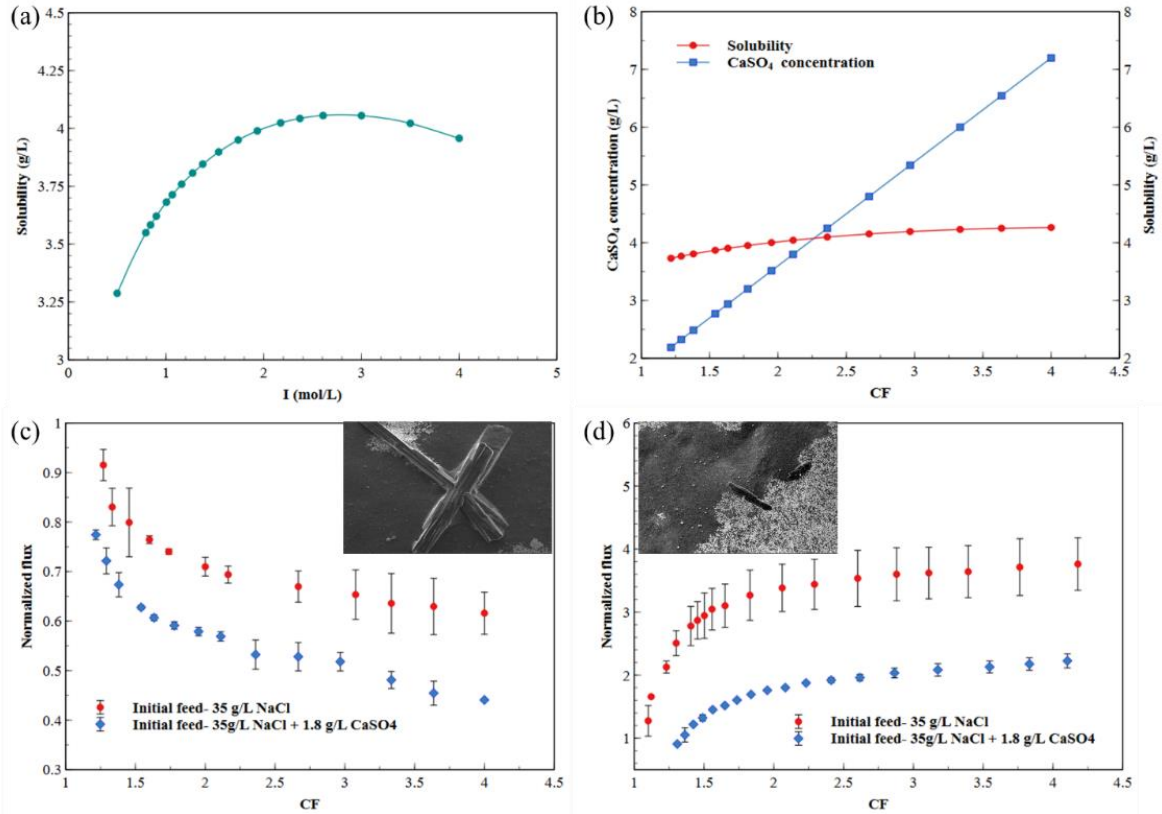


**Figure 4. 17.** (a) Impact of ionic strength on the  $\text{CaSO}_4$  solubility; (b) Impact of CF on the solubility and concentration of  $\text{CaSO}_4$ ; (c) Impact of CF on N.F of C-VMD and SEM image of membrane surface at  $\text{CF}=4$  in the C-VMD; (d) Impact of CF on N.F of RF-VMD and SEM image of membrane surface at  $\text{CF}=4$  in the RF-VMD.

#### 4.2.7. Treatment and Scaling behavior of Simulated RO Brine

Assessing scaling mitigation of RO brines is gaining interest as RO is currently the most common desalination approach and there is a growing understanding of the need for RO brine management. We used a synthetic solution containing 35 g/L NaCl, 1.80 g/L  $\text{CaSO}_4$ , 2.91 g/L  $\text{MgSO}_4$ , 4.52 g/L  $\text{MgCl}_2$ , and 1.03 g/L KCl, with a total salinity of 46.5 g/L to simulate RO brine according to Ge et al[54]. Similar values were used for describing RO

brine in the literature [37,238]. The RF-IH magnetic field is assumed to influence RO brine solutions containing multiple ions in addition to  $\text{Na}^+$ ,  $\text{Cl}^-$ ,  $\text{Ca}^{+2}$ , and  $\text{SO}_4^{-2}$ . Figure 4.18a presents N.F values of synthetic RO in comparison to saline solutions with/without  $\text{CaSO}_4$ . Results indicate that the N.F values of the RO brine are relatively similar to the solution containing only  $\text{NaCl}$ , while a solution containing  $\text{Na}^+$ ,  $\text{Cl}^-$  and  $\text{CaSO}_4$  have lower N.F values. Accordingly, ions that will not contribute to precipitants formation, including additional  $\text{K}^+$ ,  $\text{Cl}^-$ , and  $\text{Mg}^+$  may enhance the distillate flux by a similar mechanism as described for  $\text{Na}^+$  and  $\text{Cl}^-$  ions. Among all existent salts in the RO brine solution, the tendency of  $\text{CaSO}_4$  to crystallize and form scaling is the highest as its solubility in water is very low. At 25 °C, the saturation solubility of  $\text{KCl}$ ,  $\text{MgCl}_2$ ,  $\text{MgSO}_4$ , and  $\text{NaCl}$  in the water are 350.5, 540.6, 360, and 358.9 g/L, respectively, which are much higher than the solubility concentration of  $\text{CaSO}_4$  (2.4 g/L). As previously explained, we have not addressed calcium carbonate fouling as it was shown to form scaling prior to the MD process, mainly by precipitation on heat exchangers and pipes [53]. In addition, the solubility of all salts in RO brine (except  $\text{CaSO}_4$  and  $\text{CaCO}_3$ ) increases with the increase in temperature. Therefore, exposure and direct heating of RO brine by RF-IH is assumed to mainly form  $\text{CaSO}_4$  crystals. Furthermore, additional ions such as  $\text{K}^+$ ,  $\text{Cl}^-$ ,  $\text{Na}^+$ , and  $\text{Mg}^{2+}$  may have increased mobility under the RF-IH field and therefore may lead to higher distillate flux value and physical breakdown of existing  $\text{CaSO}_4$  crystals. Images of the membrane following RF-VMD using RO brines solutions (Figure 4.18b), revealed limited sporadic small  $\text{CaSO}_4$  crystals.

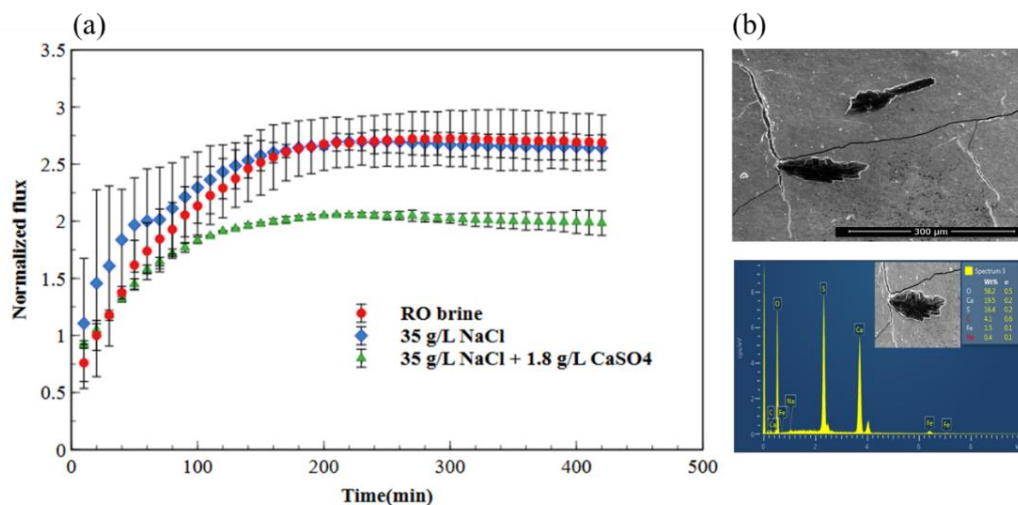


**Figure 4. 18.** (a) Impact of RF-VMD on N.F of RO brine compared to saline solutions with and without CaSO<sub>4</sub>; (b) EDX and SEM images of membranes surface of RO brine in RF-VMD system.

#### 4.2.8 Conclusions

CaSO<sub>4</sub> scaling formation and mitigation were assessed in the RF-VMD system using thermally conducting membranes modified by carbon nanotubes functionalized with magnetic iron nanoparticles. In contrast to C-VMD, where CaSO<sub>4</sub> crystallization and fouling led to a decrease in distillate flux, RF-VMD showed limited fouling and no flux decline. Membrane analysis following distillation showed only sporadic small CaSO<sub>4</sub> crystals on the membrane surface, even when treating solutions with high ionic strength. Furthermore, high concentrations of small crystals were detected at the concentrate stream, indicating limited deposition on the membrane surface. In addition, the presence of additional ions typically found in concentrated RO brine leads to enhanced distillate flux and limited scaling. The influence of different ions was assessed, showing a decrease in distillate flux as a function of CaSO<sub>4</sub> concentration and an increase in distillate flux as a result of increased Na<sup>+</sup> and Cl<sup>-</sup> ions. Results are attributed to the RF-IH magnetic fields used for directly heating the membrane surface, leading to high mobility and collision of

ions as a result of Lorentz force. These are hypothesized to enhance distillation flux and diminish scaling by weakening intermolecular water bonds and damaging the formed  $\text{CaSO}_4$  crystals. The RF-VMD system was also assessed as a function of feed flow velocity, showing optimized results at low-velocity values (6.75 cm/min).

### **4.3 Enhanced Performance of Membrane Distillation using Radio-Frequency Induction Heated Thermally Conducting Feed Spacers**

**Preface:** The contents of this section are in part based on a published article in Journal of Separation and Purification Technology: **Anvari, A., Yancheshme, A.A., Ronen, A.,** "Enhanced Performance of Membrane Distillation using Radio-Frequency Induction Heated Thermally Conducting Feed Spacers", Separation and Purification Technology 250 (2020): 117276 [196].

#### **4.3.1 Introduction**

The self-heated membranes including Joule, solar, and radio frequency (RF) heated MD systems (previous sections) were shown efficient when treating saline water as they directly heat the water near the membrane surface, leading to decrease TP over the membrane length and relatively high distillate flux in comparison to CMD systems at similar conditions. However, to date, self-heating MD systems were shown efficient only at low feed flow velocities in the range of 0.2-9 cm/min (i.e., 9 cm/min for Joule heating [188], 2.3 cm/min for RF heating (previous sections), and 0.19 cm/min for solar heated MD systems[178]), as a long contact time is required between the liquid and the heating element. Consequently, low flow velocities were shown to hinder local mixing and increase CP, thus, leading to limited distillate flux in the range of 0.5-7.5  $\text{kg/m}^2\cdot\text{h}$  [178,188,194].

Therefore, the goal of this section is to develop a proof-of-concept for a self-heated MD approach based on feed spacers that is able to reduce TP at relatively high flow velocities (100-300 cm/min), thus, coupling heating and mixing. We addressed this by developing a vacuum membrane distillation (VMD) system that includes thermally conducting feed spacers. The thermally conducting spacers are heated in-situ by radio-frequency electromagnetic fields.

In this research, inert commercial polypropylene (PP) feed spacers were exchanged with stainless-steel (SS) spacers (Figure 4.19) and these were used to directly heat the feed solution near the membrane surface instead of preheating the bulk feed solution. Feed spacers were shown to reduce CP in CMD systems at flow velocities in the range of 60-850 cm/min by increasing the mixing near the membrane's surface [85,151,152,154–156,162,163]. Similar to self-heated membranes [178,188,194], the RF heated feed spacers are assumed to increase the solution's temperature near the membrane surface and reduce TP while also promoting local mixing. An illustration of the VMD process using RF heated spacers is presented in Figure 4.19.

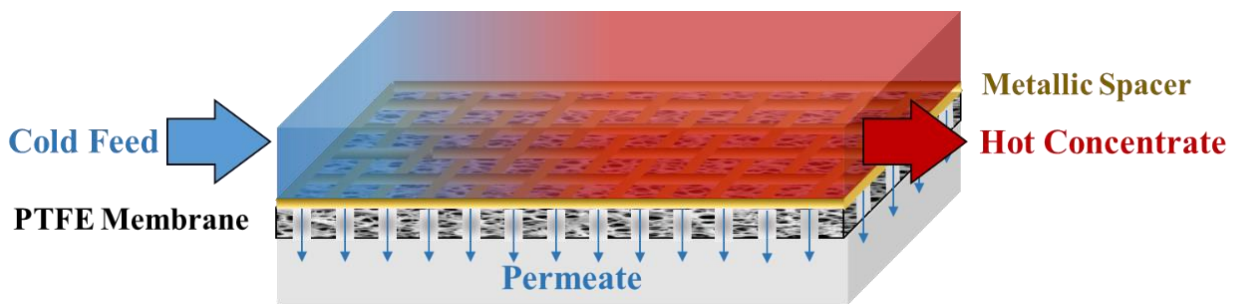


**Figure 4. 19.** Schematic diagram of the RF heated MD process. Bottom layer: vacuum chamber; Middle layer: membrane-feed spacer interface; Top: feed solution and temperature profile (red: hot; blue: cold).

### 4.3.2 SS Spacer Heating at Static Conditions

To evaluate the heating rate of the SS spacers and to calculate the energy required for heating (i.e., workpiece power), the spacer was exposed to RF heating at varying power ( $P_c$ ) values. The average temperature of the spacer, at  $P_c$  of 60W to 90W, was obtained using IR thermal imaging (Figure 4.20a, Table 4.3). As the thermal stabilities of the polymeric membrane (PTFE,  $T_g=126\text{ }^\circ\text{C}$ ) and filtration module (thermally resistant Nylon sheets with high thermal stability of  $\sim 110\text{ }^\circ\text{C}$ ) are limited, measurements in static conditions (exposed to air) were restricted to a short duration of 5 seconds as the elevated temperatures reached could impact the integrity of the system. All measurements were triplicated and the temperature at the spacer's surface ( $T_{fs}$ ) was averaged accordingly (as discussed in Section 3.11).

As eddy currents are not uniformly distributed [203,204], the heating is non-uniform along the spacer's length and width, leading to an uneven spatial temperature distribution [204]. The nonuniform heating pattern depends on the material properties, applied frequency, and ratio of coil and workpiece length and orientation [203,204]. Accordingly, the IR thermal imaging (Figure 4.20a) shows that the temperature profile along the SS spacer is not constant, with faster heating and higher temperatures along the spacer's edges. Numerical simulation was used to verify the IR measurement of the spacer's surface temperature. The simulation results (Figure 4.20b) show an average surface temperature of  $47.36\text{ }^\circ\text{C}$  for a 60 W power which is in agreement with IR image ( $46.82\text{ }^\circ\text{C}$ ) as shown in Figure 4.20a and Table 4.3. The experimental results and numerical simulation also show a similar temperature distribution pattern (Figure 4.20 a, b). Accordingly, the workpiece power ( $P_w$ ) was calculated (using Eq. 3.6) as 3.57W to 5.65W (for  $P_c$  of 60W to 90W) which are

proportional to 1.12 to 1.77 kW/m<sup>2</sup>, respectively. These values are also in agreement with the numerical simulations (i.e., 1.205 kW/m<sup>2</sup> for P<sub>c</sub> of 60W).

**Table 4. 3.** Averaged temperatures and heating rates of S1 spacer according to P<sub>c</sub> values.

P <sub>c</sub> (W)	Average T <sub>fs</sub> (°C)	Heating rate (°C/s)	P <sub>w</sub> (W)
<b>60</b>	46.82±3	4.76±0.6	3.57
<b>70</b>	50.83±0.8	5.57±0.2	4.17
<b>80</b>	56.68±1	6.7±0.2	5.03
<b>90</b>	60.68±4	7.53±0.8	5.65

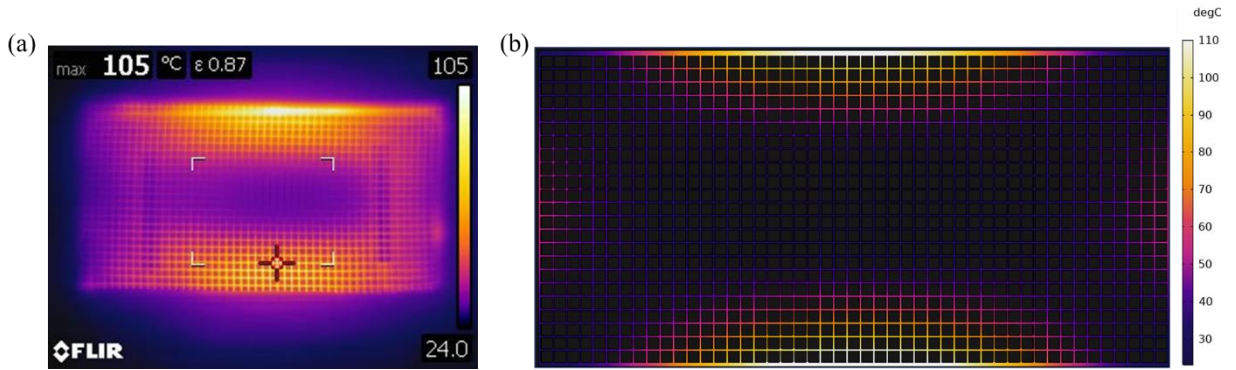


**Figure 4. 20.** (a) IR thermal image of the heated SS feed spacer (P<sub>c</sub> of 60W); (b) Numerical simulation of the temperature profile of the RF heated SS feed spacer at similar conditions. The temperature scale is in °C units.

### 4.3.3 SS Spacer Heating in Flow Conditions

To evaluate the influence of RF heated SS spacers on the performance of the VMD process, experiments were conducted using a ‘cold’ feed solution at room temperature without prior heating. Under flow condition, heat was transferred from the heated spacer to the cold feed solution, thus preventing overheating of the module. IR thermal imaging of the feed solution and SS spacer prior to heating (Figure 4.21a) showed approximately similar temperatures (19-23 °C) for the SS spacer and the surrounding liquid.

Following 30 seconds of RF heating at  $P_c$  of 60W and a low flow velocity (1 cm/min), both the solution-filled channel and the spacer exhibited a significant increase in temperature, reaching 60-90 °C (Figure 4.21b). Due to technical limitations, IR imaging was not possible at higher flow velocities but numerical simulation of the feed solution and cross-section temperature distribution (Figure 4.21 c, d) were used to show the temperature distribution along the feed channel at higher flow velocity (50 cm/min). The simulations were done with an inlet solution at a temperature of 23 °C. Cross-section of the temperature profiles were calculated at three positions at y-axis, centerline ( $y=0$  cm), middle ( $y=1$ cm), and edge ( $y=2$ cm) and along the x-axis (total length of 8 cm). Results show a continuous increase in the solution's temperature along the length of the membrane as a result of the contact between the solution and heated SS spacer. Furthermore, according to the non-uniform heating pattern of RF-IH (as presented in Figure 4.20), higher temperatures were seen near the membrane's edge ( $y=1-2$  cm). As the simulations were done in a small-scale system, similar to the dimensions of the experimental system, the temperature profiles presented are not fully developed and are expected to become homogeneous in a longer distillation module as previously shown for RF heated membranes [194].

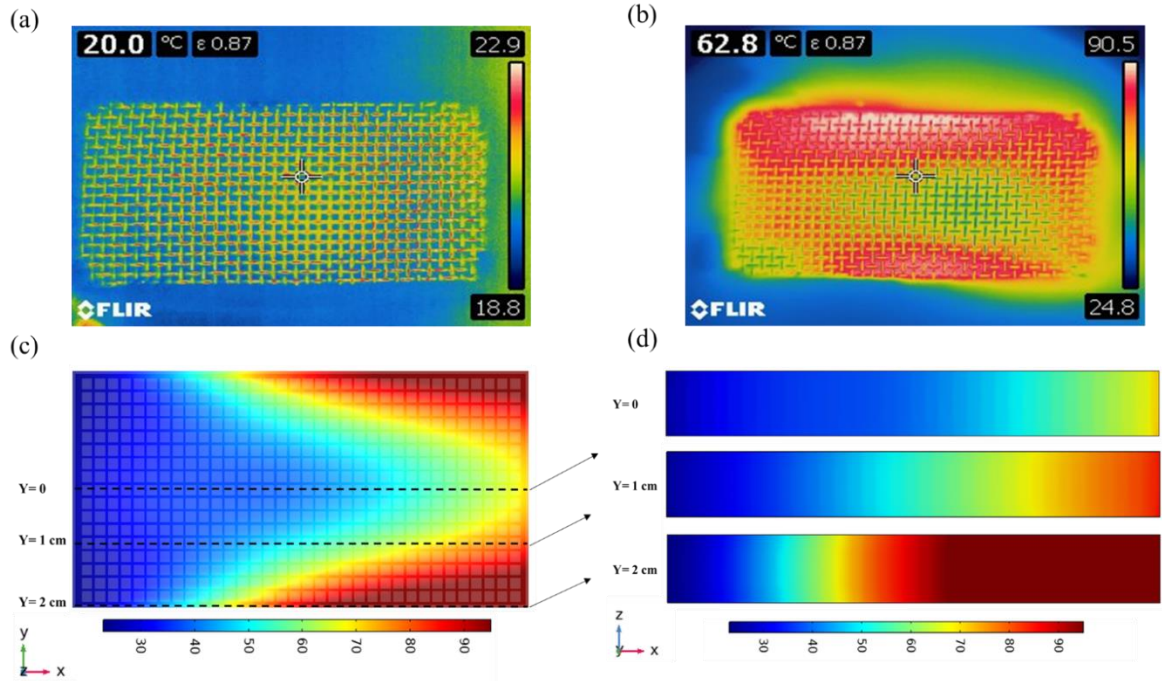


**Figure 4. 21.** IR thermal images of SS spacer and the feed solution in the flow module: (a) Initial conditions; (b) Following 30 seconds of RF heating; Numerical simulation of temperature profile of the RF-heated SS spacer and the feed solution in the flow module: (c) top view; (d) cross-section. Temperature scale is in °C units.

#### 4.3.4 Parametric Evaluation of Operating Conditions on Distillation Flux

##### 4.3.4.1 Vacuum Level

Vacuum level has a significant influence on distillate flux and selectivity in VMD systems. Therefore, the RF-VMD system was optimized in terms of distillate flux and salt rejection according to the applied vacuum level (i.e., 10-30 kPa under constant flow velocity of 50 cm/min and  $P_c$  of 60 W).

The transmembrane mass flux ( $N_v$ ) is dependent on the difference of water vapor pressure across the membrane [148] ( $\Delta P = P_{fm} - P_{vacuum}$ ) as described in Eq. 4.4 [215]:

$$N_v = K_m A \Delta P \quad \text{Eq. 4.4}$$

Where  $K_m$ ,  $P_{fm}$ , and  $A$  are membrane mass transfer coefficient, water vapor partial pressure at membrane surface in the feed side, and the surface area [215,242]. Therefore, a higher

vacuum level increases  $\Delta P$ , leading to higher distillate flux. Results (Figure 4.22a) and the related literature [148,194,215] show that the distillate flux increases linearly with the increase in vacuum level. While higher vacuum level leads to higher distillate flux, it may lead to a decrease in selectivity as a result of pore wetting at local pressures exceeding the liquid entry pressure [148]. In the evaluated VMD system, rejection was higher than 99% until a vacuum level of 20 kPa. Therefore, according to the distillate flux (Figure 4.22a) and the obtained membrane selectivity, an optimal working pressure of 20 kPa was selected for all following experiments.

#### **4.3.4.2 Feed Flow Velocity**

While for CMD systems, increasing the flow velocity of the heated feed solution was shown to increase distillate flux [142,160], for self-heating MD systems, high flow velocity of the cold feed solution was shown to decrease distillate flux [188,194] as a result of the limited liquid-heated element contact time. Higher feed flow velocity was also shown to increase the overall energy requirement, as pumping energy requirement may reach up to 10 % of the overall energy [232,243], in addition to buildup of internal pressure in the flow channel, resulting in lower salt rejection [148]. Therefore, typical flow velocities were shown to be in the range of 50-3600 cm/min for CMD systems [21,25,151,154,157] and 0.2-9 cm/min in self-heated MD systems including our previous sections [178,188,194].

The influence of feed flow velocity on distillate flux was evaluated at a 28.5 to 300 cm/min flow velocity range while maintaining all other parameters constant (i.e., feed concentration of 35 g/L NaCl, vacuum pressure of 20 kPa, and  $P_c$  of 60 W). The selected flow rate is in the low CMD range [21,25,151,154,157] and significantly above the highest flow rate described for self-heated systems [178,188,194] and was selected to allow

internal mixing near the membranes while giving the solution and heated spacer adequate contact time.

Results (Figure 4.22b) show that lower flow velocity and a longer residence time led to higher distillate flux. For example, distillate flux increased from 0.5 to 5.5 kg/m<sup>2</sup>.h by reducing the feed flow velocity from 300 to 28.5 cm/min and therefore increasing the liquid-spacer contact time from 2 to about 17 seconds. Overall, distillate flux values obtained by the RF-VMD configuration are comparatively higher than values obtained by conventional VMD (C-VMD) systems with and without spacer, even at high flow velocities. In addition, for RF-VMD, flux values corresponding to low velocities are much higher in comparison to values of C-VMD systems (Section 4.3.6). Furthermore, the obtained distillate flux was high in comparison to previously studied self-heating MD systems [178,188,194], even when assessed at velocities up to 30-100 times higher than the flow velocities used in other self-heated MD systems (Section 4.3.7). The high distillate flux at high feed flow velocities is assumed to be a result of the relatively fast RF heating rate as addressed in section 4.3.4.3 and the internal mixing by the spacers.

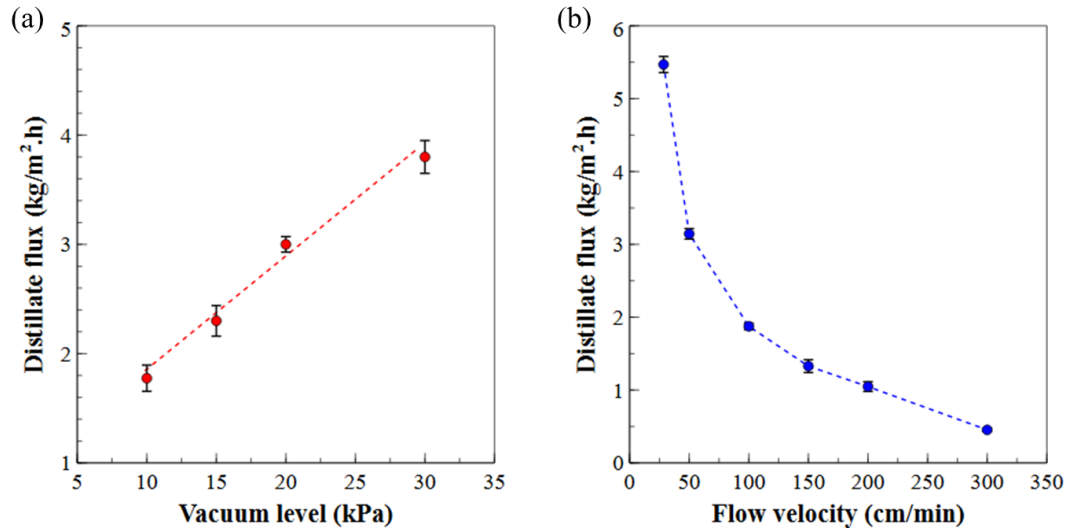


**Figure 4. 22.** (a) Impact of vacuum level on distillate flux of the SS spacer in RF heated based VMD, at 50 cm/min feed flow velocity and  $P_c$  of 60 W; (b) Impact of feed flow velocity on distillate flux of the SS spacer in RF heated based VMD, at 20 kPa vacuum pressure and  $P_c$  of 60 W.

#### 4.3.4.3 Required Power to Heat SS Spacers ( $P_w$ )

In addition to controlling the feed flow velocity, enhancing the RF-MD distillate flux can be controlled by increasing the RF heating rate while keeping flow parameter constant. This was experimentally assessed by varying the energy input to the SS spacer, ranging from 3.57 to 5.65W ( $P_c$  of 60W to 90 W) which are corresponding to 1.12 to 1.77 kW/m<sup>2</sup>. Accordingly, distillate flux was measured at three relatively high feed flow velocities (100-300 cm/min). Results show a linear relationship between the supplied power to the spacer and distillate flux for all flow velocities (Figure 4.23a) as higher power resulted in elevated membrane-spacer interface temperature. Even for a high flow velocity of 300 cm/min, distillate flux was increased by about 300% as a result of increasing the power from 1.12 kW/m<sup>2</sup> to 1.77 kW/m<sup>2</sup> (a 60% increase). Furthermore, increasing the supplied power has a relatively low impact on specific heating energy at lower flow velocities in the range of 100-200 cm/min (Figure 4.23b), resulting in approximately constant values (i.e.,  $0.63 \pm 0.04$

kWh/m<sup>2</sup> for 100 cm/min and 1±0.08 kWh/m<sup>2</sup> for 200 cm/min). For higher flow velocity in the range of 300 cm/min, the specific heating energy decreases with the increase of input power as a result of the high distillate flux obtained (Figure 4.23b). These results confirm that for RF heated MD systems, higher input power may result in a constant or even reduction in specific heating energy as the produced distillate flux is high enough to compensate on the excess amount of consumed heating energy.

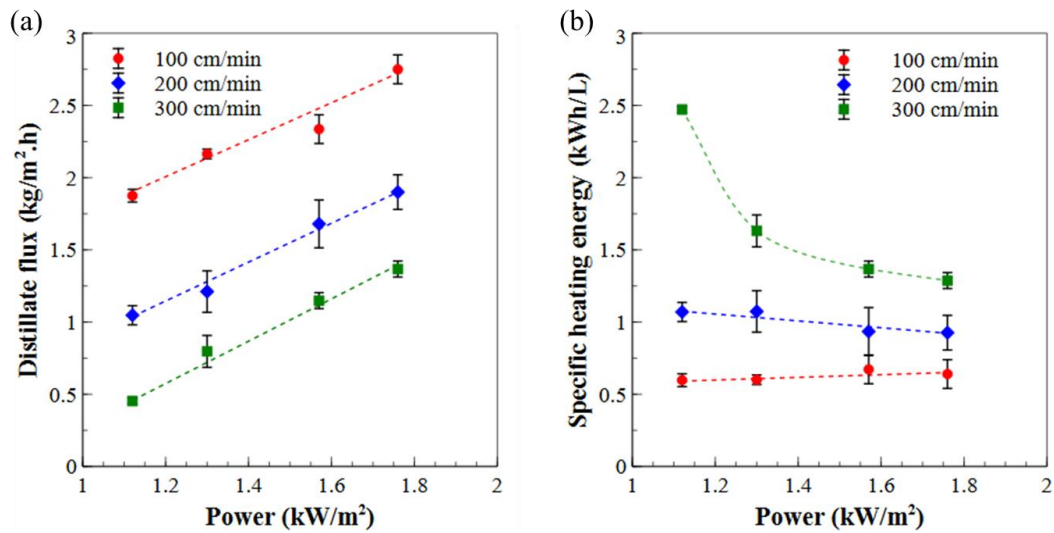


**Figure 4. 23.** (a) Impact of  $P_w$  on distillate flux of SS spacer in RF-IH based VMD, at 20 kPa vacuum pressure. (b) Impact of  $P_w$  on specific heating energy of SS spacer in RF-IH based VMD, at 20 kPa vacuum pressure.

#### 4.3.5 Optimization of Spacer’s Physical Properties and Impact of Orientation

To assess the impact of spacer’s physical properties (i.e. mass and dimensions) and orientation on the efficiency of RF heating and distillate flux, four SS spacers with different physical properties (Table 4.4 and Figure 3.1) were evaluated. Generally, the efficiency of RF heating is influenced by the mass and composition of the heated element (Eq. 3.6), therefore an element with a higher mass and high thermal and magnetic properties should heat better and faster than a non-metallic/non-magnetic component with similar geometric

properties [203,209,244]. As previously mentioned, SS spacers are commercial products, and therefore it is difficult to decouple their mass and structure properties. To compare properties, SS spacers were divided into two groups with relatively similar masses and mesh diameters per group (1.5-1.85 gr for S1, S2 and 3.7-3.87 gr for S3, S4). Within each group, spacers had different geometric parameters including filament distances (H), surface area, and porosity. In addition, spacer's orientation ( $\alpha$ ) was evaluated at two conditions, where  $\alpha=45^\circ$  and  $90^\circ$  (Figure 3.3b, Table 4.4).

**Table 4. 4.** Geometric characteristics of assessed feed spacers.

<b>Spacer</b>	<b>Material</b>	<b>Mesh mass (gr)</b>	<b>H (mm)</b>	<b>D (<math>\mu\text{m}</math>)</b>	<b>Surface area (<math>\text{cm}^2</math>)</b>	<b>Porosity (%)</b>
<b>S1</b>	Stainless Steel	1.5	1.45	245	27.7	73
<b>S2</b>	Stainless Steel	1.85	1.04	229	35.7	67
<b>S3</b>	Stainless Steel	3.7	0.92	356	54.1	52
<b>S4</b>	Stainless Steel	3.87	1.85	457	37.3	64
<b>PP</b>	Polypropylene	0.22	2.03	483	37	65

Results (Figure 4.24a) demonstrate the impact of the spacer's mass on the heating process, as RF heating is a function of the heated element mass (according to Eq. 3.6). Accordingly, spacers with higher mass (e.g., S3 and S4 spacers) produced more heat at the same applied power and duration, thus, resulting in higher temperatures near the membrane surface and significantly higher distillate flux in comparison to SS spacers with a lower mass (e.g., S1 and S2 spacers).

Spacer's filament opening size (H) was also shown to influence the distillate flux. While for PP spacers, distillate flux increased with the decrease in the spacer density, expressed as the decrease in filament distances [156], a contrasting result was seen for SS spacers as

a higher distillate flux was measured for spacers with larger H values. This trend can be seen within each spacer group, where S1 has higher flux than S2 and S4 has higher flux than S3 (Figure 4.24a). This is assumed to be a result of improved mixing of the heated solution and improved heat transfer within the spacer open areas. Furthermore, while spacer orientation ( $\alpha$ ) was shown to significantly impact distillate flux in CMD systems, leading to an increase of the heat transfer coefficient by up to two times at  $\alpha=45^\circ$  [152,155], changing RF heated SS spacers orientation to  $45^\circ$  resulted in a relatively minor impact on distillate flux (an increase of up to 1.5 times) in comparison to the impact of spacer's mass (an increase of up to 9 times) (Figure 4.24b).

Furthermore, for the assessed configuration, the surface area of the spacers (Table 4.4) had no specific influence on distillate flux. Comparison between spacer groups (i.e., S1 and S2 with S3 and S4 as shown in Figure 4.24a,) showed that the highest distillate flux was obtained for spacers with the highest surface area and highest mass (i.e., S3 and S4). However, comparing spacers with relatively similar mass and varying surface area, led to the conclusion that a higher surface area does not result in higher distillate flux. Therefore, high distillate flux as a result of RF heating is related to the spacer's mass. It should be noted that for our experimental conditions, spacers surface area differences are not significant and may result on about 50-100% difference. Longer module with more significant differences between the spacer's surface area might show different behavior as higher surface area will have higher heat transfer with the surrounding water. Overall, the highest distillate flux (i.e., 5-12 kg/m<sup>2</sup>.h for flow velocities of 100-300 cm/min) was obtained for S4 SS spacers having the highest mass.

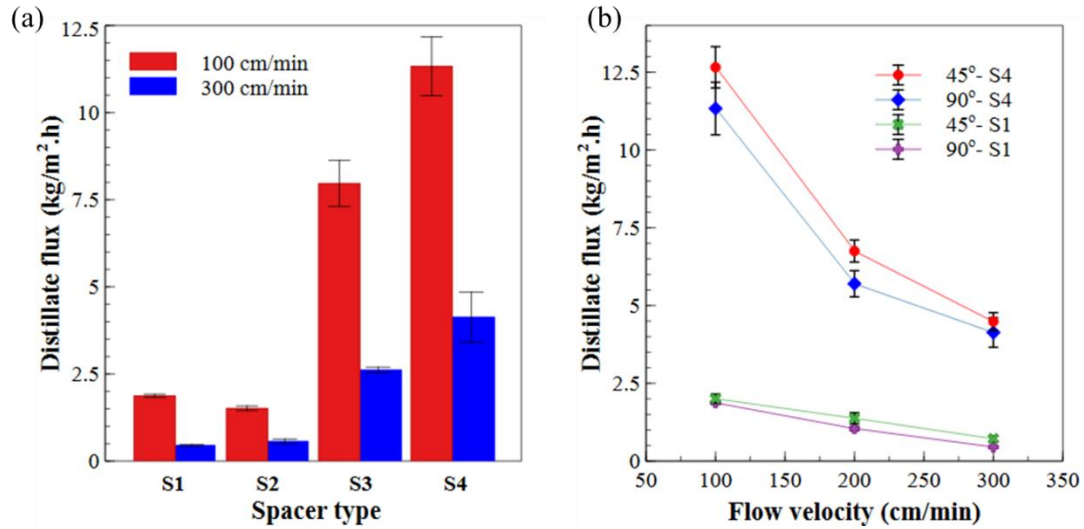


**Figure 4. 24.** (a) Distillate flux of SS spacers in RF-VMD as a function of feed flow velocity; (b) Distillate flux of S1 and S4 spacers with 45° and 90° spacer filament orientations as a function of feed flow velocity.

#### 4.3.6 Comparison of RF Heated SS Spacers with Conventional MD System

The tested system was compared to a C-VMD system in order to evaluate its feasibility. This includes testing the C-VMD system with and without a PP spacer and using SS spacers without RF heating. According to the previously obtained data, all further experiments were done using an S4 SS spacer due to its ability to produce a relatively high distillate flux in RF-VMD system. Both systems were evaluated at similar operating conditions (i.e., feed solution containing 35 g/L NaCl, feed velocity of 100 and 300 cm/min, and vacuum pressure of 20 kPa) with difference related only to the feed temperature and heating approach. The feed to the RF-VMD system was at room temperature ( $20 \pm 3$  °C) with constant applied power ( $P_c = 60$  W), while the feed to the C-VMD system was preheated to  $55 \pm 3$  °C with an input heating energy of 95-285 W depending on the feed flow velocity (i.e., 100-300 cm/min, respectively). The C-VMD inlet temperature was selected based on the local maximum temperature of the RF heated system, acquired using COMSOL

simulation, to maintain an initial similar driving force for both systems. Both systems were assessed at continuous mode without recirculation.

Results show that in the C-VMD system, the presence of the PP spacer slightly increased the distillate flux in comparison to a similar system without a feed spacer (Figure 4.25a). Distillate flux values obtained in the C-VMD system with the PP spacer at flow velocity of 100 cm/min are in the range of 1.5-2 kg/m<sup>2</sup>.h as a result of the relatively low feed flow velocity [160]. Replacing the PP spacer with the SS spacer at similar feed conditions without RF heating resulted in a higher distillate flux (up to 3 kg/m<sup>2</sup>.h). As both spacers (PP and S4) have similar geometric properties, the increase in flux is a result of a better heat distribution along the membrane module, leading to a decrease in TP. A similar result was shown by Tan et al.[166], using metallic spacers. Finally, applying 60 W of RF heating resulted in a significant increase in distillate flux, reaching 11-12 kg/m<sup>2</sup>.h which is about seven times higher than the distillate flux obtained in the C-VMD system with a PP spacer at the same temperatures and flow conditions (100 cm/min). As expected for the thermally conducting spacers heated by RF (RF-S4 spacer), reducing the feed flow velocity resulted in an increase in distillate flux (Figure 4.25a), while an opposite behavior was demonstrated for all spacers in the C-VMD system.

The high flux in the RF-VMD system is attributed to the negligible TP (TPC > 1) as a result of heating the feed solution by the RF heated SS spacer along the membrane length. This was confirmed by numerical simulation to obtain the average temperature at the membrane's surface ( $\bar{T}_{fm}$ ) and calculate TPC values along the membrane length. Results show that TPC values increase along the RF heated flow channel, indicating that the average temperature along the membrane is higher than the bulk feed temperature ( $\bar{T}_{fm} >$

$\bar{T}_f$ , Figure 4.25b). Similar results were shown for other self-heating membranes based on Joule and RF heating [188,194], resulting in an increase in TPC and reduced TP along the length of the heated element.

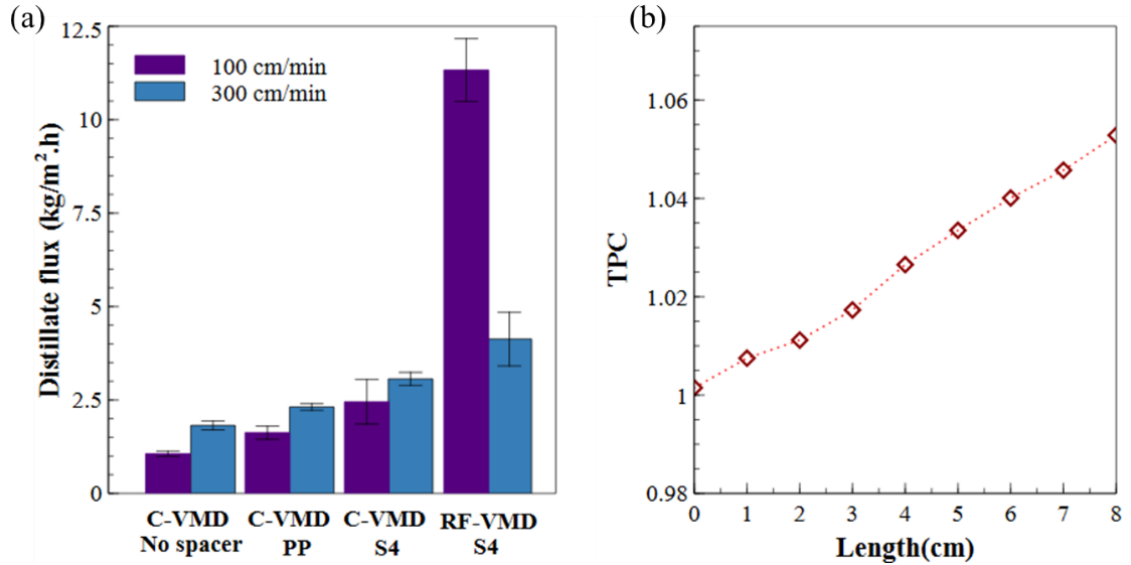


**Figure 4. 25.** (a) Distillate flux of C-VMD with and without PP and S4 spacers in comparison to the RF heated VMD system with S4 spacer at flow velocities of 100 and 300 cm/min.; (b) Numerical simulation results of TPC along the membrane length in the RF heated MD system.

#### 4.3.7 Comparison with Self-heated MD Systems

The RF heated MD system with S4 spacer was compared to novel self-heated MD systems in terms of distillate flux and specific heating energy. The assessed self-heating MD systems are based on direct heating of the membrane surface by Joule, solar, and RF heating (our previous sections) [178,188,194]. It should be noted that most of self-heating MD systems operate at low flow rates to provide adequate contact time and heat transfer between the heated element and the feed solution, e.g., Joule heating was tested at 9 cm/min [188], RF heating at 2.33 cm/min (our previous sections) [194], and solar heating at 0.192 cm/min [178]. While distillate flux increases as a result of direct membrane heating at low

flow velocity, the limited mixing near the membrane surface may lead to limiting phenomena as CP. Therefore, to mitigate CP while directly heating the SS spacers, the experimental system was evaluated at relatively high feed flow velocities of about 100 cm/min which are in the lower range of CMD systems. Results show that even at high flow velocities, the distillate flux values were in the range of 11-12 kg/m<sup>2</sup>.h which are relatively high in comparison to other self-heated MD systems (Figure 4.26).

Furthermore, energy calculations based on the experimental work show that the tested system obtained high GOR and low specific heating energy values (GOR of 2.1 and specific heating energy of 0.32 kWh/L at feed velocity of 100 cm/min) in comparison to other self-heated systems (e.g., GOR values of 0.54 and 0.48 in addition to the specific heating energy values of 1.23 and 1.4 kWh/L for Joule and solar-heated MD systems, respectively [178,188]). Specific heating energy values reported by other conventional [191,220,221] and self-heated MD systems [178,188,193,222] are generally also higher (Figure 4.26). The relatively high distillate flux and low specific heating energy are attributed to the fast and efficient heating by RF electromagnetic fields and the presence of SS spacers along the membrane length, leading to direct heating near the membrane surface and negligible TP in addition to adequate mixing near the membrane surface (although it should be noted that CP was not assessed in this work).

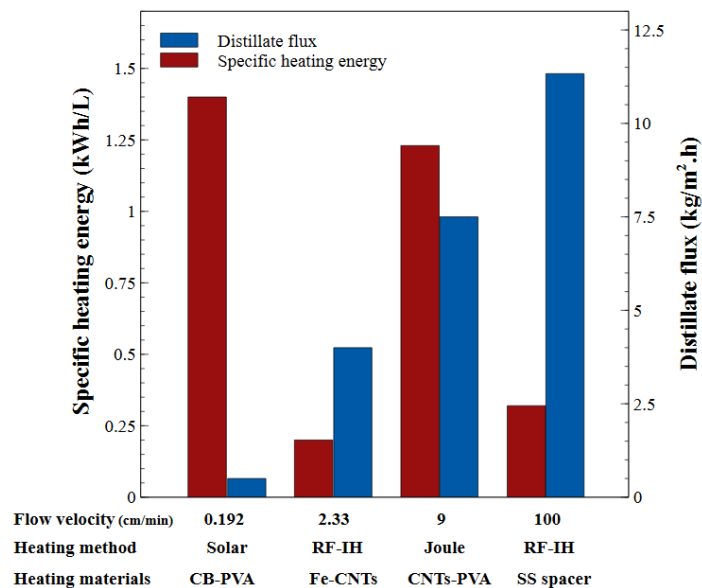


**Figure 4. 26.** Distillate flux and specific heating energy comparison of self-heated MD systems [178,188,194].

#### 4.3.8 Conclusions

Thermally conducting SS feed spacers heated by RF electromagnetic fields were shown for the first time as a new and appealing approach to directly heat the feed solution near the membrane surface. RF heating was found to be related to the mass of the spacer and therefore spacers with higher mass led to higher distillate flux. In addition to the spacer’s mass, the geometric structure of the spacer was shown to impact distillate flux while the spacer’s orientation was found negligible. Similar to other self-heating MD systems, higher distillate flux was obtained at lower flow velocities as the contact time of the feed solution and heated element increased. Results comparing the RF heated system to CMD systems are encouraging as they show a significant increase in distillate flux which is attributed to limited TP. In addition, the RF heated SS spacer-based MD system was able to significantly lower the energy requirement in comparison to other previously assessed self-heated MD systems even at relatively high flow velocities.

## CHAPTER 5

### COMPARISON, OVERALL CONCLUSION, AND FUTURE DIRECTIONS

**Preface:** The contents of this section are in part based on a published review article in Journal of Membrane Science: **Anvari, A.**, Yancheshme, A.A., Kekre, K. M., Ronen, A., "State-of-the-art methods for overcoming temperature polarization in membrane distillation process: A review", Journal of membrane science (2020): 118413 [114].

#### 5.1 Comparison of Self-heating MD Systems

Self-heated MD systems including solar, Joule, and induction heating (present study) were shown efficient in terms of decreasing TP as the temperature of the feed solution at the membrane's surface was higher than the bulk feed solution. However, the applicability of these systems should be assessed in terms of distillation performance and energy consumption. While solar heated MD systems have been shown very efficient in terms of energy as they use a renewable heat source, the applicability of these systems should be considered if they can produce adequate distillate flux. Furthermore, as solar systems require UV or IR light, they are not productive during about 50% of the time unless exposed to an external light source. Similarly, Joule heating and IH based MD configurations were shown to obtain high distillate flux; however, implementing them should be assessed in terms of energy as they use electricity to provide the heating energy. Therefore, in this section, the distillation performance and energy efficiency of self-heated MD processes have been summarized and compared. Generally, the distillation performance, energy consumption, and thermal efficiency of the MD process are evaluated based on the concept

of distillate flux (J), specific heating energy consumption ( $Q_{sh}$ ), and gain output ratio (GOR).

Table 5.1 and Figure 5.1 present a comparison of the distillation and energy performance of self-heated MD systems as described in the literature and present research (i.e., induction heated MD process). As all the systems are self-heated, the initial feed solutions ( $T_f$ ) were mostly at room temperature (20-25 °C), while for some experiments, the feed was heated to the temperature of 30-35 °. All energies in Table 5.1 and Figure 5.1 are reported as heating energy.  $Q_{sh}$  and GOR values are either reported in the literature or calculated based on equations 3.7 and 3.8 using the available data (e.g.,  $Q_{in}$ , J, etc.) in the literature. The best MD performance corresponds to the highest distillate flux, lowest  $Q_{sh}$ , and highest GOR. Higher GOR can be attained as consumed heating energy is reduced, or the distillate flux for a certain input heating energy is increased.

As shown in Table 5.1 and Figure 5.1, all solar heated MD systems, except Ag NPs coated membranes, applied relatively low input energy (around one sun irradiation energy, 0.7-1.367 kW/m<sup>2</sup>). However, their produced distillate flux values are comparatively low and varied between 0.33-6.1 kg/m<sup>2</sup>.h depending on the coated photothermal materials and operating conditions. Therefore, for solar heated systems,  $Q_{sh}$  values were obtained in the range of 0.22-2.1 kW/kg and GOR values of 0.32-3 (Figure 5.1). It should be noted that the self-assembled photothermal CB NPs and the metal nanoshell (SiO<sub>2</sub>/Au) based membranes displayed the lowest  $Q_{sh}$  values and the highest GORs, but the feed was preheated to 35 °C. The required energy for preheating was not considered here. In addition, the solar-heated Ag NPs coated membranes had high distillate flux as the result of very high input energy (23 kW/m<sup>2</sup>) through UV irradiation, leading to the low GOR and

high  $Q_{sh}$ . Overall, the performance and efficiency of solar energy typically lead to low GOR and low distillate flux and should be further optimized by increasing the photonic properties of the membrane and developing efficient optical designs under irradiation equal to solar energy (0.7-1 kW/m<sup>2</sup>). For Joule heating MD systems, higher distillate flux (7.5 kg/m<sup>2</sup>.h) was obtained for CNTs based membranes in comparison to the NRW hollow fiber membranes (2 kg/m<sup>2</sup>.h), this confirms the high efficiency of CNTs membranes as Joule heating elements. However, the obtained  $Q_{sh}$  values for both Joule heated MD systems are still high (Figure 5.1). The reported specific energy consumption value that included a vacuum pump, water bath, and the DC power supply for the Joule heated NRW membranes is 60 kWh/kg, which is the highest among all self-heated MD systems. However,  $Q_{sh}$  values presented in Figure 5.1 include only the specific heating energy as calculated in this research. Preheating (water bath) and pumping energy were not considered as the goal of this section is to compare only the required heating energy for the self-heating process. In addition, CNTs based membranes require additional optimization in terms of materials or designs to increase their energy efficiency. A comparison of all self-heated MD systems reveals that IH based MD with Fe-CNTs membranes had the highest GOR value (3.49) and lowest specific heating energy (0.197 kWh/kg), therefore, it can be considered highly effective. The relatively high distillate flux and low specific heating energy are attributed to the fast and efficient heating by RF electromagnetic fields. While the distillate flux of IH heated membranes is among the highest distillate flux values for self-heated MD systems, additional optimization is required to further increase distillate flux by increasing magnetic properties of membranes (e.g., thickness and mass loading of magnetic layer) or promoting local mixing by using IH-heated spacers.

Among all self-heated MD systems, except solar-heated Ag NPs coated membranes which have very high input energy, IH based spacers showed the highest distillate flux as spacers provide adequate local mixing near the membrane surface in addition to the direct heating process, leading to mitigation of both limiting phenomena as CP and TP. In addition, spacers allow distillation at higher flow velocities while all other self-heated MD systems are limited to the low flow velocities, leading to low mixing near the membrane surface and increase CP. Therefore, additional self-heating designs such as photothermal/electroactive heated flow promoters (i.e., spacers) should be considered as a method to prevent TP while simultaneously promoting local mixing.

**Table 5. 1.** Comparison of self-heated MD systems.

System code	Heating method	Heating materials	$Q_{in}$ (kW/m <sup>2</sup> )	$T_f$ (°C)	J (kg/m <sup>2</sup> .h)	Ref.
SH-Ag NPs	Solar irradiation	Ag NPs	23	30	25.7	[143]
SH-E Ag NPs	Solar irradiation	Electrospun Ag NPs	3.2	20	2.5	[179]
SH-CB PVA	Solar irradiation	Carbon black-PVA	0.7	20	0.5	[178]
SH-CB NPs	Solar irradiation	CB NPs	1.367	35	6.1	[180]
SH-SiO <sub>2</sub> /Au	Solar irradiation	SiO <sub>2</sub> /Au nanoshells	1.367	35	5.8	[180]
SH-Graphene	Solar irradiation	Graphene array	1	25	1.1	[181]
SH-PDA	Solar irradiation	PDA	0.75	20	0.49	[183]
SH-cESM-CNTs	Solar irradiation	cESM-CNTs	1	21	1.15	[184]
SH-Lens CB NPs	Solar irradiation	Lens array on CB NPs	0.7	20	0.33	[186]
JH-CNTs PVA	Joule heating	CNTs-PVA	11.1	20	7.5	[188]
JH-NRW	Joule heating	NRW	1.56	30	2	[193]
IH-Fe CNTs	Induction heating	Fe-CNTs	0.781	20	4	This study [194]
IH-SS	Induction heating	SS spacer	3.6	20	11.33	This study [245]

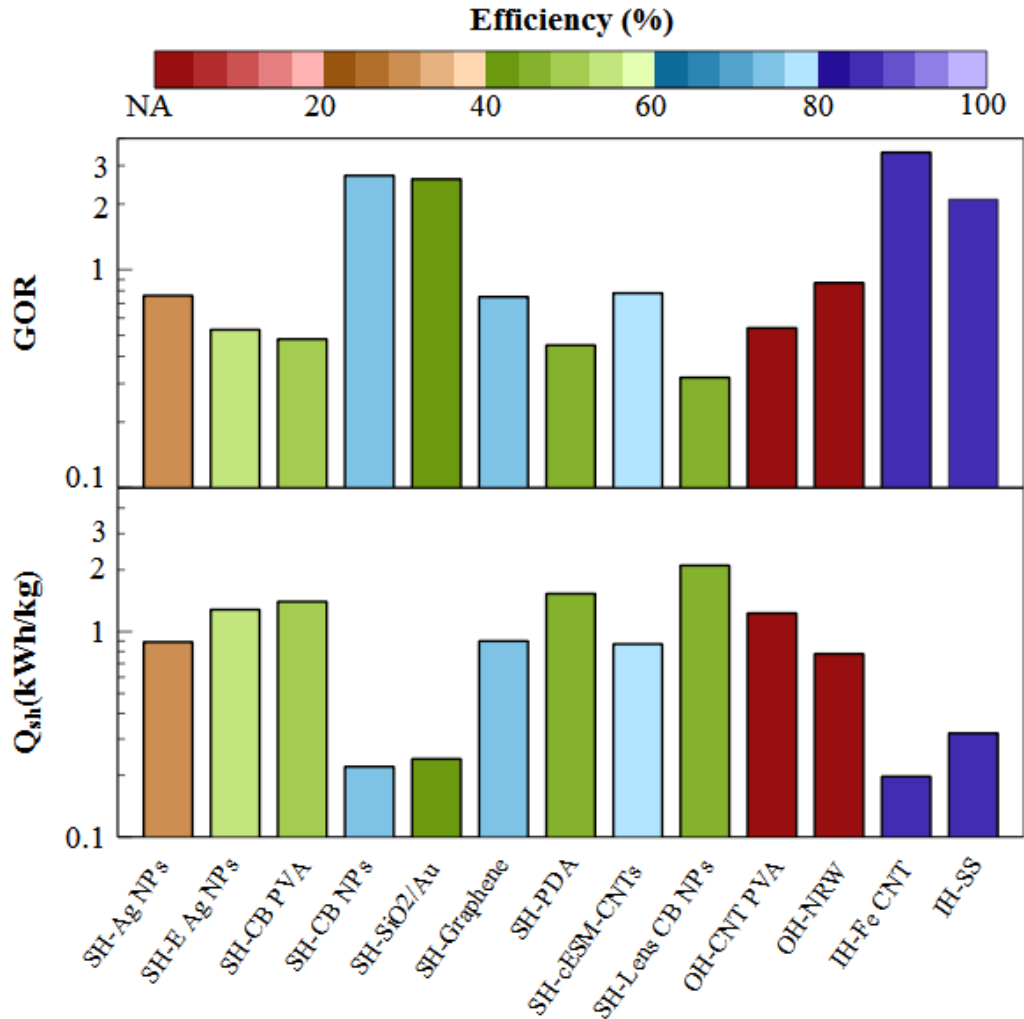


**Figure 5. 1.** Specific heating energy consumption ( $Q_{sh}$ ), gain output ratio (GOR), and energy efficiency of recently self-heated developed MD processes. Labels correspond to Table 5.1. Colors represent the efficiency percentage (%) of systems. NA: not available.

Overall, solar-heated MD systems could be promising in comparison to conventional MD systems as long as they are able to increase the produced distillate flux. Meanwhile, Joule heating and IH systems, which use electricity to provide the required heat can be comparable to solar-heated systems if they provide high distillate flux with very low specific heating energy or use renewable energy (i.e., PV cells) as their electricity source.

In terms of commercialization, solar-heated MD is still challenging as it is dependent on environmental conditions (i.e., sunny days). Furthermore, a large membrane surface area is required to receive adequate solar or UV light. For Joule heated MD systems, the commercialization challenges include expensive electrodes, high input energy, and large membrane surface area. Induction heated MD may be able to utilize the same input power to heat multiple layers of MD and therefore increase the produced distillate flux and energy efficiency accordingly. However, it still requires electricity to provide energy for heating which can be minimized by utilizing renewable energy (e.g., solar) to produce electricity for Joule heating and IH based MD configurations.

## **5.2 Overall Conclusion and future directions**

Temperature polarization and scaling are limiting factors that can affect the performance of MD processes in terms of distillate flux and energy efficiency. However, the advanced heating method based on induction heating was shown to be effective in mitigating TP and scaling of MD processes. In this research, RF-MD system with the ability to directly heat the feed solution at the membrane-water interface was presented and discussed.

Overall, the RF-VMD system was more efficient than conventional VMD system in terms of flux, specific heating energy, and scaling due to its negligible thermal polarization, low heat loss, direct feed heating on the membrane surface, and high mobility of ions under electromagnetic fields. Although MD commercialization is limited by the substantial energy required to generate distillate flux, results of this research are encouraging in terms of energy and flux, specifically for applications that require high salinity distillation with scaling tendency where pressure-based applications such as RO cannot be used.

Future studies are needed to evaluate the detailed TP and CP profiles theoretically, the detailed impact of membrane properties (e.g., mass and size of NPs along with using other conductive nanomaterials as graphene oxide (GO)), the detailed impact of spacer geometry (e.g., filament distances, surface area, and porosity), and the influence of different magnetic materials used for fabrication of magnetic element embedded to the hydrophobic membrane. In addition, heating patterns in the workpieces are known to be related to the difference in the eddy current distribution, therefore, material properties, applied frequency, and the IH system configuration (i.e., ratio of coil and workpiece length, distance, and orientation) are critical for optimizing the RF-MD system.

To gain higher flux, a higher surface area is required; therefore, hollow fiber modules should be considered instead of flat sheets, which are less efficient in terms of surface area per volume. In addition, organic fouling behavior of RF-MD system should be evaluated to improve the overall performance of the proposed RF-MD system for the application in realistic conditions.

Furthermore, additional studies are required on MD configurations integrating induction heating with renewable energy (solar/PV) to further decrease their energy consumption. Scaling up the IH system will require considering the materials used for the modules, as they must be made on non-conductive and non-magnetic materials such as polymers and plastics. Therefore, long term experiments are required prior to scale-up and commercialization of such systems.

## REFERENCES

- [1] E. Jones, M. Qadir, M.T.H. van Vliet, V. Smakhtin, S. mu Kang, The state of desalination and brine production: A global outlook, *Sci. Total Environ.* 657 (2019) 1343–1356. doi:10.1016/j.scitotenv.2018.12.076.
- [2] A.Y. Hoekstra, Water scarcity challenges to business, *Nat. Clim. Chang.* 4 (2014) 318–320. doi:10.1038/nclimate2214.
- [3] N.M. Wade, Distillation of plant development and cost update, *Desalination.* 136 (2001) 3–12. doi:10.1016/S0011-9164(01)00159-X.
- [4] J.A. Sanmartino, M. Khayet, M.C. García-Payo, H. El-Bakouri, A. Riaza, Treatment of reverse osmosis brine by direct contact membrane distillation: Chemical pretreatment approach, *Desalination.* 420 (2017) 79–90. doi:10.1016/j.desal.2017.06.030.
- [5] H.H. Salih, S.A. Dastgheib, Treatment of a hypersaline brine, extracted from a potential CO<sub>2</sub> sequestration site, and an industrial wastewater by membrane distillation and forward osmosis, *Chem. Eng. J.* 325 (2017) 415–423. doi:10.1016/j.cej.2017.05.075.
- [6] A. Giwa, V. Dufour, F. Al Marzooqi, M. Al Kaabi, S.W. Hasan, Brine management methods: Recent innovations and current status, *Desalination.* 407 (2017) 1–23. doi:10.1016/j.desal.2016.12.008.
- [7] V.G. Gude, Desalination and water reuse to address global water scarcity, *Rev. Environ. Sci. Biotechnol.* 16 (2017) 591–609. doi:10.1007/s11157-017-9449-7.
- [8] D.L. Shaffer, L.H. Arias Chavez, M. Ben-Sasson, S. Romero-Vargas Castrillón, N.Y. Yip, M. Elimelech, Desalination and reuse of high-salinity shale gas

- produced water: Drivers, technologies, and future directions, *Environ. Sci. Technol.* 47 (2013) 9569–9583. doi:10.1021/es401966e.
- [9] M. Elimelech, W.A. Phillip, The future of seawater desalination: Energy, technology, and the environment, *Science* (80-. ). 333 (2011) 712–717. doi:10.1126/science.1200488.
- [10] B.E. Jones, M. Qadir, V. Smakhtin, Quenching Humanity ’ s Freshwater Thirst Creates a Salty Threat, (2020) 2019–2021.
- [11] A. Deshmukh, C. Boo, V. Karanikola, S. Lin, A.P. Straub, T. Tong, D.M. Warsinger, M. Elimelech, Membrane distillation at the water-energy nexus: Limits, opportunities, and challenges, *Energy Environ. Sci.* 11 (2018) 1177–1196. doi:10.1039/c8ee00291f.
- [12] N. Ghaffour, T.M. Missimer, G.L. Amy, Technical review and evaluation of the economics of water desalination: Current and future challenges for better water supply sustainability, *Desalination*. (2013). doi:10.1016/j.desal.2012.10.015.
- [13] A. Suárez, P. Fernández, J. Ramón, E. Iglesias, F.A. Riera, Cost assessment of membrane processes : A practical example in the dairy wastewater reclamation by reverse osmosis, *J. Memb. Sci.* 493 (2015) 389–402. doi:10.1016/j.memsci.2015.04.065.
- [14] H. Fath, Z. Abbas, A. Khaled, Techno-economic assessment and environmental impacts of desalination technologies, 266 (2011) 263–273. doi:10.1016/j.desal.2010.08.035.
- [15] K. Jevons, M. Awe, Economic benefits of membrane technology vs . evaporator ☆, 250 (2010) 961–963. doi:10.1016/j.desal.2009.09.081.

- [16] K. Kimura, G. Amy, J.E. Drewes, T. Heberer, T. Kim, Y. Watanabe, Rejection of organic micropollutants ( disinfection by-products , endocrine disrupting compounds , and pharmaceutically active compounds ) by NF / RO membranes, 227 (2003) 113–121. doi:10.1016/j.memsci.2003.09.005.
- [17] I. Sutzkover-gutman, D. Hasson, Feed water pretreatment for desalination plants, DES. 264 (2010) 289–296. doi:10.1016/j.desal.2010.07.014.
- [18] S. Jamaly, N.N. Darwish, I. Ahmed, S.W. Hasan, A short review on reverse osmosis pretreatment technologies, DES. 354 (2014) 30–38. doi:10.1016/j.desal.2014.09.017.
- [19] A. Giwa, N. Akther, V. Dufour, S.W. Hasan, RSC Advances A critical review on recent polymeric and nano- enhanced membranes for reverse osmosis, (2016) 8134–8163. doi:10.1039/c5ra17221g.
- [20] N. Akther, A. Sodiq, A. Giwa, S. Daer, H.A. Arafat, S.W. Hasan, Recent advancements in forward osmosis desalination : A review, Chem. Eng. J. 281 (2015) 502–522. doi:10.1016/j.cej.2015.05.080.
- [21] B.B. Ashoor, S. Mansour, A. Giwa, V. Dufour, S.W. Hasan, Principles and applications of direct contact membrane distillation ( DCMD ): A comprehensive review, 398 (2016) 222–246. doi:10.1016/j.desal.2016.07.043.
- [22] K.W. Lawson, D.R. Lloyd, Membrane distillation, J. Memb. Sci. 124 (1997) 1–25. doi:10.1016/S0376-7388(96)00236-0.
- [23] S. Al-obaidani, E. Curcio, F. Macedonio, G. Di, H. Al-hinai, E. Drioli, Potential of membrane distillation in seawater desalination : Thermal efficiency , sensitivity study and cost estimation, 323 (2008) 85–98. doi:10.1016/j.memsci.2008.06.006.

- [24] E. Curcio, E. Drioli, Membrane distillation and related operations - A review, *Sep. Purif. Rev.* 34 (2005) 35–86. doi:10.1081/SPM-200054951.
- [25] A. Alkudhiri, N. Darwish, N. Hilal, Membrane distillation: A comprehensive review, *Desalination*. 287 (2012) 2–18. doi:10.1016/j.desal.2011.08.027.
- [26] M.S. El-Bourawi, Z. Ding, R. Ma, M. Khayet, A framework for better understanding membrane distillation separation process, *J. Memb. Sci.* 285 (2006) 4–29. doi:10.1016/j.memsci.2006.08.002.
- [27] A.M. Alklaibi, N. Lior, Membrane-distillation desalination: Status and potential, *Desalination*. 171 (2005) 111–131. doi:10.1016/j.desal.2004.03.024.
- [28] T.Y. Cath, V.D. Adams, A.E. Childress, Experimental study of desalination using direct contact membrane distillation : a new approach to flux enhancement, 228 (2004) 5–16. doi:10.1016/j.memsci.2003.09.006.
- [29] S. Adham, A. Hussain, J.M. Matar, R. Does, A. Janson, Application of Membrane Distillation for desalting brines from thermal desalination plants, *DES*. 314 (2013) 101–108. doi:10.1016/j.desal.2013.01.003.
- [30] J.A. Bush, J. Vanneste, T.Y. Cath, Membrane distillation for concentration of hypersaline brines from the Great Salt Lake : Effects of scaling and fouling on performance , efficiency , and salt rejection, *Sep. Purif. Technol.* 170 (2016) 78–91. doi:10.1016/j.seppur.2016.06.028.
- [31] B. Wu, X. Tan, W.K. Teo, K. Li, B. Wu, Removal of Benzene / Toluene from Water by Vacuum Membrane Distillation in a PVDF Hollow Fiber Membrane Module Removal of Benzene / Toluene from Water PVDF Hollow Fiber Membrane Module, 6395 (2006). doi:10.1080/01496390500283456.

- [32] A. Criscuoli, J. Zhong, A. Figoli, M.C. Carnevale, R. Huang, E. Drioli, Treatment of dye solutions by vacuum membrane distillation, *Water Res.* 42 (2008) 5031–5037. doi:10.1016/j.watres.2008.09.014.
- [33] L.D. Tijing, Y.C. Woo, J.S. Choi, S. Lee, S.H. Kim, H.K. Shon, Fouling and its control in membrane distillation-A review, *J. Memb. Sci.* 475 (2015) 215–244. doi:10.1016/j.memsci.2014.09.042.
- [34] S. Mozia, M. Tomaszewska, A.W. Morawski, Photocatalytic membrane reactor ( PMR ) coupling photocatalysis and membrane distillation — Effectiveness of removal of three azo dyes from water, 129 (2007) 3–8. doi:10.1016/j.cattod.2007.06.043.
- [35] D. Singh, K.K. Sirkar, Desalination of brine and produced water by direct contact membrane distillation at high temperatures and pressures, *J. Memb. Sci.* 389 (2012) 380–388. doi:10.1016/j.memsci.2011.11.003.
- [36] C.K. Chiam, R. Sarbatly, Vacuum membrane distillation processes for aqueous solution treatment-A review, *Chem. Eng. Process. Process Intensif.* 74 (2014) 27–54. doi:10.1016/j.cep.2013.10.002.
- [37] Z. Yan, H. Yang, F. Qu, H. Yu, H. Liang, G. Li, J. Ma, Reverse osmosis brine treatment using direct contact membrane distillation: Effects of feed temperature and velocity, *Desalination.* 423 (2017) 149–156. doi:10.1016/j.desal.2017.09.010.
- [38] F.A. Banat, J. Simandl, Removal of benzene traces from contaminated water by vacuum membrane distillation, *Chem. Eng. Sci.* (1996). doi:10.1016/0009-2509(95)00365-7.
- [39] C.F. Couto, M.C.S. Amaral, L.C. Lange, L.V. de S. Santos, Effect of humic acid

concentration on pharmaceutically active compounds (PhACs) rejection by direct contact membrane distillation (DCMD), *Sep. Purif. Technol.* (2019).

doi:10.1016/j.seppur.2018.12.012.

- [40] N. Mundhenk, P. Huttenloch, T. Kohl, H. Steger, R. Zorn, Metal corrosion in geothermal brine environments of the Upper Rhine graben - Laboratory and on-site studies, *Geothermics*. 46 (2013) 14–21.  
doi:10.1016/j.geothermics.2012.10.006.
- [41] P. Wang, T. Chung, Recent advances in membrane distillation processes : Membrane development , configuration design and application exploring, *J. Memb. Sci.* 474 (2015) 39–56. doi:10.1016/j.memsci.2014.09.016.
- [42] B.E. Logan, M. Elimelech, Membrane-based processes for sustainable power generation using water., *Nature*. 488 (2012) 313–9. doi:10.1038/nature11477.
- [43] A.S. Alsaadi, L. Francis, G.L. Amy, N. Ghaffour, Experimental and theoretical analyses of temperature polarization effect in vacuum membrane distillation, *J. Memb. Sci.* (2014). doi:10.1016/j.memsci.2014.08.005.
- [44] L. Martínez-Díez, M.I. Vázquez-González, Temperature Polarization in Mass Transport Through Hydrophobic Porous Membranes, *AIChE J.* (1996).  
doi:10.1002/aic.690420706.
- [45] L. Martínez-Díez, M.I. Vázquez-González, Temperature and concentration polarization in membrane distillation of aqueous salt solutions, *J. Memb. Sci.* (1999). doi:10.1016/S0376-7388(98)00349-4.
- [46] L.D. Tijing, Y. Chul, J. Choi, S. Lee, S. Kim, H. Kyong, Fouling and its control in membrane distillation — A review, *J. Memb. Sci.* 475 (2015) 215–244.

doi:10.1016/j.memsci.2014.09.042.

- [47] D.M. Warsinger, J. Swaminathan, E. Guillen-burrieza, H.A. Arafat, J.H.L. V, Scaling and fouling in membrane distillation for desalination applications : A review, *DES*. 356 (2015) 294–313. doi:10.1016/j.desal.2014.06.031.
- [48] M. Gryta, Alkaline scaling in the membrane distillation process, 228 (2008) 128–134. doi:10.1016/j.desal.2007.10.004.
- [49] F. He, K.K. Sirkar, J. Gilron, Studies on scaling of membranes in desalination by direct contact membrane distillation : CaCO<sub>3</sub> and mixed CaCO<sub>3</sub> / CaSO<sub>4</sub> systems, 64 (2009) 1844–1859. doi:10.1016/j.ces.2008.12.036.
- [50] S. Srisurichan, R. Jiraratananon, A.G. Fane, Mass transfer mechanisms and transport resistances in direct contact membrane distillation process, *J. Memb. Sci.* 277 (2006) 186–194. doi:10.1016/j.memsci.2005.10.028.
- [51] E. Curcio, X. Ji, G. Di, A. Obaidani, E. Fontananova, E. Drioli, Membrane distillation operated at high seawater concentration factors : Role of the membrane on CaCO<sub>3</sub> scaling in presence of humic acid, 346 (2010) 263–269. doi:10.1016/j.memsci.2009.09.044.
- [52] L. Wang, B. Li, X. Gao, Q. Wang, J. Lu, Y. Wang, S. Wang, Study of membrane fouling in cross-flow vacuum membrane distillation, *Sep. Purif. Technol.* 122 (2014) 133–143. doi:10.1016/j.seppur.2013.10.031.
- [53] F. He, J. Gilron, H. Lee, L. Song, K.K. Sirkar, Potential for scaling by sparingly soluble salts in crossflow DCMD, 311 (2008) 68–80. doi:10.1016/j.memsci.2007.11.056.
- [54] J. Ge, Y. Peng, Z. Li, P. Chen, S. Wang, Membrane fouling and wetting in a

- DCMD process for RO brine concentration, 344 (2014) 97–107.  
doi:10.1016/j.desal.2014.03.017.
- [55] E. Curcio, E. Drioli, E. Curcio, E. Drioli, Membrane Distillation and Related Operations — A Review, 2119 (2017). doi:10.1081/SPM-200054951.
- [56] F.A. Banat, J. Simandl, Desalination by Membrane Distillation : A Parametric Study, 6395 (2017). doi:10.1080/01496399808544764.
- [57] L. Song, Z. Ma, X. Liao, P.B. Kosaraju, J.R. Irish, K.K. Sirkar, Pilot plant studies of novel membranes and devices for direct contact membrane distillation-based desalination, 323 (2008) 257–270. doi:10.1016/j.memsci.2008.05.079.
- [58] E.K. Summers, H.A. Arafat, J.H.L. V, Energy efficiency comparison of single-stage membrane distillation ( MD ) desalination cycles in different configurations, DES. 290 (2012) 54–66. doi:10.1016/j.desal.2012.01.004.
- [59] M. Mahdi, A. Shirazi, A. Kargari, A. Fauzi, T. Matsuura, Computational Fluid Dynamic ( CFD ) opportunities applied to the membrane distillation process : State-of-the-art and perspectives, DES. 377 (2016) 73–90.  
doi:10.1016/j.desal.2015.09.010.
- [60] M.A.E.R. Abu-Zeid, Y. Zhang, H. Dong, L. Zhang, H.L. Chen, L. Hou, A comprehensive review of vacuum membrane distillation technique, Desalination. 356 (2015) 1–14. doi:10.1016/j.desal.2014.10.033.
- [61] M.A. Izquierdo-Gil, G. Jonsson, Factors affecting flux and ethanol separation performance in vacuum membrane distillation (VMD), J. Memb. Sci. (2003). doi:10.1016/S0376-7388(02)00540-9.
- [62] P. Termpiyakul, R. Jiratananon, S. Srisurichan, Heat and mass transfer

- characteristics of a direct contact membrane distillation process for desalination, *Desalination*. 177 (2005) 133–141. doi:10.1016/j.desal.2004.11.019.
- [63] Y.M. Manawi, M.A.M.M. Khraisheh, A.K. Fard, F. Benyahia, S. Adham, A predictive model for the assessment of the temperature polarization effect in direct contact membrane distillation desalination of high salinity feed, *Desalination*. (2014). doi:10.1016/j.desal.2014.02.028.
- [64] Y. Yun, R. Ma, W. Zhang, A.G. Fane, J. Li, Direct contact membrane distillation mechanism for high concentration NaCl solutions, *Desalination*. 188 (2006) 251–262. doi:10.1016/j.desal.2005.04.123.
- [65] S.T. Hsu, K.T. Cheng, J.S. Chiou, Seawater desalination by direct contact membrane distillation, *Desalination*. 143 (2002) 279–287. doi:10.1016/S0011-9164(02)00266-7.
- [66] K.W. Lawson, D.R. Lloyd, Membrane distillation. I. Module design and performance evaluation using vacuum membrane distillation, *J. Memb. Sci.* 120 (1996) 111–121. doi:10.1016/0376-7388(96)00140-8.
- [67] J.M.O. De Záarate, A. Velázquez, L. Peña, J.I. Mengual, J.M.O. De Záarate, A. Velázquez, L. Peña, J.I. Mengual, Influence of Temperature Polarization on Separation by Membrane Distillation, 6395 (2006). doi:10.1080/01496399308018048.
- [68] A.G. Fane, R.W. Schofield, C.J.D. Fell, The efficient use of energy in membrane distillation, *Desalination*. 64 (1987) 231–243. doi:10.1016/0011-9164(87)90099-3.
- [69] R. Ullah, M. Khraisheh, R.J. Esteves, J.T. McLeskey, M. AlGhouti, M. Gad-el-Hak, H. Vahedi Tafreshi, Energy efficiency of direct contact membrane

- distillation, *Desalination*. (2018). doi:10.1016/j.desal.2018.01.025.
- [70] L. Eykens, K. De Sitter, C. Dotremont, L. Pinoy, B. Van der Bruggen, How To Optimize the Membrane Properties for Membrane Distillation: A Review, *Ind. Eng. Chem. Res.* 55 (2016) 9333–9343. doi:10.1021/acs.iecr.6b02226.
- [71] K.Y. Wang, S.W. Foo, T. Chung, Mixed Matrix PVDF Hollow Fiber Membranes with Nanoscale Pores for Desalination through Direct Contact Membrane Distillation, (2009) 4474–4483.
- [72] J. Phattaranawik, R. Jiraratananon, A.G. Fane, Effect of pore size distribution and air flux on mass transport in direct contact membrane distillation, *J. Memb. Sci.* (2003). doi:10.1016/S0376-7388(02)00603-8.
- [73] T.C. Chen, C.D. Ho, H.M. Yeh, Theoretical modeling and experimental analysis of direct contact membrane distillation, *J. Memb. Sci.* (2009). doi:10.1016/j.memsci.2008.12.063.
- [74] J. Phattaranawik, R. Jiraratananon, A.G. Fane, C. Halim, Mass flux enhancement using spacer filled channels in direct contact membrane distillation, *J. Memb. Sci.* (2001). doi:10.1016/S0376-7388(01)00344-1.
- [75] A.R. Da Costa, A.G. Fane, D.E. Wiley, Spacer characterization and pressure drop modelling in spacer-filled channels for ultrafiltration, *J. Memb. Sci.* (1994). doi:10.1016/0376-7388(93)E0076-P.
- [76] J. Phattaranawik, R. Jiraratananon, A.G. Fane, Effects of net-type spacers on heat and mass transfer in direct contact membrane distillation and comparison with ultrafiltration studies, *J. Memb. Sci.* (2003). doi:10.1016/S0376-7388(03)00130-3.
- [77] S. Meng, J. Mansouri, Y. Ye, V. Chen, Effect of templating agents on the

- properties and membrane distillation performance of TiO<sub>2</sub>-coated PVDF membranes, *J. Memb. Sci.* (2014). doi:10.1016/j.memsci.2013.08.036.
- [78] J.A. Kharraz, M.R. Bilad, H.A. Arafat, Flux stabilization in membrane distillation desalination of seawater and brine using corrugated PVDF membranes, *J. Memb. Sci.* (2015). doi:10.1016/j.memsci.2015.08.039.
- [79] M. A, E. Y, Experimental Evaluation of Corrugated Feed Channel of Direct Contact Membrane Distillation, *J. Membr. Sci. Technol.* (2016). doi:10.4172/2155-9589.1000151.
- [80] M. Khayet, Membranes and theoretical modeling of membrane distillation : A review, *Adv. Colloid Interface Sci.* 164 (2011) 56–88. doi:10.1016/j.cis.2010.09.005.
- [81] M. Tomaszewska, Membrane Distillation - Examples of Applications in Technology and Environmental Protection, 9 (2000).
- [82] V. V Ugrozov, I.B. Elkina, Mathematical modeling of influence of porous structure a membrane on its vapour-conductivity in the process of membrane distillation, 147 (2002) 167–171.
- [83] J. Woods, J. Pellegrino, J. Burch, Generalized guidance for considering pore-size distribution in membrane distillation, *J. Memb. Sci.* 368 (2011) 124–133. doi:10.1016/j.memsci.2010.11.041.
- [84] L. Eykens, I. Hitsov, K. De Sitter, C. Dotremont, L. Pinoy, I. Nopens, Influence of membrane thickness and process conditions on direct contact membrane distillation at different salinities, *J. Memb. Sci.* 498 (2016) 353–364. doi:10.1016/j.memsci.2015.07.037.

- [85] J. Phattaranawik, R. Jiraratananon, A.G. Fane, Heat transport and membrane distillation coefficients in direct contact membrane distillation, *J. Memb. Sci.* 212 (2003) 177–193. doi:10.1016/S0376-7388(02)00498-2.
- [86] E. Drioli, A. Ali, F. Macedonio, Membrane distillation : Recent developments and perspectives, 356 (2015) 56–84.
- [87] K.W. Lawson, D.R. Lloyd, Membrane distillation. I. Module design and performance evaluation using vacuum membrane distillation, *J. Memb. Sci.* 120 (1996) 111–121. doi:10.1016/0376-7388(96)00140-8.
- [88] M. Khayet, P. Godino, J.I. Mengual, Nature of flow on sweeping gas membrane distillation, *J. Memb. Sci.* 170 (2000) 243–255. doi:10.1016/S0376-7388(99)00369-5.
- [89] M.I. V, Study of evaporation efficiency in membrane distillation, 126 (2000) 193–198.
- [90] R.W. Schofield, A.G. Fane, C.J.D. Fell, R. Macoun, Factors affecting flux in membrane distillation, *Desalination.* (1990). doi:10.1016/0011-9164(90)85030-E.
- [91] S. SRISURICHAN, R. JIRARATANANON, A. FANE, Mass transfer mechanisms and transport resistances in direct contact membrane distillation process, *J. Memb. Sci.* 277 (2006) 186–194. doi:10.1016/j.memsci.2005.10.028.
- [92] L. Martlnez, Comparison of membrane distillation performance using different feeds, 168 (2004) 359–365.
- [93] M. Qtaishat, T. Matsuura, B. Kruczek, M. Khayet, Heat and mass transfer analysis in direct contact membrane distillation, 219 (2008) 272–292. doi:10.1016/j.desal.2007.05.019.

- [94] C. Ferna, M.C. Garcõ, Air gap membrane distillation of sucrose aqueous solutions, 155 (1999).
- [95] M. Gryta, Calcium sulphate scaling in membrane distillation process ‡, 63 (2009) 146–151. doi:10.2478/s11696-008-0095-y.
- [96] L.D. Nghiem, T. Cath, Author ' s personal copy A scaling mitigation approach during direct contact membrane distillation Author ' s personal copy, 80 (2011) 315–322. doi:10.1016/j.seppur.2011.05.013.
- [97] D.M. Warsinger, E.W. Tow, J. Swaminathan, J.H.L. V, Theoretical framework for predicting inorganic fouling in membrane distillation and experimental validation with calcium sulfate, J. Memb. Sci. 528 (2017) 381–390. doi:10.1016/j.memsci.2017.01.031.
- [98] G. Naidu, S. Jeong, Y. Choi, E. Jang, T. Hwang, S. Vigneswaran, Application of vacuum membrane distillation for small scale drinking water production, DES. 354 (2014) 53–61. doi:10.1016/j.desal.2014.09.026.
- [99] D. Hou, Z. Wang, G. Li, H. Fan, J. Wang, H. Huang, Ultrasonic assisted direct contact membrane distillation hybrid process for membrane scaling mitigation, DES. 375 (2015) 33–39. doi:10.1016/j.desal.2015.07.018.
- [100] T. Zou, X. Dong, G. Kang, M. Zhou, M. Li, Y. Cao, Fouling behavior and scaling mitigation strategy of CaSO<sub>4</sub> in submerged vacuum membrane distillation, Desalination. 425 (2018) 86–93. doi:10.1016/j.desal.2017.10.015.
- [101] H.C. Duong, M. Duke, S. Gray, P. Cooper, L.D. Nghiem, Membrane scaling and prevention techniques during seawater desalination by air gap membrane distillation, DES. 397 (2016) 92–100. doi:10.1016/j.desal.2016.06.025.

- [102] P. Zhang, P. Knötig, S. Gray, M. Duke, Scale reduction and cleaning techniques during direct contact membrane distillation of seawater reverse osmosis brine, *DES*. 374 (2015) 20–30. doi:10.1016/j.desal.2015.07.005.
- [103] M. Gryta, Long-term performance of membrane distillation process, 265 (2005) 153–159. doi:10.1016/j.memsci.2005.04.049.
- [104] A. Razmjou, E. Arifin, G. Dong, J. Mansouri, V. Chen, Superhydrophobic modification of TiO<sub>2</sub> nanocomposite PVDF membranes for applications in membrane distillation, *J. Memb. Sci.* 415–416 (2012) 850–863. doi:10.1016/j.memsci.2012.06.004.
- [105] H.K. Shon, S.H. Kim, S. Vigneswaran, R. Ben Aim, S. Lee, J. Cho, Physico-Chemical Pretreatment of Seawater : Fouling Reduction and Membrane Characterization, (n.d.).
- [106] J. Wang, D. Qu, M. Tie, H. Ren, X. Peng, Z. Luan, Effect of coagulation pretreatment on membrane distillation process for desalination of recirculating cooling water, 64 (2008) 108–115. doi:10.1016/j.seppur.2008.07.022.
- [107] L. Tang, A. Iddya, X. Zhu, A. V. Dudchenko, W. Duan, C. Turchi, J. Vanneste, T.Y. Cath, D. Jassby, Enhanced Flux and Electrochemical Cleaning of Silicate Scaling on Carbon Nanotube-Coated Membrane Distillation Membranes Treating Geothermal Brines, *ACS Appl. Mater. Interfaces*. (2017). doi:10.1021/acsami.7b12615.
- [108] M.S. Humoud, S. Roy, Scaling Reduction in Carbon Nanotube-Immobilized Membrane during Membrane Distillation, (2019).
- [109] S. Jeong, S.J. Kim, L. Hee Kim, M. Seop Shin, S. Vigneswaran, T. Vinh Nguyen,

- I.S. Kim, Foulant analysis of a reverse osmosis membrane used pretreated seawater, *J. Memb. Sci.* (2013). doi:10.1016/j.memsci.2012.11.007.
- [110] D. Jermann, W. Pronk, S. Meylan, M. Boller, Interplay of different NOM fouling mechanisms during ultrafiltration for drinking water production, *Water Res.* (2007). doi:10.1016/j.watres.2006.12.030.
- [111] S. Srisurichan, R. Jiraratananon, A.G. Fane, Humic acid fouling in the membrane distillation process, *Desalination.* (2005). doi:10.1016/j.desal.2004.09.003.
- [112] G. Naidu, S. Jeong, S.J. Kim, I.S. Kim, S. Vigneswaran, Organic fouling behavior in direct contact membrane distillation, *Desalination.* (2014). doi:10.1016/j.desal.2014.05.045.
- [113] X. Jin, A. Jawor, S. Kim, E.M.V. Hoek, Effects of feed water temperature on separation performance and organic fouling of brackish water RO membranes, *Desalination.* (2009). doi:10.1016/j.desal.2008.03.026.
- [114] A. Anvari, A.A. Yancheshme, K.M. Kekre, A. Ronen, State-of-the-art methods for overcoming temperature polarization in membrane distillation process: A review, *J. Memb. Sci.* (2020) 118413. doi:10.1016/j.memsci.2020.118413.
- [115] L. Liu, F. Shen, X. Chen, J. Luo, Y. Su, H. Wu, Y. Wan, A novel plasma-induced surface hydrophobization strategy for membrane distillation: Etching, dipping and grafting, *J. Memb. Sci.* (2016). doi:10.1016/j.memsci.2015.11.003.
- [116] S. Majidi Salehi, G. Di Profio, E. Fontananova, F.P. Nicoletta, E. Curcio, G. De Filpo, Membrane distillation by novel hydrogel composite membranes, *J. Memb. Sci.* (2016). doi:10.1016/j.memsci.2015.12.062.
- [117] M. Essalhi, M. Khayet, Surface segregation of fluorinated modifying

- macromolecule for hydrophobic/hydrophilic membrane preparation and application in air gap and direct contact membrane distillation, *J. Memb. Sci.* 417–418 (2012) 163–173. doi:10.1016/j.memsci.2012.06.028.
- [118] J.A. Prince, D. Rana, G. Singh, T. Matsuura, T. Jun Kai, T.S. Shanmugasundaram, Effect of hydrophobic surface modifying macromolecules on differently produced PVDF membranes for direct contact membrane distillation, *Chem. Eng. J.* (2014). doi:10.1016/j.cej.2013.11.039.
- [119] A. Rastegarpanah, H.R. Mortaheb, Surface treatment of polyethersulfone membranes for applying in desalination by direct contact membrane distillation, *Desalination.* (2016). doi:10.1016/j.desal.2015.09.008.
- [120] H.C. Yang, W. Zhong, J. Hou, V. Chen, Z.K. Xu, Janus hollow fiber membrane with a mussel-inspired coating on the lumen surface for direct contact membrane distillation, *J. Memb. Sci.* (2017). doi:10.1016/j.memsci.2016.09.044.
- [121] W.T. Xu, Z.P. Zhao, M. Liu, K.C. Chen, Morphological and hydrophobic modifications of PVDF flat membrane with silane coupling agent grafting via plasma flow for VMD of ethanol-water mixture, *J. Memb. Sci.* (2015). doi:10.1016/j.memsci.2015.05.024.
- [122] M. Bhadra, S. Roy, S. Mitra, Enhanced desalination using carboxylated carbon nanotube immobilized membranes, *Sep. Purif. Technol.* (2013). doi:10.1016/j.seppur.2013.10.020.
- [123] M. Bhadra, S. Roy, S. Mitra, Nanodiamond immobilized membranes for enhanced desalination via membrane distillation, *Desalination.* (2014). doi:10.1016/j.desal.2014.02.036.

- [124] M. Bhadra, S. Roy, S. Mitra, Desalination across a graphene oxide membrane via direct contact membrane distillation, *Desalination*. 378 (2016) 37–43.  
doi:10.1016/j.desal.2015.09.026.
- [125] A. Jafari, M.R.S. Kebria, A. Rahimpour, G. Bakeri, Graphene quantum dots modified polyvinylidene fluoride (PVDF) nanofibrous membranes with enhanced performance for air Gap membrane distillation, *Chem. Eng. Process. - Process Intensif.* (2018). doi:10.1016/j.cep.2018.03.010.
- [126] A.K. An, E.J. Lee, J. Guo, S. Jeong, J.G. Lee, N. Ghaffour, Enhanced vapor transport in membrane distillation via functionalized carbon nanotubes anchored into electrospun nanofibres, *Sci. Rep.* (2017). doi:10.1038/srep41562.
- [127] S. Ragunath, S. Roy, S. Mitra, Carbon nanotube immobilized membrane with controlled nanotube incorporation via phase inversion polymerization for membrane distillation based desalination, *Sep. Purif. Technol.* (2018).  
doi:10.1016/j.seppur.2017.11.053.
- [128] M. Bhadra, S. Roy, S. Mitra, Flux enhancement in direct contact membrane distillation by implementing carbon nanotube immobilized PTFE membrane, *Sep. Purif. Technol.* (2016). doi:10.1016/j.seppur.2016.01.046.
- [129] J.E. Efome, M. Baghbanzadeh, D. Rana, T. Matsuura, C.Q. Lan, Effects of superhydrophobic SiO<sub>2</sub> nanoparticles on the performance of PVDF flat sheet membranes for vacuum membrane distillation, *Desalination*. (2015).  
doi:10.1016/j.desal.2015.07.002.
- [130] B. Kumanek, D. Janas, Thermal conductivity of carbon nanotube networks: a review, *J. Mater. Sci.* (2019). doi:10.1007/s10853-019-03368-0.

- [131] C.M. Hussain, C. Saridara, S. Mitra, Altering the polarity of self-assembled carbon nanotubes stationary phase via covalent functionalization, *RSC Adv.* (2011). doi:10.1039/c1ra00341k.
- [132] M. Bhadra, S. Roy, S. Mitra, A Bilayered Structure Comprised of Functionalized Carbon Nanotubes for Desalination by Membrane Distillation, *ACS Appl. Mater. Interfaces.* 8 (2016) 19507–19513. doi:10.1021/acsami.6b05644.
- [133] R. Zhou, D. Rana, T. Matsuura, C.Q. Lan, Effects of multi-walled carbon nanotubes (MWCNTs) and integrated MWCNTs/SiO<sub>2</sub> nano-additives on PVDF polymeric membranes for vacuum membrane distillation, *Sep. Purif. Technol.* 217 (2019) 154–163. doi:10.1016/j.seppur.2019.02.013.
- [134] S. Roy, M. Bhadra, S. Mitra, Enhanced desalination via functionalized carbon nanotube immobilized membrane in direct contact membrane distillation, *Sep. Purif. Technol.* 136 (2014) 58–65. doi:10.1016/j.seppur.2014.08.009.
- [135] M. Qtaishat, D. Rana, M. Khayet, T. Matsuura, Preparation and characterization of novel hydrophobic/hydrophilic polyetherimide composite membranes for desalination by direct contact membrane distillation, *J. Memb. Sci.* 327 (2009) 264–273. doi:10.1016/j.memsci.2008.11.040.
- [136] M. Qtaishat, M. Khayet, T. Matsuura, Novel porous composite hydrophobic/hydrophilic polysulfone membranes for desalination by direct contact membrane distillation, *J. Memb. Sci.* 341 (2009) 139–148. doi:10.1016/j.memsci.2009.05.053.
- [137] M. Khayet, J.I. Mengual, T. Matsuura, Porous hydrophobic/hydrophilic composite membranes: Application in desalination using direct contact membrane distillation,

- J. Memb. Sci. 252 (2005) 101–113. doi:10.1016/j.memsci.2004.11.022.
- [138] S. Mansour, A. Giwa, S.W. Hasan, Novel graphene nanoplatelets-coated polyethylene membrane for the treatment of reject brine by pilot-scale direct contact membrane distillation: An optimization study, *Desalination*. (2018). doi:10.1016/j.desal.2018.04.026.
- [139] M. Hu, S. Zheng, B. Mi, Organic Fouling of Graphene Oxide Membranes and Its Implications for Membrane Fouling Control in Engineered Osmosis, (2016). doi:10.1021/acs.est.5b03916.
- [140] B. Cao, A. Ansari, X. Yi, D.F. Rodrigues, Y. Hu, Gypsum scale formation on graphene oxide modified reverse osmosis membrane, *J. Memb. Sci.* (2018). doi:10.1016/j.memsci.2018.02.005.
- [141] D. Cohen-Tanugi, J.C. Grossman, Water desalination across nanoporous graphene, *Nano Lett.* (2012). doi:10.1021/nl3012853.
- [142] A. Politano, P. Argurio, G. Di Profio, V. Sanna, A. Cupolillo, S. Chakraborty, H.A. Arafat, E. Curcio, Photothermal Membrane Distillation for Seawater Desalination, *Adv. Mater.* 29 (2017) 1–6. doi:10.1002/adma.201603504.
- [143] A. Politano, G. Di Profio, E. Fontananova, V. Sanna, A. Cupolillo, E. Curcio, Overcoming temperature polarization in membrane distillation by thermoplasmonic effects activated by Ag nanofillers in polymeric membranes, *Desalination*. 451 (2019) 192–199. doi:10.1016/j.desal.2018.03.006.
- [144] Q. Huang, S. Gao, Y. Huang, M. Zhang, C. Xiao, Study on photothermal PVDF/ATO nanofiber membrane and its membrane distillation performance, *J. Memb. Sci.* 582 (2019) 203–210. doi:10.1016/j.memsci.2019.04.019.

- [145] H. Wang, Y. Wu, X. Yuan, G. Zeng, J. Zhou, X. Wang, J.W. Chew, Clay-Inspired MXene-Based Electrochemical Devices and Photo-Electrocatalyst: State-of-the-Art Progresses and Challenges, *Adv. Mater.* (2018). doi:10.1002/adma.201704561.
- [146] Y.Z. Tan, H. Wang, L. Han, M.B. Tanis-Kanbur, M.V. Pranav, J.W. Chew, Photothermal-enhanced and fouling-resistant membrane for solar-assisted membrane distillation, *J. Memb. Sci.* 565 (2018) 254–265. doi:10.1016/j.memsci.2018.08.032.
- [147] Y.D. Kim, L. Francis, J.G. Lee, M.G. Ham, N. Ghaffour, Effect of non-woven net spacer on a direct contact membrane distillation performance: Experimental and theoretical studies, *J. Memb. Sci.* (2018). doi:10.1016/j.memsci.2018.07.019.
- [148] H. Abdallah, A.F. Moustafa, A.A.H. AlAnezi, H.E.M. El-Sayed, Performance of a newly developed titanium oxide nanotubes/polyethersulfone blend membrane for water desalination using vacuum membrane distillation, *Desalination.* 346 (2014) 30–36. doi:10.1016/j.desal.2014.05.003.
- [149] L. Martínez-Díez, M.I. Vázquez-González, F.J. Florido-Díaz, Study of membrane distillation using channel spacers, *J. Memb. Sci.* (1998). doi:10.1016/S0376-7388(98)00024-6.
- [150] R.W. Schofield, A.G. Fane, R. Macoun, Factors Affecting Flux in Membrane Distillation, *77* (1990) 279–294.
- [151] A. Katsandri, A theoretical analysis of a spacer filled flat plate membrane distillation modules using CFD: Part I: velocity and shear stress analysis, *Desalination.* 408 (2017) 145–165. doi:10.1016/j.desal.2015.09.001.
- [152] Y. Taamneh, K. Bataineh, Improving the performance of direct contact membrane

- distillation utilizing spacer-filled channel, *Desalination*. 408 (2017) 25–35.  
doi:10.1016/j.desal.2017.01.004.
- [153] L. Gurreri, A. Tamburini, A. Cipollina, G. Micale, M. Ciofalo, CFD prediction of concentration polarization phenomena in spacer-filled channels for reverse electro dialysis, *J. Memb. Sci.* (2014). doi:10.1016/j.memsci.2014.05.058.
- [154] H. Chang, J. Hsu, C. Chang, C. Ho, T. Cheng, Simulation study of transfer characteristics for spacer-filled membrane distillation desalination modules q, *Appl. Energy*. 185 (2017) 2045–2057. doi:10.1016/j.apenergy.2015.12.030.
- [155] M. Albeirutty, N. Turkmen, S. Al-Sharif, S. Bouguecha, A. Malik, O. Faruki, A. Cipollina, M. Ciofalo, G. Micale, An experimental study for the characterization of fluid dynamics and heat transport within the spacer-filled channels of membrane distillation modules, *Desalination*. 430 (2018) 136–146.  
doi:10.1016/j.desal.2017.12.043.
- [156] J. Seo, Y.M. Kim, J.H. Kim, Spacer optimization strategy for direct contact membrane distillation: Shapes, configurations, diameters, and numbers of spacer filaments, *Desalination*. 417 (2017) 9–18. doi:10.1016/j.desal.2017.05.009.
- [157] A. Hagedorn, G. Fieg, D. Winter, J. Koschikowski, A. Grabowski, T. Mann, Membrane and spacer evaluation with respect to future module design in membrane distillation, *Desalination*. 413 (2017) 154–167.  
doi:10.1016/j.desal.2017.03.016.
- [158] M. Shakaib, S.M.F. Hasani, I. Ahmed, R.M. Yunus, A CFD study on the effect of spacer orientation on temperature polarization in membrane distillation modules, *Desalination*. (2012). doi:10.1016/j.desal.2011.09.020.

- [159] A. Katsandri, A theoretical analysis of a spacer filled flat plate membrane distillation modules using CFD: Part II: Temperature polarisation analysis, *Desalination*. 408 (2017) 166–180. doi:10.1016/j.desal.2015.11.021.
- [160] L. Martínez, J.M. Rodríguez-Maroto, Characterization of membrane distillation modules and analysis of mass flux enhancement by channel spacers, *J. Memb. Sci.* (2006). doi:10.1016/j.memsci.2005.07.045.
- [161] E.H.C. Castillo, N. Thomas, O. Al-Ketan, R. Rowshan, R.K. Abu Al-Rub, L.D. Nghiem, S. Vigneswaran, H.A. Arafat, G. Naidu, 3D printed spacers for organic fouling mitigation in membrane distillation, *J. Memb. Sci.* 581 (2019) 331–343. doi:10.1016/j.memsci.2019.03.040.
- [162] N. Thomas, N. Sreedhar, O. Al-Ketan, R. Rowshan, R.K. Abu Al-Rub, H. Arafat, 3D printed triply periodic minimal surfaces as spacers for enhanced heat and mass transfer in membrane distillation, *Desalination*. (2018). doi:10.1016/j.desal.2018.06.009.
- [163] N. Thomas, N. Sreedhar, O. Al-Ketan, R. Rowshan, R.K. Abu Al-Rub, H. Arafat, 3D printed spacers based on TPMS architectures for scaling control in membrane distillation, *J. Memb. Sci.* 581 (2019) 38–49. doi:10.1016/j.memsci.2019.03.039.
- [164] E.A. Lord, A.L. Mackay, Periodic minimal surfaces of cubic symmetry, *Curr. Sci.* (2003).
- [165] J. Swaminathan, H.W. Chung, D.M. Warsinger, F.A. AlMarzooqi, H.A. Arafat, J.H. Lienhard, Energy efficiency of permeate gap and novel conductive gap membrane distillation, *J. Memb. Sci.* 502 (2016) 171–178. doi:10.1016/j.memsci.2015.12.017.

- [166] Y.Z. Tan, E.H. Ang, J.W. Chew, Metallic spacers to enhance membrane distillation, *J. Memb. Sci.* 572 (2019) 171–183.  
doi:10.1016/j.memsci.2018.10.073.
- [167] S. Parekh, M.M. Farid, J.R. Selmán, S. Al-Hallaj, Solar desalination with a humidification-dehumidification technique - A comprehensive technical review, *Desalination*. (2004). doi:10.1016/S0011-9164(04)90007-0.
- [168] F. Suárez, S.W. Tyler, A.E. Childress, A theoretical study of a direct contact membrane distillation system coupled to a salt-gradient solar pond for terminal lakes reclamation, *Water Res.* (2010). doi:10.1016/j.watres.2010.05.050.
- [169] A. Saleh, J.A. Qudeiri, M.A. Al-Nimr, Performance investigation of a salt gradient solar pond coupled with desalination facility near the Dead Sea, *Energy*. (2011). doi:10.1016/j.energy.2010.12.018.
- [170] A. Chafidz, E.D. Kerme, I. Wazeer, Y. Khalid, A. Ajbar, S.M. Al-Zahrani, Design and fabrication of a portable and hybrid solar-powered membrane distillation system, *J. Clean. Prod.* (2016). doi:10.1016/j.jclepro.2016.05.127.
- [171] M.R. Qtaishat, F. Banat, Desalination by solar powered membrane distillation systems, *Desalination*. (2013). doi:10.1016/j.desal.2012.01.021.
- [172] J. Koschikowski, M. Wieghaus, M. Rommel, Solar thermal driven desalination plants based on membrane distillation, *Desalination*. 156 (2003) 295–304.  
doi:10.1016/S0011-9164(03)00360-6.
- [173] Z. Ding, L. Liu, M.S. El-Bourawi, R. Ma, Analysis of a solar-powered membrane distillation system, *Desalination*. 172 (2005) 27–40.  
doi:10.1016/j.desal.2004.06.195.

- [174] H. Chang, G.B. Wang, Y.H. Chen, C.C. Li, C.L. Chang, Modeling and optimization of a solar driven membrane distillation desalination system, *Renew. Energy*. (2010). doi:10.1016/j.renene.2010.04.020.
- [175] T.C. Chen, C.D. Ho, Immediate assisted solar direct contact membrane distillation in saline water desalination, *J. Memb. Sci.* (2010). doi:10.1016/j.memsci.2010.04.037.
- [176] Y. Zhang, L. Liu, K. Li, D. Hou, J. Wang, Enhancement of energy utilization using nanofluid in solar powered membrane distillation, *Chemosphere*. 212 (2018) 554–562. doi:10.1016/j.chemosphere.2018.08.114.
- [177] G. Xue, Q. Chen, S. Lin, J. Duan, P. Yang, K. Liu, J. Li, Highly Efficient Water Harvesting with Optimized Solar Thermal Membrane Distillation Device, 1800001 (2018) 1–6. doi:10.1002/gch2.201800001.
- [178] P.D. Dongare, A. Alabastri, S. Pedersen, K.R. Zodrow, N.J. Hogan, O. Neumann, J. Wud, T. Wang, A. Deshmukh, M. Elimelech, Q. Li, P. Nordlander, N.J. Halas, Nanophotonics-enabled solar membrane distillation for off-grid water purification, *Proc. Natl. Acad. Sci. U. S. A.* 114 (2017) 6936–6941. doi:10.1073/pnas.1701835114.
- [179] H. Ye, X. Li, L. Deng, P. Li, T. Zhang, X. Wang, B.S. Hsiao, Silver Nanoparticle-Enabled Photothermal Nanofibrous Membrane for Light-Driven Membrane Distillation, *Ind. Eng. Chem. Res.* 58 (2019) 3269–3281. doi:10.1021/acs.iecr.8b04708.
- [180] J. Wu, K.R. Zodrow, P.B. Szemraj, Q. Li, Photothermal nanocomposite membranes for direct solar membrane distillation, *J. Mater. Chem. A*. 5 (2017)

23712–23719. doi:10.1039/c7ta04555g.

- [181] B. Gong, H. Yang, S. Wu, G. Xiong, J. Yan, K. Cen, Graphene Array - Based Anti - fouling Solar Vapour Gap Membrane Distillation with High Energy Efficiency, *Nano-Micro Lett.* 11 (2019) 1–14. doi:10.1007/s40820-019-0281-1.
- [182] A. Alabastri, P.D. Dongare, O. Neumann, J. Metz, I. Adebisi, P. Nordlander, N.J. Halas, Resonant energy transfer enhances solar thermal desalination, *Energy Environ. Sci.* 13 (2020) 968–976. doi:10.1039/c9ee03256h.
- [183] X. Wu, Q. Jiang, D. Ghim, S. Singamaneni, Y.S. Jun, Localized heating with a photothermal polydopamine coating facilitates a novel membrane distillation process, *J. Mater. Chem. A.* 6 (2018) 18799–18807. doi:10.1039/c8ta05738a.
- [184] X. Han, W. Wang, K. Zuo, L. Chen, L. Yuan, J. Liang, Q. Li, P.M. Ajayan, Y. Zhao, J. Lou, Bio-derived ultrathin membrane for solar driven water purification, *Nano Energy.* 60 (2019) 567–575. doi:10.1016/j.nanoen.2019.03.089.
- [185] E.K. Summers, J.H. Lienhard, Experimental study of thermal performance in air gap membrane distillation systems, including the direct solar heating of membranes, *Desalination.* (2013). doi:10.1016/j.desal.2013.09.023.
- [186] P.D. Dongare, A. Alabastri, O. Neumann, P. Nordlander, N.J. Halas, Solar thermal desalination as a nonlinear optical process, *Proc. Natl. Acad. Sci. U. S. A.* (2019). doi:10.1073/pnas.1905311116.
- [187] X. Xuan, Joule heating in electrokinetic flow, *Electrophoresis.* 29 (2008) 33–43. doi:10.1002/elps.200700302.
- [188] A. V. Dudchenko, C. Chen, A. Cardenas, J. Rolf, D. Jassby, Frequency-dependent stability of CNT Joule heaters in ionizable media and desalination processes, *Nat.*

Nanotechnol. 12 (2017) 557–563. doi:10.1038/nnano.2017.102.

- [189] A. V Dudchenko, J. Rolf, K. Russell, W. Duan, D. Jassby, Organic fouling inhibition on electrically conducting carbon nanotube – polyvinyl alcohol composite ultra filtration membranes, *J. Memb. Sci.* 468 (2014) 1–10. doi:10.1016/j.memsci.2014.05.041.
- [190] C.F. de Lannoy, D. Jassby, D.D. Davis, M.R. Wiesner, A highly electrically conductive polymer-multiwalled carbon nanotube nanocomposite membrane, *J. Memb. Sci.* (2012). doi:10.1016/j.memsci.2012.05.061.
- [191] A. Criscuoli, M. Concetta, E. Drioli, Evaluation of energy requirements in membrane distillation, 47 (2008) 1098–1105. doi:10.1016/j.ccep.2007.03.006.
- [192] D.B. Gingerich, M.S. Mauter, Quantity, Quality, and Availability of Waste Heat from United States Thermal Power Generation, *Environ. Sci. Technol.* (2015). doi:10.1021/es5060989.
- [193] L. Song, Q. Huang, Y. Huang, R. Bi, C. Xiao, An electro-thermal braid-reinforced PVDF hollow fiber membrane for vacuum membrane distillation, *J. Memb. Sci.* 591 (2019) 117359. doi:10.1016/j.memsci.2019.117359.
- [194] A. Anvari, K.M. Kekre, A. Azimi, Y. Yao, A. Ronen, Membrane distillation of high salinity water by induction heated thermally conducting membranes, *J. Memb. Sci.* 589 (2019) 117253. doi:10.1016/j.memsci.2019.117253.
- [195] A. Anvari, K.M. Kekre, A. Ronen, Scaling mitigation in radio-frequency induction heated membrane distillation, *J. Memb. Sci.* (2020) 117859. doi:10.1016/j.memsci.2020.117859.
- [196] A. Anvari, A. Azimi Yancheshme, A. Ronen, Enhanced performance of membrane

distillation using radio-frequency induction heated thermally conducting feed spacers, *Sep. Purif. Technol.* 250 (2020) 117276.

doi:10.1016/j.seppur.2020.117276.

- [197] R. Francis, G. Byrne, G. Warburton, The corrosion of superduplex stainless steel in different types of seawater, *CORROSION*. (2011) 1–9.
- [198] A.H. Carlson, Precision forming of titanium alloys and the like by use of induction heating, U.S. Pat. No. 3,605,477. (1971).
- [199] C. Gosselin, J. Bizzozero, C. Gosselin, K.L. Scrivener, Expansion Mechanisms in Calcium Aluminate and Sulfoaluminate Systems with Calcium Sulfate Cement and Concrete Research Expansion mechanisms in calcium aluminate and sulfoaluminate systems with calcium sulfate, *Cem. Concr. Res.* 56 (2014) 190–202. doi:10.1016/j.cemconres.2013.11.011.
- [200] S.A. Ntim, S. Mitra, Removal of Trace Arsenic To Meet Drinking Water Standards Using Iron Oxide Coated Multiwall Carbon Nanotubes, (2011) 2077–2083.
- [201] A. V. Dudchenko, J. Rolf, K. Russell, W. Duan, D. Jassby, Organic fouling inhibition on electrically conducting carbon nanotube-polyvinyl alcohol composite ultrafiltration membranes, *J. Memb. Sci.* (2014). doi:10.1016/j.memsci.2014.05.041.
- [202] B. Li, K.K. Sirkar, Novel membrane and device for vacuum membrane distillation-based desalination process, *J. Memb. Sci.* (2005). doi:10.1016/j.memsci.2004.08.040.
- [203] V. Rudnev, D. Loveless, R.L. Cook, *Handbook of Induction Heating*, Second

Edition, 2018.

- [204] M.H. Tavakoli, H. Karbaschi, F. Samavat, Influence of workpiece height on the induction heating process Influence of workpiece height on the induction heating process, *Math. Comput. Model.* 54 (2011) 50–58. doi:10.1016/j.mcm.2011.01.033.
- [205] H. Hayer, O. Bakhtiari, T. Mohammadi, Analysis of heat and mass transfer in vacuum membrane distillation for water desalination using computational fluid dynamics ( CFD ), 3994 (2015). doi:10.1080/19443994.2014.912158.
- [206] A. Rojas-Morin, Y. Flores-Salgado, A. Barba-Pingarron, R. Valdez-Navarro, F. Mendez, O. Alvarez-Brito, M. Salgado-Baltazar, Thermal Analysis for the Solar Concentrating Energy and Induction Heating for Metals, in: *Comsol Conf.*, 2013: pp. 1–16.
- [207] R. Ghosh, L. Pradhan, Y.P. Devi, S.S. Meena, R. Tewari, A. Kumar, S. Sharma, N.S. Gajbhiye, R.K. Vatsa, B.N. Pandey, R.S. Ningthoujam, Induction heating studies of Fe<sub>3</sub>O<sub>4</sub>magnetic nanoparticles capped with oleic acid and polyethylene glycol for hyperthermia, *J. Mater. Chem.* 21 (2011) 13388–13398. doi:10.1039/c1jm10092k.
- [208] S. Sabale, V. Jadhav, V. Khot, X. Zhu, M. Xin, H. Chen, Superparamagnetic MFe<sub>2</sub>O<sub>4</sub> (M = Ni, Co, Zn, Mn) nanoparticles: synthesis, characterization, induction heating and cell viability studies for cancer hyperthermia applications, *J. Mater. Sci. Mater. Med.* 26 (2015) 127. doi:10.1007/s10856-015-5466-7.
- [209] O. Lucia, P. Maussion, E.J. Dede, J.M. Burdio, Induction heating technology and its applications: Past developments, current technology, and future challenges, *IEEE Trans. Ind. Electron.* 61 (2014) 2509–2520. doi:10.1109/TIE.2013.2281162.

- [210] H. Sarnago, A. Mediano, Ó. Lucia, High efficiency AC-AC power electronic converter applied to domestic induction heating, *IEEE Trans. Power Electron.* 27 (2012) 3676–3684. doi:10.1109/TPEL.2012.2185067.
- [211] M. Sweeney, J. Dols, B. Fortenbery, F. Sharp, Induction Cooking Technology Design and Assessment, 2014 ACEEE Summer Study Energy Effic. Build. (2014) 370–379. <https://aceee.org/files/proceedings/2014/data/papers/9-702.pdf>.
- [212] S. Tanrıseven, N. Uğur, A. Kanak, S. Ergün, Erinoks: EnerGy-efficient INduction-based food processing for optimized kitchens, *Proc. - IEEE Int. Symp. Circuits Syst.* 2019-May (2019). doi:10.1109/ISCAS.2019.8702571.
- [213] S. Tong, C.A. Quinto, L. Zhang, P. Mohindra, G. Bao, Size-Dependent Heating of Magnetic Iron Oxide Nanoparticles, *ACS Nano.* 11 (2017) 6808–6816. doi:10.1021/acsnano.7b01762.
- [214] M.I. Va, Temperature and concentration polarization in membrane distillation of aqueous salt solutions, 156 (1999).
- [215] H. Wang, B. Li, L. Wang, S. Song, J. Wang, Y. Feng, S. Wang, Permeate flux curve characteristics analysis of cross-flow vacuum membrane distillation, *Ind. Eng. Chem. Res.* 51 (2012) 487–494. doi:10.1021/ie201961v.
- [216] Q. Wang, L. Li, G. Chen, Y. Yang, Effects of magnetic field on the sol-gel transition of methylcellulose in water, *Carbohydr. Polym.* 70 (2007) 345–349. doi:10.1016/j.carbpol.2007.04.006.
- [217] A. Seyfi, R. Afzalzadeh, A. Hajnorouzi, Increase in water evaporation rate with increase in static magnetic field perpendicular to water-air interface, *Chem. Eng. Process. Process Intensif.* 120 (2017) 195–200. doi:10.1016/j.cep.2017.06.009.

- [218] K.T. Chang, C.I. Weng, An investigation into the structure of aqueous NaCl electrolyte solutions under magnetic fields, *Comput. Mater. Sci.* 43 (2008) 1048–1055. doi:10.1016/j.commatsci.2008.02.020.
- [219] E. Chibowski, A. Szcze, Influence of Magnetic Field on Evaporation Rate and Surface Tension of Water, (2018). doi:10.3390/colloids2040068.
- [220] R. Sarbatly, C.K. Chiam, Evaluation of geothermal energy in desalination by vacuum membrane distillation, *Appl. Energy.* 112 (2013) 737–746. doi:10.1016/j.apenergy.2012.12.028.
- [221] D. Winter, J. Koschikowski, M. Wieghaus, Desalination using membrane distillation : Experimental studies on full scale spiral wound modules, *J. Memb. Sci.* 375 (2011) 104–112. doi:10.1016/j.memsci.2011.03.030.
- [222] X. Han, W. Wang, K. Zuo, L. Chen, L. Yuan, J. Liang, Q. Li, P.M. Ajayan, Y. Zhao, J. Lou, Bio-derived ultrathin membrane for solar driven water purification, *Nano Energy.* 60 (2019) 567–575. doi:10.1016/j.nanoen.2019.03.089.
- [223] P.D. Dongare, A. Alabastri, S. Pedersen, K.R. Zodrow, Nanophotonics-enabled solar membrane distillation for off-grid water purification, (2017) 1–6. doi:10.1073/pnas.1701835114.
- [224] H. Geng, J. Wang, C. Zhang, P. Li, H. Chang, High water recovery of RO brine using multi-stage air gap membrane distillation, *Desalination.* 355 (2015) 178–185. doi:10.1016/j.desal.2014.10.038.
- [225] W.L. Marshall, R. Slusher, E. V. Jones, Aqueous Systems at High Temperature. XIV. Solubility and Thermodynamic Relationships for CaSO<sub>4</sub> in NaCl-H<sub>2</sub>O Solutions from 40· to 200· C., 0 to 4 Molal NaCl, *J. Chem. Eng. Data.* 9 (1964)

- 187–191. doi:10.1021/je60021a011.
- [226] K.U.G. Raju, G. Atkinson, The Thermodynamics of “ Scale ” Mineral Solubilities . 3 . Calcium Sulfate in Aqueous NaCl, (1990) 361–367.  
doi:10.1021/je00061a038.
- [227] H.E.L. Madsen, Influence of magnetic field on the precipitation of some inorganic salts, 152 (1995) 94–100.
- [228] A. Shahryari, M. Pakshir, Influence of a modulated electromagnetic field on fouling in a double-pipe heat exchanger, 3 (2007) 389–395.  
doi:10.1016/j.jmatprotec.2007.10.048.
- [229] X. Xiaokai, Research on the electromagnetic anti-fouling technology for heat transfer enhancement, 28 (2008) 889–894.  
doi:10.1016/j.applthermaleng.2007.07.006.
- [230] M. Rouina, H. Kariminia, S. Abbas, E. Shahryari, Effect of electromagnetic field on membrane fouling in reverse osmosis process, DES. 395 (2016) 41–45.  
doi:10.1016/j.desal.2016.05.009.
- [231] N.S. Zaidi, J. Sohaili, K. Muda, M. Sillanpää, Magnetic Field Application and its Potential in Water and Wastewater Treatment Systems Magnetic Field Application and its Potential in Water and Wastewater Treatment Systems, 2119 (2014).  
doi:10.1080/15422119.2013.794148.
- [232] A. Luo, N. Lior, Critical review of membrane distillation performance criteria, Desalin. Water Treat. 57 (2016) 20093–20140.  
doi:10.1080/19443994.2016.1152637.
- [233] C. Piyadasa, H.F. Ridgway, T.R. Yeager, M.B. Stewart, C. Pelekani, S.R. Gray,

- J.D. Orbell, The application of electromagnetic fields to the control of the scaling and biofouling of reverse osmosis membranes - A review, *Desalination*. 418 (2017) 19–34. doi:10.1016/j.desal.2017.05.017.
- [234] G.Z. Ramon, E.M. V Hoek, On the enhanced drag force induced by permeation through a filtration membrane On the enhanced drag force induced by permeation through a filtration membrane, (2012). doi:10.1016/j.memsci.2011.10.056.
- [235] I.B. Silva, J.C. Queiroz, D.F.S. Petri, *Colloids and Surfaces A : Physicochemical and Engineering Aspects* The effect of magnetic field on ion hydration and sulfate scale formation, *Colloids Surfaces A Physicochem. Eng. Asp.* 465 (2015) 175–183. doi:10.1016/j.colsurfa.2014.10.054.
- [236] J. Li, J. Liu, T. Yang, C. Xiao, Quantitative study of the effect of electromagnetic field on scale deposition on nanofiltration membranes via UTDR, 41 (2007) 4595–4610. doi:10.1016/j.watres.2007.06.041.
- [237] M.A. Salman, M. Safar, G.A.- Nuwaibit, The Effect of Magnetic Treatment on Retarding Scaling Deposition, 5 (2015) 62–77.
- [238] J.P. Mericq, S. Laborie, C. Cabassud, Vacuum membrane distillation of seawater reverse osmosis brines, *Water Res.* (2010). doi:10.1016/j.watres.2010.06.052.
- [239] J.A.. Meijer, G.M. van Rosmalen, Solubilities and supersaturations and its hydrates in seawater, *Desalination*. 51 (1984) 255–305.
- [240] C.R. Martinetti, A.E. Childress, T.Y. Cath, High recovery of concentrated RO brines using forward osmosis and membrane distillation, 331 (2009) 31–39. doi:10.1016/j.memsci.2009.01.003.
- [241] W.L. Marshall, R. Slusher, Thermodynamics of Calcium Sulfate Dihydrate in

Aqueous Sodium Chloride Solutions, 0-110° 1,2 , J. Phys. Chem. 70 (2006) 4015–4027. doi:10.1021/j100884a044.

[242] L. Li, K.K. Sirkar, Studies in vacuum membrane distillation with flat membranes, J. Memb. Sci. 523 (2017) 225–234. doi:10.1016/j.memsci.2016.09.028.

[243] X. Wang, L. Zhang, H. Yang, H. Chen, Feasibility research of potable water production via solar-heated hollow fiber membrane distillation system, Desalination. 247 (2009) 403–411. doi:10.1016/j.desal.2008.10.008.

[244] R. Hergt, S. Dutz, M. Röder, Effects of size distribution on hysteresis losses of magnetic nanoparticles for hyperthermia, J. Phys. Condens. Matter. 20 (2008). doi:10.1088/0953-8984/20/38/385214.

[245] A. Anvari, A. Azimi Yancheshme, A. Ronen, Enhanced performance of membrane distillation using radio-frequency induction heated thermally conducting feed spacers, Sep. Purif. Technol. 250 (2020) 117276. doi:10.1016/j.seppur.2020.117276.